AN ABSTRACT OF THE THESIS OF

Alexander M. Dueñas for the degree of Master of Science in Nuclear Engineering presented on December 5, 2019.

Title: Investigation of Drag Coefficient and Virtual Mass Coefficient on Rising Ellipsoidal Bubbles

Abstract approved:

____

Qiao Wu   Wade R. Marcum

Accurately describing drag and virtual mass forces in two-phase flows is crucial for high fidelity modeling of nuclear thermal hydraulic safety systems. This study compares existing drag coefficient, C_D, correlations commonly used in computational fluid dynamics (CFD) applications for air bubbles to experimental data collected for ellipsoidal air bubbles of varying diameter. This study also measured the virtual mass coefficient on a cylinder rod using a method that considers viscous and wake effects. This experiment used velocity field measurements obtained with particle image velocimetry (PIV). An experimental flow loop has been built to inject air bubbles of varying diameter into an optically clear acrylic test section and had the capability to use a cylinder rod perpendicular to flow. A rigorous uncertainty analysis is presented for measured values which provided insight for improvements for future experimental studies. These experiments resulted in total, form, and skin drag coefficients to be directly measured with the nominal trend of increasing form drag for increasing bubble diameter experimentally confirmed. The virtual mass coefficient analysis demonstrated a method applicable for steady state conditions. This method was capable of retrieving the potential flow solution when the predicted drag work from the wake was removed and identified experimental setups useful for characterizing the influence of wake dynamics on virtual mass.

Investigation of Drag Coefficient and Virtual Mass Coefficient on Rising Ellipsoidal Bubbles

by

Alexander M. Dueñas

A THESIS

submitted to

Oregon State University

in partial fulfillment of
the requirements for the
degree of

Master of Science

Presented December 5, 2019
Commencement June 2020

Master of Science thesis of Alexander M. Dueñas presented on December 5, 2019

APPROVED:

Co-Major Professor, representing Nuclear Engineering

Co-Major Professor, representing Nuclear Engineering

Head of the School of Nuclear Science and Engineering

Dean of the Graduate School

I understand that my thesis will become part of the permanent collection of Oregon State University libraries. My signature below authorizes release of my thesis to any reader upon request.

Alexander M. Dueñas, Author

ACKNOWLEDGEMENTS

I would like to deeply thank my advisors Dr. Qiao Wu and Dr. Wade Marcum for their continual support, challenging myself to be the best that I can, the opportunity to study under them and be a part of their research groups. Acknowledgements must be given to Isaiah Wieland whose collaboration was vital for the construction of our experimental facility. Without his help I could not have collected my data, and debugging issues would have taken so much longer. I also want to thank Musa Moussaoui for his exceptional patience and walking through concepts with me. Chris Nighbert is also recognized and thanked for his efforts to lay the ground work for this project and experimental facility. Additionally, I would like to thank Nick Swango for always willing to help, his invaluable lessons about pipe fitting, and continually reminding me of common sense.

I would like to offer special thanks to Dr. Carl Stoots, who is no longer with us, for being a wonderful person and mentor. He is deeply missed.

I want to thank my best friend Ari Foley for her always great advice, fantastic humor, and for continually raising the bar on how amazing plots can look. Lastly, I would like to thank my parents David and Joanne Dueñas, my cool older brother Kevin Dueñas, my grandmother Roberta Lowry, and my aunt Beth Berenson for their constant support, encouragement, and love.

TABLE OF CONTENTS

Section Page

1 Introduction ... 1

1.1 Motivation ... 1
1.2 Purpose ... 2
1.3 Objectives ... 2
1.4 Document Overview ... 3

2 Survey of Literature ... 4

2.1 Two-Phase Drag ... 4
2.2 Virtual Mass ... 11
2.3 Two-Phase Experimental Techniques ... 16
2.4 Summary ... 21

3 Experimental Facility ... 22

3.1 Facility Description ... 23
3.2 Instrumentation ... 23
3.3 Particle Image Velocimetry System ... 25
3.4 Bubble Injection System ... 26

4 Methodology ... 29

4.1 Drag Coefficient ... 31
4.2 Virtual Mass Coefficient ... 35
4.3 Sources of Error ... 39
4.4 Uncertainty Analysis ... 40

5 Results & Discussion ... 43

5.1 Drag Coefficient ... 53
5.2 Virtual Mass Coefficient ... 59

6 Conclusions ... 72

6.1 Significance of Work ... 72
6.2 Assumptions and Limitations ... 73
6.3 Observations ... 74
6.4 Future Work ... 74

References ... 76
Nomenclature ... 80
Appendix A: Uncertainty Analysis ... 82

Drag Coefficient Uncertainty Propagation: ... 82
Total Drag/Buoyancy Force Uncertainty Propagation: ... 83
Form Drag Uncertainty Propagation: ... 83
Skin Drag Uncertainty Propagation: ... 86
Area Uncertainty Propagation: ... 87

TABLE OF CONTENTS (CONTINUED)

Page

Diameter Uncertainty Propagation for $V \geq 0.1$ [mL]: 87
Tate's Law Uncertainty Propagation for $V < 0.1$ [mL]: 87
Velocity Uncertainty Propagation: 88
Pressure Uncertainty Propagation:... 89
Virtual Mass Coefficient Uncertainty Propagation: 93
Reynolds Number Uncertainty Propagation: 95
Appendix B: Potential Flow Kinetic Energy Proof 96
Relative Kinetic Energy.. 96
Relative Velocity 99

LIST OF FIGURES

Figure Page

Figure 1: Haberman and Morton measured drag coefficients for various liquids [4] 5

Figure 2: Drag coefficient for single particle in infinite medium [9] 9

Figure 3: Typical PIV Planar System 18

Figure 4: Bubble Investigation Loop 22

Figure 5: Injection System with 5 mL Syringe 28

Figure 6: Injection System with 0.5 mL Syringe 28

Figure 7: Example cross-correlation map 30

Figure 8: Pressure surface integral geometry diagram 34

Figure 9: Example drag force component determination 34

Figure 10: Predicted virtual mass coefficient for spherical potential flow 37

Figure 11: Infinite cylinder kinetic energy per unit length spatial map 38

Figure 12: 0.013 mL bubble rising 45

Figure 13: 0.027 mL bubble rising 45

Figure 14: 0.04 mL bubble rising 46

Figure 15: 0.053 mL bubble rising 46

Figure 16: 0.067 mL bubble rising 47

Figure 17: 0.013 mL bubble velocity field | t=0.453 s 48

Figure 18: 0.013 mL bubble vertical velocity field | t =0.453 s 48

Figure 19: 0.013 mL bubble horizontal velocity field | t=0.453 s 49

Figure 20: 0.013 mL bubble vorticity map | t=0.453 s 49

Figure 21: 0.067 mL bubble velocity field | t=1.740 s 50

Figure 22: 0.067 mL bubble vertical velocity field | t=1.740 s 51

Figure 23: 0.067 mL bubble horizontal velocity field | t=1.740 s 51

Figure 24: 0.067 mL bubble vorticity map | t=1.740 s 52

Figure 25: Bubble terminal velocity versus spherical equivalent bubble diameter 53

Figure 26: Measured total drag coefficient versus Reynolds Number 54

Figure 27: Measured total drag coefficient versus prediction 55

Figure 28: Form drag coefficient versus Reynolds number 57

LIST OF FIGURES (CONTINUED)

Figure Page

Figure 29: Measured skin drag versus Reynolds number 58

Figure 30: Cylinder 250 mm/s integral time scale spatial map 61

Figure 31: Cylinder 120 [mm/s] turbulent kinetic energy map 62

Figure 32: Cylinder 150 [mm/s] turbulent kinetic energy map 63

Figure 33: Cylinder 210 [mm/s] turbulent kinetic energy map 63

Figure 34: Cylinder 250 [mm/s] turbulent kinetic energy map 64

Figure 35: Cylinder 270 [mm/s] turbulent kinetic energy map 64

Figure 36: Cylinder measured virtual mass coefficient versus Reynolds number............ 66

Figure 37: Integrated kinetic energy with increasing distance into wake......................... 68

Figure 38: Cylinder measured virtual mass coefficient with drag work subtracted 69

Figure 39: Cylinder measured drag coefficient versus Reynolds number........................ 70

LIST OF TABLES

Table	Page

Table 1: Instrumentation Specification 24
Table 2: Data Acquisition System Uncertainty 25
Table 3: PIV Laser Specifications 26
Table 4: High-Speed Camera Specifications 26
Table 5: Bubble Injection System Specifications 27
Table 6: Bubble Test Matrix 43
Table 7: Total Drag Coefficient Values with 95% confidence 56
Table 8: Form Drag Coefficient Values with 95% confidence 59
Table 9: Cylinder rod flow conditions 60
Table 10: Cylinder virtual mass coefficient w/ 95% confidence 71

1 INTRODUCTION

Nuclear power plants and reactors often employ the use of best estimate codes, such as RELAP5 or TRACE V5 [1], to perform reactor safety analyses. The use of computer codes allows for large and complex calculations to be performed relatively quickly and with a known degree of accuracy. Most of these codes perform their calculations by receiving the inputs of the systems operating conditions and evaluate state properties, boundary conditions, and solve conservation equations. These codes are capable of modeling two phase flow by using conservation equations of mass, momentum, and energy for each of the two phases. The balance equations for both phases interact with each other through "jump conditions". These jump conditions are applied at the interfacial surface area of the two-phase fluid for interfacial forces such as drag, virtual mass, turbulent dispersion, and lift forces [2]. Modeling the interactions between the phases has historically relied on empirical and semi-empirical correlations, however analytical models can be implemented for simplified geometries such as spheres. These closure relationships were developed by performing a multitude of fluids experiments. When using an empirical approach, correlations are developed from experiments to be used to predict reactor and plant behavior. However, the limitation of this approach is that correlations are limited to being used only within the range of the experimental database they are developed from.

Because best estimate codes are used to design nuclear power plants and for reactor safety analyses, the accuracy of these codes impact the safety margins they can operate at. This results from uncertainty propagation due to numerical implementation of mechanistic models and the accuracy of the experimental database used for the empirical correlations. This means that the error propagation from experimental uncertainty can be a limiting factor when determining safety margins.

1.1 Motivation

Experiments that developed empirical correlations typically relied on measurement devices such as probes, hot wire anemometry, and pitot tubes, which are intrusive and provide single point measurements. An intrusive technique disrupts the fluid structure and provides limited information regarding the underlying flow pattern. This disruption of the fluid structure can cause deformation of each of the two phases that comprise the fluid and alter the flow's velocity distribution which can result in large uncertainties in bias associated with the experimental data.

However, there have been many advancements in fluid measurement technology that can reduce the uncertainty by obtaining more accurate measurements. One such advancement is particle image velocimetry (PIV). Particle Image Velocimetry is an investigative technique that uses a high-powered laser and high-speed camera to obtain non-intrusive, spatially resolved instantaneous velocity measurements within a flow field [3]. This eliminates the flow irregularities caused by typical intrusive measurements and reduces the uncertainty associated with the flow measurement.

While computational capabilities have greatly increased, the improvement in the characterization of these experiments and empirical models have not increased equivalently. A reexamination of drag and virtual mass coefficient correlations can be performed with the PIV technique to possibly reduce the uncertainty associated with drag correlations and provide a better understanding of the virtual mass coefficient. Reducing the uncertainty associated with these relationships could further improve the modeling capabilities of these phenomenon in thermal hydraulic codes.

1.2 Purpose

The purpose of this study is to provide an evaluation of existing drag coefficient correlations and the virtual mass coefficient for a single bubble using the PIV technique.

1.3 Objectives

The objective of this thesis is to provide a quantitative error between experimental data and existing drag and virtual mass coefficient correlations by varying Reynolds number and bubble radius. The goal of this work is to demonstrate the reduced uncertainty by obtaining improved velocity measurements to better characterize the phenomenon of drag in two phase flow. This study will proceed with the following objectives:

- Construct an experimental flow loop which can control flow rate and bubble size to perform PIV measurements of a two phase fluid flow.
- Perform experiments varying Reynolds number and bubble radius and obtain velocity field information around a single bubble.
- Compare existing drag coefficient correlations using the experimental data.
- Measure virtual mass coefficient for single bubbles
- Perform uncertainty analysis based upon the experimental data.

1.4 Document Overview

This chapter discusses the context of the study and identifies motivation for the need to reexamine drag coefficient correlations. This document is organized with the following breakdown:

Chapter 2: Literature Survey – This chapter will include a review of pertinent literature that describes two phase flow experimental techniques, drag coefficient, and virtual mass. The measurement techniques used by past researchers will be discussed and what impacts it made on the formulation of drag coefficient correlations.

Chapter 3: Experimental Setup and Methods – The experimental setup used in this study will be described and a thorough explanation of the methodology implemented will be given. Justification and limitations of the methodology will be examined.

Chapter 4: Results – Presents the results of the PIV experiments.

Chapter 5: Discussion – Discussion of the results and phenomena observed from the experiment.

Chapter 6: Conclusion – Contains concluding remarks on the study and discussion of significant finds and future work to improve the experiment.

2 SURVEY OF LITERATURE

There has been extensive research into bubble systems and their dynamics, this chapter reviews the relevant literature on drag and virtual mass coefficients. Determining these coefficients has relied on various measurement techniques. These techniques are introduced with a description of their working principles, strengths, and limitations. Particle image velocimetry will be discussed with highlights for its selection as the measurement technique used for this study.

2.1 Two-Phase Drag

Drag force is the combination of pressure and frictional effects on a body to oppose its relative motion in a fluid. It is typically described by eq.(1):

$$F_D = \frac{1}{2} C_D \rho_f A u_r^2 \tag{1}$$

where ρ_f is the density of the fluid surrounding the body, A is the projected cross sectional area tangential to the direction of the drag force, u is the relative velocity between the body and the fluid, and C_D is the drag coefficient for the body in the flow system. In bubbly flows, the primary motion investigated is the rise of bubbles. As bubbles rise, they quickly reach their terminal velocity which is used as the relative velocity. There are three types of motion rising bubbles have: a rectilinear path, helical spiral, or a rectilinear path with rocking [4]. These motion types have been found to be largely dependent on the Reynolds number which depends on bubble shape [4], [5]. Drag coefficient on spherical solid particles, drops, and bubbles have been extensively studied by Cox (1962), Levich (1962), Taylor and Acrivos (1964), Wellek et al. (1966), and Soo (1970).

An early comprehensive study on the motion of bubbles was performed by Haberman and Morton [4] to study air bubbles rising in various liquids. This study used eight fluids (water, glim solution, mineral oil, varsol, turpentine, methyl alcohol, corn syrup, glycerine-water mixtures, olive oil, and syrup), with water at two temperatures and filtered/unfiltered, and with corn syrup and glycerine at two concentrations. Observations of drag coefficient dependent on surface contamination showed that pure systems had lower drag coefficient. The possible explanation was that surface contaminates eliminates the internal circulation and causes the bubble to behave more as a rigid particle (sphere) which has higher drag than deformable fluid particles. Figure 1, adapted from reference [4], shows the calculated drag coefficients based on measured terminal velocity for various liquids versus Reynolds number, eq. (2). Each liquid is plotted based by increasing Morton number, eq. (3).

$$\mathrm{Re} = \frac{2\rho_c U r_e}{\mu_c} \tag{2}$$

$$\mathrm{Mo} = \frac{g\mu_c^4}{\rho_c \sigma^3} \tag{3}$$

The Morton number is unique for each fluid. It was shown that liquids with low Morton numbers $\left(\mathrm{Mo} \leq 10^{-8}\right)$ all experienced minimum drag coefficients near Re=250 whereas liquids with high Morton numbers $\left(\mathrm{Mo} \geq 10^{-2}\right)$ did not reach this same minimum and transitioned to spherical cap bubbles earlier than other liquids.

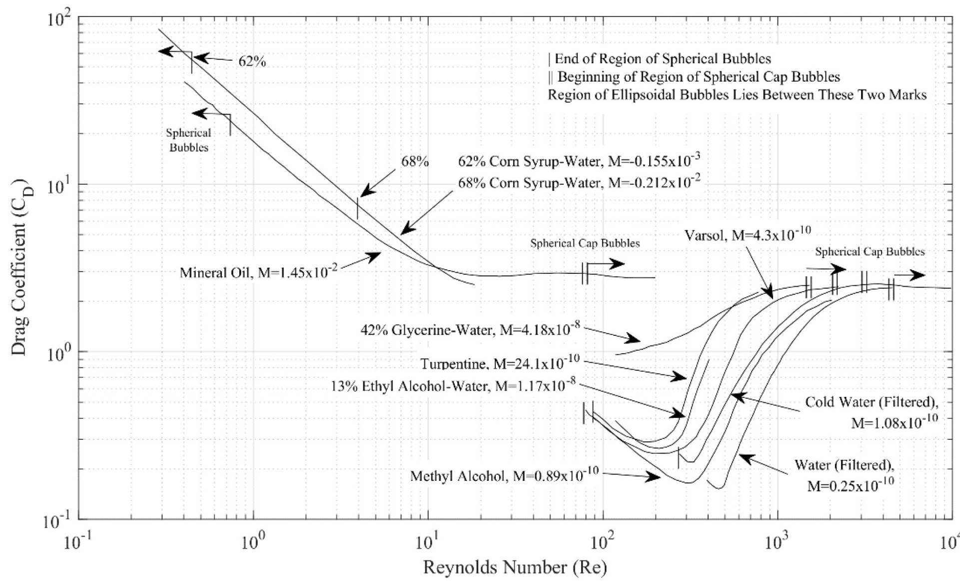

Figure 1: Haberman and Morton measured drag coefficients for various liquids [4]

The drag coefficient was high at low Reynolds numbers which corresponded to small spherical bubbles which follow Stokes flow. At small particle sizes a fluid particle behaves as a rigid particle which has higher drag than fluid particles as mentioned above. As the equivalent bubble radius (r_e) increases, the bubble shape transitions from spherical bubbles to an ellipsoidal shape because the inertial forces become larger than the surface tension of the bubble [6]. Spherical cap bubbles occurred in all liquid systems after a Weber number, eq. (4), of 20 was reached.

$$\mathrm{We} = \frac{2\rho_c U^2 r_e}{\sigma} \tag{4}$$

The drag coefficient for the cap bubbles were all independent of bubble size and equaled $C_D = 2.6$, with the terminal velocity only depending on the equivalent radius [4]. This indicated that after $\mathrm{We} \geq 20$ the drag coefficient of spherical cap bubbles did not depend on the continuous phase's fluid.

Harmathy's early work related the drag coefficient of drops or bubbles to spherical solid particles [5]. An important aspect investigated is the effect of bubble shape on bubble motion and resulting drag coefficient. Harmathy notes that small fluid particles with a spherical or slightly ellipsoidal shape move in straight line (rectilinear) motion. When the particle becomes predominantly ellipsoidal and more distorted, the motion becomes more zig-zag and helical in its path. However, the magnitude of this oscillatory motion decreases with greater distortion. After enough distortion, the fluid particle transitions to a spherical cap bubble which has rectilinear motion again which was also observed by Haberman and Morton. Oscillating motion was seen occurring with Reynolds number larger than 500 and indicated turbulent flow conditions had been reached. Harmathy discusses that under turbulent flow conditions, the drag coefficient becomes independent of the Reynolds number over a wide range while retaining the same shape. Several prior publications reported that drag coefficient strongly depended on Reynolds number, however Harmathy notes that varying the Reynolds number for fluid particles often changes the particle shape. Harmathy stated that particle shape was the dominant influence on the drag coefficient in the turbulent flow regime, and results in the dependence of the Eötvös number (Eo), eq.(5) , which compares gravitational and surface tension forces acting on bubbles or drops.

$$\mathrm{Eo} = \frac{\Delta\rho g D_e^2}{\sigma} \tag{5}$$

Harmathy noted that the zig-zag or spiraling path for ellipsoidal bubbles increases the drag coefficient of the bubble and developed a correlation, eq.(6), from experimental data to relate drag coefficient for ellipsoidal bubbles in an infinite medium to spherical particles in an infinite medium, eq.(7) [5].

$$\frac{C_{\infty}^{o}}{C_{s,\infty}} = 1.29\mathrm{Eo}^{\frac{1}{2}}\,;\left(\mathrm{Eo} \leq 13\right) \tag{6}$$

$$C_{s,\infty} = \frac{4}{3}\frac{d_e \Delta\rho g}{\rho_c u_{\infty}^2} \tag{7}$$

Where $C_{o,\infty}$ is the drag coefficient for a sphere, u_{∞} is a sphere's terminal velocity, ρ_c is the continuous phase's density, $\Delta\rho$ is the difference in density between the continuous and dispersed phases, d_e is the equivalent bubble diameter, and g is the gravitational constant.

Moore derived a drag coefficient correlation, eq. (8), for spherical gas bubbles rising in a pure system by evaluating the viscous dissipation of the wake using potential flow [7]. However, if there was any contamination in the flow than the correlation breaks down quickly.

$$C_D = \frac{48}{\mathrm{Re}}\left\{1 - \frac{2.2}{\mathrm{Re}^{\frac{1}{2}}} + O\left(\mathrm{Re}^{-\frac{5}{6}}\right)\right\} \tag{8}$$

This helped show how the level of contamination in the flow greatly affects the drag force experienced by the bubble. Wallis describes the relationship of terminal velocity and corresponding bubble radius [8], and suggested that in theory surface tension should be the only parameter distinguishing drops and bubbles from solid particles. However, the varying contamination between experimental datasets was considered to cause of the wide spread of data.

Ishii and Zuber developed single bubble drag coefficient correlations based on over 1000 experimental data points. This work summarized previously studied drag coefficient forms to describe drag on single bubbles to develop drag coefficient relations for multi-particle systems [9]. They defined the correlations, eqs.(9)-(12), based on four flow regimes: stokes regime, viscous regime (undistorted particles), distorted particle regime, and spherical-cap regime which are listed below respectively with applicable ranges.

$$C_D = \frac{24}{\mathrm{Re}}; \mathrm{Re} << 1 \tag{9}$$

$$C_D = \frac{24}{\mathrm{Re}}\left(1 + 0.1\mathrm{Re}^{0.75}\right); 1 \le \mathrm{Re} \le 2\times10^5 \tag{10}$$

$$C_D = \frac{4}{3} r_e \left(\frac{g\Delta\rho}{\sigma}\right)^{0.5}; \begin{cases} N_\mu \ge \dfrac{36(2)^{0.5}\left(1 + 0.1\mathrm{Re}^{0.75}\right)}{\mathrm{Re}^2} \\ N_\mu \equiv \dfrac{\mu_c}{\left[\rho_c \sigma \left(\dfrac{\sigma}{g\Delta\rho}\right)^{0.5}\right]^{0.5}} \end{cases} \tag{11}$$

$$C_D = \frac{8}{3}; r_e \ge 2\left(\frac{\sigma}{g\Delta\rho}\right)^{0.5} \tag{12}$$

Equation (10) is very similar in form to a correlation, eq.(13), developed by Schiller and Naumann in 1933 [6].

$$C_D = \frac{24}{\mathrm{Re}}\left(1 + 0.15\mathrm{Re}^{0.687}\right); \mathrm{Re} \le 800 \tag{13}$$

Equations (9)-(12) are plotted in Figure 2, adapted from reference [9], and show the flow regime regions considered by Ishii and Zuber. The plot shows similar trends seen in Figure 1, the transition to spherical cap bubble roughly follows the same shape and is shown to depend on the parameter N_μ which is described as the viscosity number. This number scales the viscous force of the dispersed fluid by the bubble's surface tension [9]. Fluids with low viscosity numbers approximate solid particles for larger Reynolds numbers, because the surface tension forces are substantially stronger than the viscous forces which allows the bubble to act as a rigid surface. As described in Figure 1, the drag coefficient in the distorted regime reaches a minimum before it transitions to a spherical cap bubble. Unlike Haberman and Morton, Figure 2 shows that the minimum drag coefficient largely depends on the viscosity number.

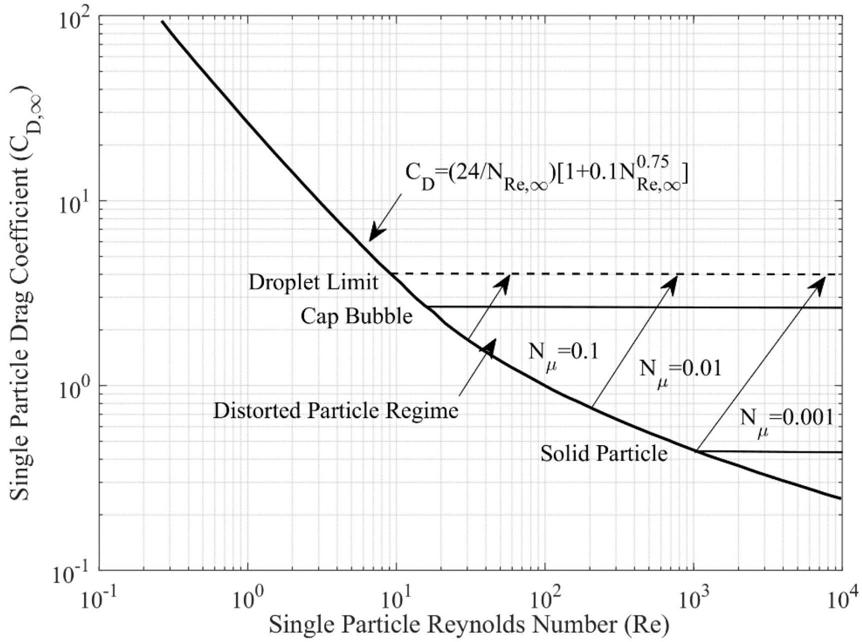

Figure 2: Drag coefficient for single particle in infinite medium [9]

Tomiyama et al., investigated drag coefficient on single air bubbles dependent on fluid properties, gravity, bubble diameter, and contamination of the continuous phase [10]. Spherical bubbles are categorized into three groups: pure systems, slightly contaminated, and contaminated. Because the bubbles are spherical, they exhibit rectilinear motions. Tomiyama et al., noted that in pure systems an internal circulation is formed which decreases viscous drag, which is noted by Harmathy as well [5]. A contaminated system causes the bubble interface to act as a rigid surface, and suggest that contaminated systems allow spherical bubbles to behave similar to solid particles [10]. The researchers modeled the drag coefficient for non-spherical bubbles as a wave propagation caused by the gas phase acting as a "disturbance" in the liquid phase. This disturbance causes a wave propagation that has a characteristic phase velocity. Because the bubble's terminal velocity cannot be larger than its phase velocity, the limit on the terminal velocity becomes the phase velocity. The terminal velocity is then calculated as:

$$V_T^2 = \frac{2\sigma}{\rho_f d} + \frac{\left(\rho_f - \rho_g\right) g d}{2\rho_f} \tag{14}$$

Using eq.(14) as the definition of terminal velocity and performing a force balance between the drag and buoyancy forces results in the drag coefficient being:

$$C_D = \frac{8}{3}\frac{\mathrm{Eo}}{\mathrm{Eo}+4} \tag{15}$$

This result was verified against experimental data by Clift, Grace, and Weber [6] for $0.7 < d < 1.5\,\mathrm{mm}$ sized bubbles. Three drag coefficient correlations, eqs.(16)-(18), for non-spherical bubbles were subsequently developed for pure, slight contaminated, and contaminated systems.

$$C_D = \max\left\{\min\left[\frac{16}{\mathrm{Re}}\left(1+0.15\,\mathrm{Re}^{0.687}\right),\frac{48}{\mathrm{Re}}\right],\frac{8}{3}\frac{\mathrm{Eo}}{\mathrm{Eo}+4}\right\} \tag{16}$$

$$C_D = \max\left\{\min\left[\frac{24}{\mathrm{Re}}\left(1+0.15\,\mathrm{Re}^{0.687}\right),\frac{72}{\mathrm{Re}}\right],\frac{8}{3}\frac{\mathrm{Eo}}{\mathrm{Eo}+4}\right\} \tag{17}$$

$$C_D = \max\left\{\frac{24}{\mathrm{Re}}\left(1+0.15\,\mathrm{Re}^{0.687}\right),\frac{8}{3}\frac{\mathrm{Eo}}{\mathrm{Eo}+4}\right\} \tag{18}$$

It can be noted that the drag coefficient correlations for pure systems are similar to the correlation derived by Moore [7], and contaminated systems include correlations from Ishii and Zuber [9].

Zhang, et al numerically investigated the effect of closure models for interfacial forces consisting of drag, lift and virtual mass [11]. Closure relations proposed by Tomiyama [12] for each interfacial force were compared to velocity data from 4 mm bubbles by Deen [13]. The drag coefficient correlation presented by Tomiyama differed from previous correlations and is shown with eq.(19):

$$C_D = \frac{8}{3}\frac{\mathrm{Eo}\left(1-\mathrm{E}^2\right)}{\mathrm{E}^{\frac{2}{3}}\mathrm{Eo}+16\left(1-\mathrm{E}^2\right)\mathrm{E}^{\frac{4}{3}}}F\left(\mathrm{E}\right)^{-2} \tag{19}$$

$$\mathrm{E} = \frac{1}{1+0.163\,\mathrm{Eo}^{0.757}}$$

$$F\left(\mathrm{E}\right) = \frac{\sin^{-1}\left(1-\mathrm{E}^2\right)^{0.5}-\mathrm{E}\left(1-\mathrm{E}^2\right)^{0.5}}{1-\mathrm{E}^2}$$

where C_D is the bubble drag coefficient, E and $F(E)$ are functions of the Eötvös number. The drag correlation, eq(19), was shown to over predict the drag force on the gas phase when the bubbles were still low in the tank column and matched well as the bubbles rose higher into the tank.

Kelbaliyev and Ceylan used the method of tangents to combine several drag coefficient correlations dependent on Re, Mo, and Eo numbers at low Reynolds numbers into a single correlation with a range up to Re=100 [14]. They noted that the drag coefficient of drops or bubbles continue to decrease as a function of Reynolds number until it reaches a minimum. According to Kelbaliyev and Ceylan, this minimum drag occured at eq.(20).

$$\mathrm{Re}\,\mathrm{Mo}^{\frac{1}{6}} \approx 7 \tag{20}$$

This indicated that shape deformation would occur at values larger than 7 [14]. Traditionally, correlations show that the drag coefficient becomes constant at higher Reynolds numbers, but these correlations do not factor shape deformation which alters the drag.

2.2 Virtual Mass

The virtual mass (also known as added mass) force of a particle is the force needed to “accelerate the apparent mass of the surrounding fluid phase when the relative velocity changes” [2]. The most commonly expressed form for the virtual mass force is shown in eq.(21):

$$F_k^{VM} = \mp C_{VM}\alpha_g\rho_f\left(\frac{D_g u_g}{Dt} - \frac{D_f u_f}{Dt}\right) \tag{21}$$

where F_k^{VM} is the virtual mass force for either phase, C_{VM} is the virtual mass coefficient, α_g is the dispersed phase void fraction, ρ_f is the continuous phase density, the first material derivative term is for the dispersed (vapor) phase, and the second material derivative is for the continuous (liquid) phase. The virtual mass occurs in unsteady motion and is one of the two additional terms considered in the momentum equation, where the Basset force is the other term which describes boundary layer development resulting from the acceleration. Lamb used potential flow theory to analytically derive the virtual mass coefficient for a rigid sphere which is $C_{VM} = 0.5$ [15]. This coefficient value has been traditionally used when including the force in two-fluid models.

Zuber modified the momentum equation proposed by Bassett's single particle accelerating in laminar flow model which used the same virtual mass coefficient as Lamb [16]. Using void fraction in this modification the virtual mass coefficient was expressed with eq.(22):

$$C_{VM} = \frac{1}{2}\frac{1+2\alpha_g}{1-\alpha_g} \tag{22}$$

where α_g is the dispersed phase void fraction. A factor that Zuber considered to determine the expression's validity was that it returns Lamb's virtual mass coefficient when $\alpha_g \to 0$ which causes $C_{VM} \to 0.5$.

Wijngaarden and Jeffrey analyzed the effect of virtual mass on bubble clouds to determine the effective virtual mass of a bubble in a two phase mixture. Their potential flow analysis showed that a massless sphere moving in an impulsively generated flow causes the sphere to move with the three times the velocity it had in the uniform flow [17].

Geurst derived equations of motion for two phase flows, and derived a dispersion equation of the dispersed phase in the continuous phase which possessed two complex conjugate roots when the relative velocity difference is not too large. This suggested that two-phase flows that neglect virtual mass force will generally be unstable [18]. The equations of fluid motion were derived using Hamilton's principle which uses a Lagrangian reference frame and resulted in the virtual mass coefficient being expressed as:

$$C_{VM} = \frac{1}{2}\hat{m}\alpha_o\left(1-\alpha_o\right)\left(1-\frac{\hat{m}+2}{\hat{m}}\alpha_o\right) \tag{23}$$

where α_o is the void fraction, and $\hat{m}$ is a parameter dependent on the flow. Spherical bubbles use $\hat{m}=1$, which show that the virtual mass coefficient goes to zero with a void fraction $\alpha_o = 0.333$. The author suggested this showed that bubbly flow breaks down at that void fraction and transitions to another two phase flow regime [18].

Felderhof analyzed virtual mass in two phase flows with linearized Navier-Stokes equations at low Reynolds numbers in an inviscid fluid with a potential flow analysis. This analysis found that the virtual mass coefficient of spherical particles suspended in a fluid can be a direct expression, eq.(24), in terms of an effective dielectric constant (γ).

$$C_{VM} = \frac{1-\gamma\alpha}{2-3\alpha+\gamma\alpha} \tag{24}$$

The added mass determined from this approach did not match the induced mass term derived by Zuber except when the dielectric constant is approximated with the Clausis-Mossotti value. Which results in $\gamma = 1$ which causes the virtual mass to become identical with Zuber's expression [19].

Mei and Klausner numerically modeled a stationary spherical bubble in a flow with small fluctuations in the free stream velocity. They found the added mass term to be directly proportional to the Reynolds as shown in eq. (25).

$$F_{VM} = \frac{\mathrm{Re}}{18} \tag{25}$$

They noted that at $\mathrm{Re} > 6$ the added mass force exceeds the Basset force and at $\mathrm{Re} > 200$ the added mass greatly exceeds the Basset force by a factor of 64 at low frequency velocity oscillations which showed the more dominant effect from the added mass. However, the study is limited to its range of Reynolds number from $0.6 < \mathrm{Re} \leq 200$, and assumes no deformation in the bubble shape [20].

Previous studies of virtual mass used potential flow theory to derive a virtual mass coefficient for bubbly flows, but did not include the influence of bubble wakes on the motion of bubble swarms. Sankaranarayanan et al. used a Lattice Boltzmann method to numerically model a bubble's conservation equations [21] to compute virtual mass coefficient on bubble swarms of spherical, ellipsoidal, and spheroid bubbles shown by eq.(26).

$$C_{VM} = \frac{1}{2}\left(0.37\mathrm{Ta} + 1\right) \tag{26}$$

$$\mathrm{Ta} = \mathrm{Re}\,\mathrm{Mo}^{0.23} \tag{27}$$

Simulations were performed for various Tadaki numbers, eq.(27), to obtain a linear fit for virtual mass coefficient of a single bubble. They noted that the aspect ratio of a spheroid/ellipsoidal bubble can be correlated to a single bubble's virtual mass coefficient and can account for variations produced by different Weber and Eötvös numbers. However, aspect ratio was determined to not be an appropriate measure to estimate virtual mass in uniformly spaced bubble swarms [21].

Ohl et al. investigated the effect of bubble expansion on the added mass. This was performed with a bubble force balance that allowed the bubble diameter to change with respect with time and resulted in eq.(28).

$$\frac{dU_g}{dt} = 3\frac{dU_f}{dt} - \frac{3}{R}\frac{dR}{dt}\left(U_g - U_f\right) + 2g - \frac{3}{4}\frac{C_D}{R}\left|U_R\right|U_R \tag{28}$$

Equation (28) modeled the added mass contribution with the inclusion of the second term on the right hand side. An experiment with an air bubble injected into a stagnant tank was used to compare the added mass modeled with eq.(28), and eq.(28) without the second right hand side term. The added mass model including the bubble expansion had good agreement with the rise velocity while the omitted model consistently over predicted the rise velocity [22].

Zhang et al, examined the impact of the virtual mass coefficient correlation presented by Tomiyama with a numerical comparison [11] to experimental data from Deen as previously described in section 2.1. The correlation used by Tomiyama [12] is shown with eq.(29):

$$C_{VM} = \frac{\cos^{-1}\mathrm{E} - E\left(1-\mathrm{E}^2\right)^{0.5}}{\left(2\mathrm{E}^{-1} - \mathrm{E}\right)\left(1-\mathrm{E}^2\right)^{0.5} - \cos^{-1}\mathrm{E}} \tag{29}$$

$$\mathrm{E} = \frac{1}{1 + 0.163\mathrm{Eo}^{0.757}}$$

where C_{VM} is the bubble's virtual mass coefficient, and E is a function of the Eötvös number. The rise velocity for the liquid and gas phases were compared between the measured velocity data and the use of three different virtual mass coefficient inputs. The inputs were a virtual mass coefficient of zero, the traditional $C_{VM} = 0.5$ value, and the coefficient calculated with eq(29). The study showed that there was no notable difference between either virtual mass coefficient correlation used, and suggested that the large impact of the interfacial lift force as the likely reason for no impact from virtual mass [11].

Kendoush derived a semi-analytical correlation for virtual mass coefficient for oblate-ellipsoidal bubbles noting that virtual mass changes based on shape. This led to virtual mass coefficients for spherical cap bubbles, but few solutions for ellipsoidal bubbles. As a result the author derived eq.(30):

$$C_{VM} = \left\{ 2\left[1 - \left(\frac{6.613}{64}\right)\mathrm{We}^2\right]^3 \left[1 + \left(\frac{3}{32}\mathrm{We}^2\right)\right]^2 \times \left[1 - \left(\frac{3}{16}\right)\mathrm{We}^2\right] \right\}^{-1} \tag{30}$$

$$\mathrm{We}^2 = \frac{\mathrm{Ta}\left(\frac{\mathrm{Re}}{\mathrm{Eo}}\right)^{\frac{1}{3}}}{\mathrm{Mo}^{0.103}}$$

As the Weber number approaches zero it results in the traditional $C_{VM} = 0.5$ value from potential flow theory. The semi-analytical correlation had good agreement with the work from Sankaranarayanan et al. up to a Tadaki number of 4.75 [23].

The virtual mass force is often included in simulations to add numerical stability [24]. Numerical instability can occur because the two-fluid model is an ill-posed system of partial differential equations (PDEs) and needs constitutive modelling. RELAP5/MOD3.3 includes virtual mass but neglects the spatial derivatives of the flow's material derivative [25]. The truncated form of the virtual mass force in RELAP5/MOD3.3 was compared to the Pauchon and Banerjee Model (P-B Model), which uses the material derivatives in eq.(21), with experimental data from Bernier which injects 5 mm bubbles into flow with varying liquid velocities [26]. For high void fractions RELAP5/MOD3.3 was seen to have PDEs more well-posed than the P-B model. Additionally, the RELAP5/MOD3.3 had slight over predictions of the experimental data which was attributed to the models choice of drift velocity correlation and not the truncated virtual mass force. However, Fullmer et al. did note that solutions still become unstable at high enough liquid fluxes.

2.3 Two-Phase Experimental Techniques

There are numerous instruments used to measure relevant two-phase flow parameters such as interfacial area concentration, and liquid and gas velocities. Conductivity probes have been used to measure interfacial area concentration and gas velocities. Common ways liquid velocity is measured is with a rotameter, electromagnetic flow meter, hot wire anemometry, Laser Doppler Anemometry (LDA), or particle image velocimetry (PIV), although this list is not exhaustive.

Hot wire anemometry (HWA) uses a very thin heated wire placed perpendicular to the main flow. The wire temperature is monitored with a thermocouple, and because of the cross flow over it causes convective heat transfer to occur along the wire. Typically, HWA uses a controller to keep the temperature of the wire constant, this is achieved by adjusting the voltage in a bridge and amplifier circuit. The flow velocity is then correlated to the bridge voltage [27]. Hot wire anemometers can provide different components of velocity based on how many wires are being used, one wire corresponds to one component of velocity, where a 3-wire anemometer can provide full 3-D information on the velocity vector.

Double-sensor and four-sensor conductivity probes developed by Kataoka [28] have been used to measure the interfacial area and interfacial velocity of the vapor phase in two phase flow. For double-sensor probes, two parallel thin electrodes are offset by a known distance with the impedance measured between the probe tip and a common ground [29] When a vapor bubble passes through a wire, the difference in conductivity in the vapor compared to the liquid produces an increase in measured impedance. When the vapor bubble passes through the second wire it causes another pulse. The time between pulses and distance between wires is used to determine velocity. Limitations to the double-sensor include the requirement of spherical bubbles and a statistical approach to account for bubbles that miss one electrode [29]. The four-sensor conductivity probe can provide three components of interfacial velocity at a point but suffered from a large size which made it ineffective for flows with small bubbles. As a result, a miniaturized probe was developed to overcome the size restriction [30]. Dang et al. used the miniaturized four-sensor conductivity probe to measure interfacial velocity, interfacial area concentration, and Sauter mean diameter with a total instrumentation uncertainty of ±11.9% [31].

Laser Doppler anemometry (LDA)/ laser Doppler velocimetry (LDV) is a non-intrusive measurement technique with a probe volume made up of laser beams and uses the Doppler effect to determine velocity. There are four main operational modes of LDA/LDV: spectrometer, reference beam, one beam, and fringe systems. The most widely used operation mode is the fringe system, which uses a laser beam split into two coherent beams which are crossed to create a fringe pattern with equally spaced bright and dark planes. A particle in the flow moves across this fringe pattern which scatters the light from the fringes to a photodetector which records the frequency the signal. Multiplying the signal frequency by the distance between fringes results in an instantaneous velocity measurement [32]. The spacing of the fringes are proportional to particle's velocity and velocity magnitude determined is normal to the fringe probe volume.

Advantages of LDA/LDV are the non-intrusive capabilities which are well suited to transonic, supersonic, and combustion flows. It can provide high spatial and temporal resolution with sample times on the order of a few microseconds and a probe volume smaller than the smallest turbulent flow scale. Disadvantages of using an LDA/LDV system is that it provides only local point measurements, requires optical access, and does not provide velocity information regarding the flow field or flow structure [32].

Particle image velocimetry (PIV) is a non-intrusive laser measurement technique which is capable of providing spatially resolved flow velocities and qualitative flow visualization [3]. The basic working principle for PIV is the use of a high-powered light source to illuminate tracer particles suspended in a flow. The light is refracted by the tracer particles and recorded by a high-speed camera. Velocity field measurements are generated by observing the displacement of tracer particles between two frames recorded with a high-speed camera, such as a CCD or CMOS camera. The field of view is discretized into "interrogation windows" which are represented as a specific pixel resolution. The light scattered off of tracer particles is recorded as an intensity field. Image processing uses these intensity fields to determine the best statistical match of the image pairs. A correlation function uses these image pairs to produce a displacement vector; in addition, given the time between the two frames and the displacement vector, a velocity vector can be built. Repeating this process across all the interrogation windows enables the velocity field to be constructed.

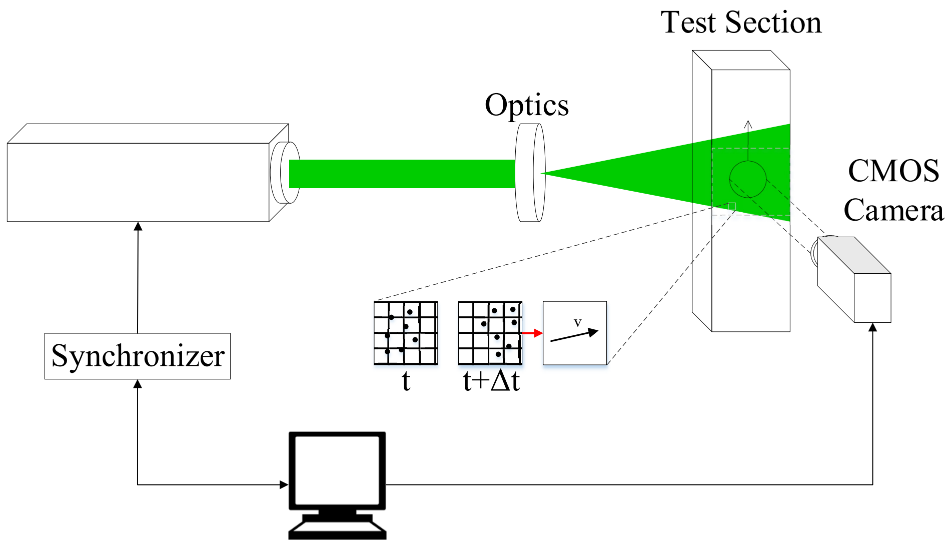

Figure 3: Typical PIV Planar System

As with LDA/LDV systems, PIV does not provide direct measurement of the fluid but instead measures the seeding particles' velocity. This makes accuracy of the velocity field dependent on the particle used to seed the flow. Unless the density of the tracer particles matches the fluid exactly, there will always be an amount of settling or rising of the particles. This is described as the velocity "slip" error between the particles and the fluid [33]. Equation (31) shows the velocity "slip" difference:

$$v_p - \mathbf{u} = \frac{\bar{\rho} - 1}{\bar{\rho}} g_o \tau_o \tag{31}$$

where v_p is the particle velocity, $\boldsymbol{u}$ is the flow velocity, $\bar{\rho}$ is the particle density, g is the gravitational constant, and τ_o is the time constant associated with the flow. This slip error can be associated with the Stokes Number (St):

$$\mathrm{St} = \frac{u_o \tau_p}{l_p} \tag{32}$$

where u_o is the flow velocity, τ_p is the particle relaxation time constant, and l_p is the particle's characteristic length. The Stokes number is used to describe how well particles can follow the streamlines of a flow. Particles that have a $\mathrm{St} \ll 1$ are able to accelerate with the fluid when the flow changes, and able to match the streamlines very well which implies a reduction in velocity slip [34].

Brücker investigated the wake structure of rising spherical bubbles with a helical or zig-zag pattern with Reynolds numbers up to Re=700 with a PIV system. The system used a continuous Ar-ion laser. It was noted that it was impossible to eliminate out of plane motion with bubbles rising in stagnant liquid. This resulted in a scanning laser sheet method to vary the vertical laser sheet's horizontal position to ensure bubbles were mostly in the laser sheet and prevent out of plane motion issues. A high-speed camera was used at a 400 Hz framerate with a 512 x 512 pixel resolution and 512 number of frames. The field of view was 3 x 6 cm^2 with interrogation window size of 32 x 32 pixels [35]. While the author was able to account for the presence of the bubble in their cross-correlation method, the only uncertainty estimation mentioned in the study was a maximum 5% uncertainty on determining the y-coordinate of a bubble's centroid. Brücker also noted that the use of tracer particles acts as contaminants and causes the bubbles to behave as they would in a contaminated system.

Deen examined 4 mm rising bubbles in a stagnant tank with PIV using rhodamin-B florescent tracer particles with a 75 μm diameter and 15 Hz Nd:YAG pulsed laser with a laser sheet 3 mm thickness. Images were captured with two Kodak Megaplus ES 1.0 cameras with a 1008 x 1018 pixel resolution. One camera used an orange optical filter to filter out light with a wavelength below 590 nm and the other camera used a band pass filter to allow the 532 nm wavelength laser light to be captured which detected the gas phase. The PIV algorithm used in the analysis was compared to a synthetically generated

PIV image and compared the ability for the algorithm to calculate velocity fields to match the synthetic image, but an uncertainty on the velocity measurements was not presented.

Hosokawa et al. calculated the pressure distribution around solid single spherical particles and single bubbles in Reynolds number ranges from $20 \leq Re \leq 61$ in a glycerol-water solution with a 4 Watt Ar-ion laser PIV system to produce a 1.2 mm thick laser sheet. A pump was used to run counter current flow from the top of a test section to make the rising bubble stationary in the field of view. The test section was a square rod with a 30 mm diameter cylindrical hold to allow undistorted optical access with a round flow channel which allowed a two-dimensional axisymmetric flow assumption. The system measured the velocity of 3 μm diameter sized silicon dioxide tracer particles with a CCD camera with 1024 x 1016 pixel resolution. Velocity measurements obtained had uncertainties of less than 5% which resulted in a maximum 20% error in the evaluated pressure distributions [36].

Ortiz-Villafuerte, et al used a PIV system to evaluate drag and lift coefficients of ellipsoidal bubbles in rising stagnant water over a Reynolds number range of $400 \leq Re \leq 650$. Air bubbles were injected into a 12.7 mm inner diameter pipe which resulted in wall effects contributing . Three charged couple device (CCD) cameras were used to recorded the PIV images, each camera had a maximum resolution of 640 x 480 pixels with a resolution of 640 x 240 pixels for a 60 fps framerate with a 12.7 mm horizontal field of view [37]. The measured velocities in the axial direction had a reported 3% uncertainty and calculated drag coefficients had a reported 7% uncertainty. Large uncertainties on the lift coefficient led the researchers to note that cameras with resolutions larger than 1000 x 1000 pixels and higher framerates would greatly assist with reducing experimental uncertainty [37]. Visualizing the movement of a discontinuous vapor phase in a liquid has been performed with high speed cameras in past studies. Haberman and Morton used a close-up lens camera that had film speeds of 25, 50, and 35 frames per second with a 1.4 x 1.8 to 1.75 x 2.3 [in.] field of view [4] which was a comparable setup for Ortiz-Villafuerte et al.

2.4 Summary

Drag coefficient for single bubbles has primarily focused on spherical shapes without much consideration for the effects of shape deformation. Drag coefficient correlations have been well developed for Reynolds numbers typically below $\mathrm{Re} < 10^2$, above $\mathrm{Re} \geq 10^4$ which is a known constant value, and has been under examined in the order of magnitude range of $10^2 < \mathrm{Re} < 10^3$. Research into the virtual mass force on bubbles has primarily used potential flow theory with some work looking into bubbles in viscous flows. Correlations developed to model the virtual mass coefficient collapse down to Lamb's analytically derived value which is typically used to approximate the virtual mass coefficient in computer codes. Similar to drag coefficient, the virtual mass coefficient has been studied for a range of low Reynolds numbers with few experimental studies performed. Studies for both coefficients that have relied on experimental databases to evaluate the analytical, semi-analytical, and empirical correlations developed typically did not report instrument uncertainty which affects the ability to quantify error in computer code validation studies.

Two phase flow measurements have typically relied on point measurements, however LDA is capable of providing a non-intrusive measure. Particle image velocimetry has been used to non-intrusively study bubble flows to observe flow dynamics and velocity fields. These studies investigated rising air bubbles in either stagnant or flowing water systems within the range of Reynolds numbers observed for previous drag and virtual mass coefficient experiments. A majority of the PIV studies have suggested using higher camera resolution and framerate to greatly reduce experimental uncertainty. The suggested experimental improvements and review of relevant literature has shown a region of interest that will be investigated with this study.

3 EXPERIMENTAL FACILITY

This study was performed with the Bubble Investigation Loop (BIL), shown in Figure 4, which is a non-heated recirculating water flow loop. The loop uses a rectangular acrylic test section which provides optical access to the flow. This test section has a bubble injection system attached to the bottom of the section which can inject varying sized bubbles into the flow and imaged with the PIV system. A pump is used to recirculate counter-current flow to the bubble rise and controls a bubble's rise time. The PIV system includes a high-speed camera mounted perpendicular to one of the test sections sides, a laser is positioned to send a light sheet into the test section which is also perpendicular to the camera. In addition to the PIV system, other instrumentation includes a thermocouple, flowmeters, static pressure transducer, and a differential pressure transducer provide supplementary flow information needed to obtain thermophysical properties of the fluid.

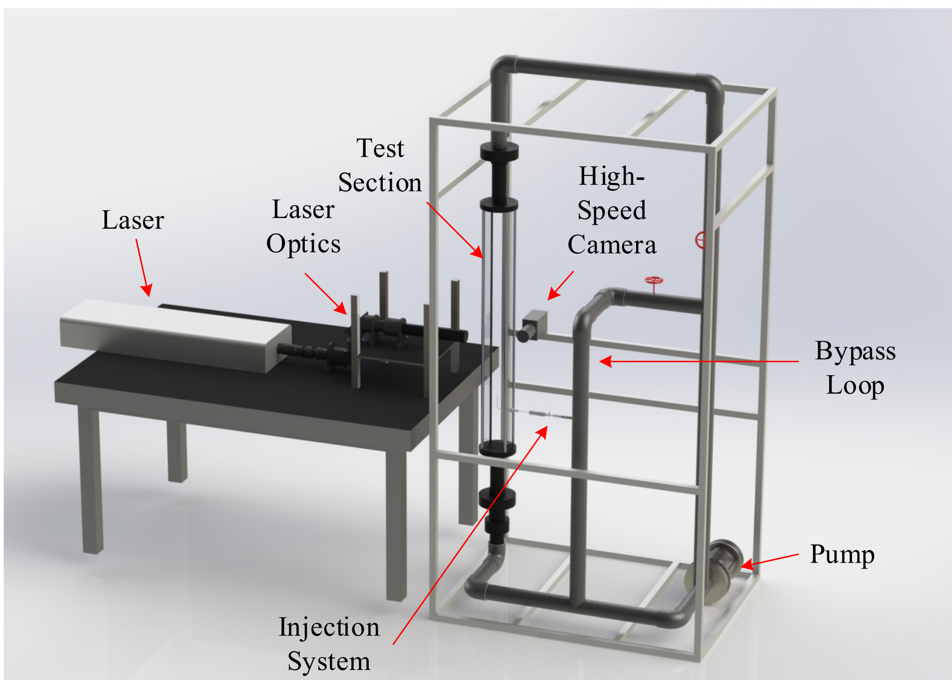

Figure 4: Bubble Investigation Loop

3.1 Facility Description

The facility design is centered on the acrylic test section used to investigate the rising bubbles. Acrylic was chosen for its low cost and optical access with a similar refractive index to water. The test section has a 3in. x 3in. inner cross section, 3/8 in. wall thickness, and 40 in. height. This cross-sectional area was chosen to minimize wall effects on the bubbles and manufacturing cost; while the height was selected to reduce entrance effects from the inlet at the top of the test section.

Flow is circulated up through the piping on the pump's discharge side to the top of the facility and down through the test section to provide counter-current flow on injected bubbles rising. Flow rate is controlled using a Variable Frequency Drive (VFD), additional flow control is provided with a bypass loop which can redirect a portion of the flow back to the pump suction side without having to travel through the test section.

3.2 Instrumentation

Thermophysical properties for the fluid flow were obtained using pressure and temperature instruments. Table 1 lists the instrument specifications. An Omega K-Type thermocouple with a 304 SS sheath and 1/16" diameter was used to record temperature on the pump suction side. Because the BIL is an unheated system only one thermocouple was used. An Omega gauge pressure transducer was located next to the thermocouple for installation ease, and an Omega PX-409 differential pressure transducer has its instrument line taps also on the pump suction side and immediately after the pump discharge side. This location was selected because the minimum and maximum pressures in the system occur there. Instrumentation readings were recorded using a National Instruments (NI) cDAQ-9174 chassis and LabVIEW software. The uncertainty of a single measurement can be evaluated by taking the square root of the sum of the squares of sources of uncertainty which is shown in eq. (33), where σ_x is the uncertainty for a measured value, and σ_i, σ_j, and σ_k are various sources of uncertainty.

$$\sigma_x = \left(\sigma_i^2 + \sigma_j^2 + \ldots \sigma_k^2\right)^{0.5} \tag{33}$$

This takes the square root of the sum of the instrument and data acquisition system (DAQ) errors squared. The instrument error is approximated from the accuracy reported by the manufacturer and the DAQ error comes from the reported errors from the NI modules used to record the instruments signals. Because the instruments are connect to a DAQ, the resolution error is instead the quantization error associated with the number of bits the module can use to record values. When determining the uncertainty contributed from the NI modules, quantization error was neglected due to its uncertainty values being on the order 10^{-6} which was substantially smaller than the modules' gain and offset errors. It is important to specify that the uncertainty for the flowmeters neglects the DAQ uncertainty from its corresponding NI-9205 module. The reasoning for neglecting the DAQ uncertainty is based on how flowrate is calculated. The turbine flow meters generate voltage pulses from a magnetic tip on the turbine blade passing a pick coil hosed in the meter. This voltage pulse is read by the NI-9205 module and sent to LabVIEW. A LabVIEW application performs a Fast Fourier Transform (FFT) on the voltage signal to determine a pulse rate which is then multiplied by a calibration factor to convert pulse rate to flow rate. Because the flow meters are not critical instruments, did not provide data used in any calculations, the difficulty in prorogating uncertainty through an FFT analysis, and the low uncertainty of the module itself, the DAQ uncertainty was neglected when evaluating the flow rate uncertainty. Additionally, the meters provided a qualitative check to identify the major flow path when the bypass loop was opened to prepare the flow loop for testing.

Table 1: Instrumentation Specification

Instrument	Manufacturer	Model Number	Range	Instrument Uncertainty
K-Type Thermocouple	Omega	KMQSS-062U-4	–270 to 1372°C	±2.2°C
Differential Pressure Transmitter	Omega	PX-409-030DWUI	0-30 psi	±0.08% of reading
Gauge Pressure Transducer	Omega	MMG030C1P4C0T3A5CE	0-30 psig	±0.20% of reading
Flow Meter	Omega	FTB-103	1.25-9.5 gpm	±0.5% of reading
Flow Meter	Omega	FTB-108	8-130 gpm	±0.5% of reading

Table 2: Data Acquisition System Uncertainty

Module	Manufacturer	Model Number	Range	DAQ Uncertainty	Uncertainty Value
Current Input	National Instruments	NI-9208	±22 mA	Gain	± 0.167 mA
				Offset	± 0.0088 mA
				Total:	**± 0.228 psi**
Voltage Input	National Instruments	NI-9205	±10 V	Gain	± 4.76 mV
				Offset	± 1.40 mV
				Noise	± 0.072 mV
				Total:	**± 6.23 mV**
Thermocouple	National Instruments	NI-9214	±78.125 mV	Gain	± 0.117 mV
				Offset	± 0.008 mV
				Noise	± 0.22 µV
				Total:	**±0.3625°C**

3.3 Particle Image Velocimetry System

The primary measurement technique used in this study was a Dantec Dynamics PIV system. This system consists of the following main components: laser, laser optics, high speed camera, speeding particles, synchronization and timing box. Dantec DynamicStudio software was used to control the laser, camera, and synchronization. The laser and camera specifications are listed in Table 3 and Table 4 respectively. Optics supplied from Dantec Dynamics are used to diffuse the beam into a laser sheet. The SpeedSense camera operated at a 1920 x 1200 resolution, with a 400 Hz framerate, and could store a maximum of 427 image-pairs. Spatial calibration was performed by lowering a 0.75 inch ball attached to the base of a 0.25 inch diameter rod into the PIV field of view where an image capture could be taken and used to measure the scale factor. Polymethyl-methcrylate (PMMA)-Rhodamine-B fluorescent tracing particles ranging from 1-20 µm diameter were used to seed the flow and eliminated glare from the bubbles by using an optical filter that only allows the fluorescent wavelength emitted by the particles after receiving the light sheet. The particles gave the water a pink hue as visible in Figure 5 and Figure 6.

Table 3: PIV Laser Specifications

Manufacturer	Litron Lasers Ltd.
Model	LDY304 PIV
Type	Nd:YLF
Wavelength Emitted	527 nm
Pulse Duration	100 ns
Pulse Frequency	0.2-20 kHz (each cavity)
Maximum Power	150 W
Beam Diameter	5 mm
Beam Divergence	< 3mrad

Table 4: High-Speed Camera Specifications

Manufacturer	Phantom
Model	Miro320S SpeedSense
Camera Sensor	CMOS
Resolution	1920 x 1200
Pixel Size	10 μm
Bit Depth	12
Frame rate	400 fps
Maximum Framerate @ Max Resolution	1380 fps

3.4 Bubble Injection System

The injection system needed to repeatedly inject bubbles of known volume into the flow field. Figure 5 and Figure 6 show the injection system's components comprised of a syringe, tubing, and a coalescence device. A 5 mL capacity syringe and 0.5 mL capacity syringe were used to allow variable bubble. In both figures, the syringe is attached to a three-way valve which allows the syringe to be filled with air and opened to inject the air into the test section. The coalescence device allowed injected bubbles to form larger bubbles instead of dispersing a stream of small bubbles which can be rotated to release the bubble into the flow field.

A range of bubble volumes were achieved based on the use of two different syringes and accompanying tube sizes with specifications shown in Table 5. The expected minimum spherical equivalent bubble diameter was determined using Tate's Law [38], shown in eq (34),

$$d_{\mathrm{b}} = \left(\frac{6 d_{\mathrm{n}} \sigma}{g \Delta \rho} \right)^{\frac{1}{3}} \tag{34}$$

where d_{b} is the spherical equivalent bubble, d_{n} is the tube diameter the bubble emerges from, σ is the surface tension, $\Delta\rho$ is the density difference between bubble and fluid, and g is the gravitational constant. This equation is used to estimate the diameter a bubble will form based on the tube diameter it is injected from. This was used to determine the minimum volume from a syringe that can be injected before a bubble is formed. The different syringes provide different levels of resolution which aids in keeping instrument uncertainty for the syringes lower when dealing either small or larger bubbles. The resolution uncertainty was approximated as half of the syringe's resolution.

Table 5: Bubble Injection System Specifications

Setup Parameter	**Setup 1**	**Setup 2**
Syringe Capacity	0.5 mL	5 mL
Resolution	0.005 mL	0.1 mL
Resolution Uncertainty	± 0.0025 mL	± 0.05 mL
Tube OD	1/16”	1/8”
Wall Thickness	0.02”	0.028”
Minimum Bubble Diameter	2.9 mm	4.8 mm

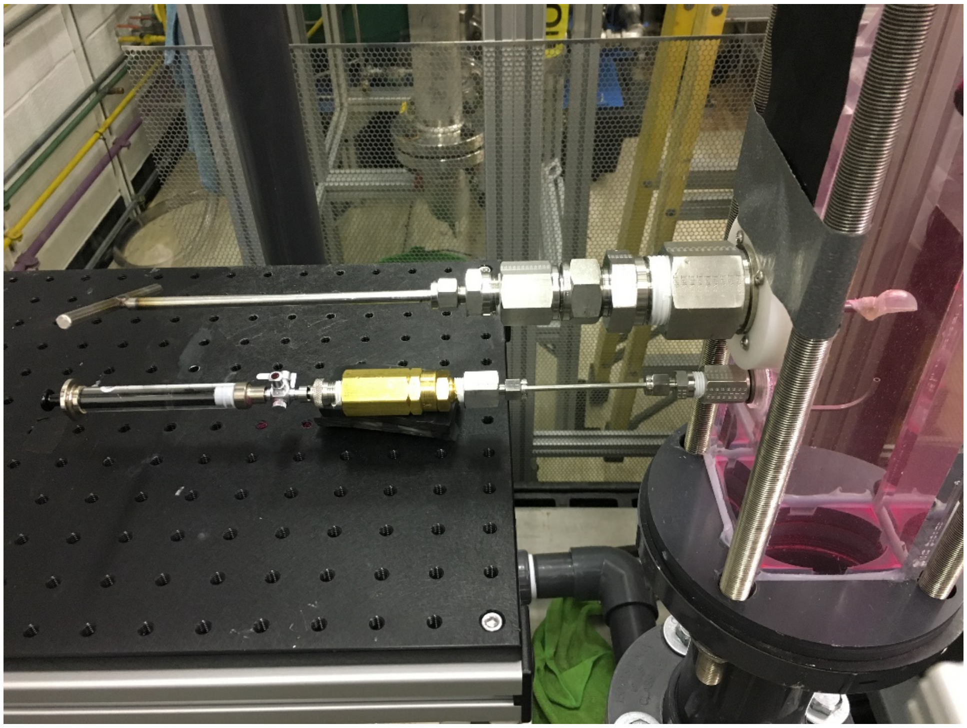

Figure 5: Injection System with 5 mL Syringe

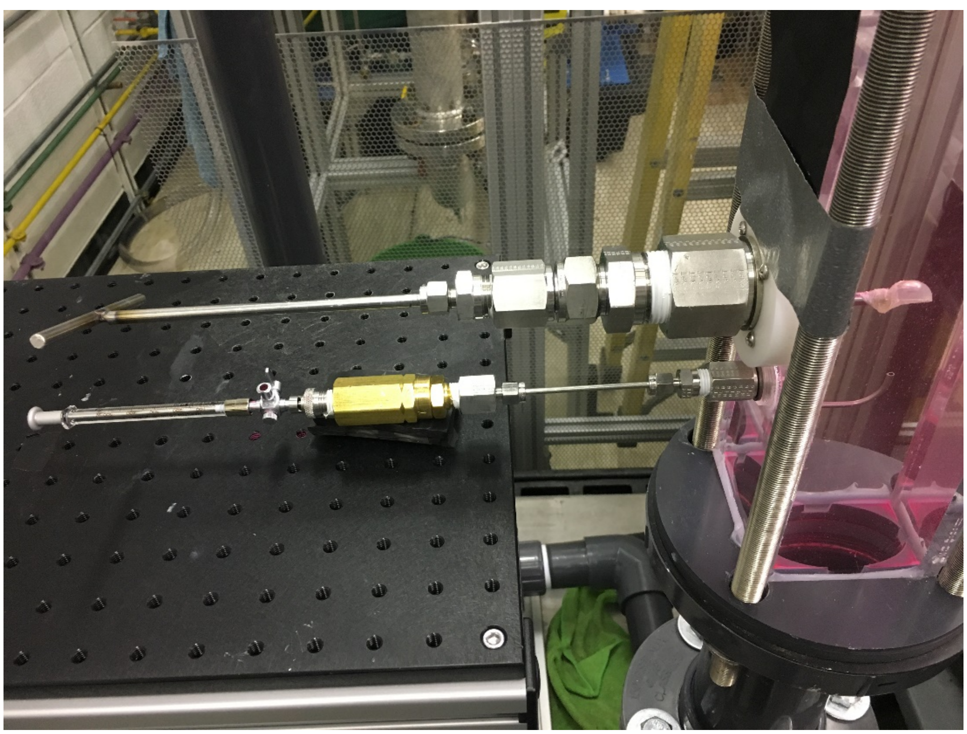

Figure 6: Injection System with 0.5 mL Syringe

4 METHODOLOGY

A method has been developed to acquire instantaneous velocity fields around a bubble and calculate its associated drag coefficient and virtual mass reported on a Reynolds number basis.

Prior to every data collection, a calibration image of the 19.05 mm ball in the field of view was captured. This calibration image provided the particle pixel displacement length scale when evaluating velocity. The bubble images were acquired with the PIV and bubble injection systems described in. A known bubble volume is injected into the coalescence device. The Rhodamine-B seeding particles have a slightly larger density than water which made settling more noticeable. The pump was run to ensure mixing of the particles in the fluid occurred prior to any data collection. The Dantec Dynamic software allows the particle density to be calculated and was used to ensure the recommended 8-10 particles per interrogation area [3] was achieved. The pump would continue to provide counter current flow at roughly 100 mm/s to the injected bubbles which stabilized the helical rise and increased its time in the camera's field of view. This flow speed choice was determined from visual inspection and balanced stabilizing the bubble's rise while not changing the rise trajectory because of the turbulent flow characteristics. Once the coalescence device was rotated to release the bubble, the PIV system was initiated to capture the image pairs of the bubble while it moved through the field of view. The system used a high frame collection rate of 200 Hz with a 1 ms time between each laser pulse for an image pair.

Because the bubble is not included with the particles when analyzed in the correlation method, the bubble is masked and not treated as a region of interest for the correlation method. This prevents unrealistic and erroneous velocity vectors from being produced due to an interrogation area going from a defined seeding density to no seeding density where the bubble is located. After masking the bubble, the Dantec Dynamics DynamicStudio software calculated the velocity field for each image pair. In PIV, the velocity is calculated by performing a spatial correlation, also known as a cross-correlation. During data collection, two quick successive images are captured and treated as an image pair with each frame having an associated light intensity distribution across it which appears as the greyscale image. The location of light intensity peaks represents the physical location of the tracer particles. The image frames are divided into interrogation area windows where a cross correlation is performed on each interrogation area. The cross correlation between the two exposed image frames is performed in each interrogation area with eq. (35) which calculates correlation coefficient between the intensity peaks location in each image frames interrogation area.

$$R(\boldsymbol{s}) = \int \tau_1(\boldsymbol{X})\tau_2(\boldsymbol{X}+\boldsymbol{s})d\boldsymbol{X} \tag{35}$$

where τ_1 and τ_2 are the weighted light intensity distributions for the interrogation area in frame 1 and frame 2, $\boldsymbol{X}$ is the position vector of the intensity peak, and $\boldsymbol{s}$ is the displacement vector of the intensity peak between the two frames. The maximum correlation coefficient, $R(\boldsymbol{s})$, represents the average in-plane displacement and provides the two velocity components for the flow in that interrogation area. Figure 7 shows an example correlation map with a high peak located off the center which provides the displacement vector of the particles in this interrogation area. The correlation map also shows the ratio of the highest peak to the second highest peak, referred to as the SN ratio, and provides the normalized height of the maximum peak.

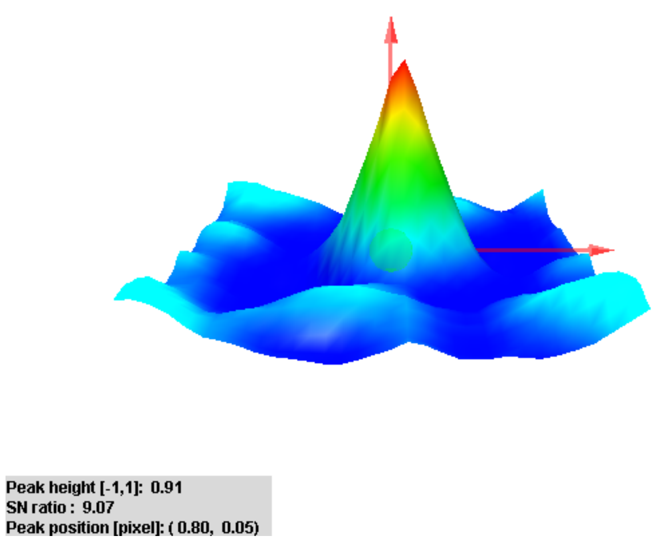

Figure 7: Example cross-correlation map

The software used an adaptive-PIV correlation which performs a cross correlation and iteratively adjusts the size and shape of interrogation areas to ensure a predefined seeding density in that interrogation area is achieved. A maximum and minimum pixel interrogation area size of 64x64 and 16x16 were specified respectively, where the first iteration of the analysis uses the maximum interrogation area and subsequently can divide the interrogation area by two after each iteration if the seeding density is higher than the predefined seeding density value. A peak height validation process and correlation peak signal to noise ratio was used to accept, reject and substitute rejected spurious velocity vectors. The peak height validation process input defines a minimum height that a correlation peak must be above to be accepted. The correlation peak signal to noise ratio takes a ratio of the tallest and second tallest correlation peaks and evaluates them against another user defined input. A ratio greater than or equal to the input results in an accepted vector. A signal to noise ratio of 2 was selected based on recommendations of threshold values of 1.2 [39]and 2 [40] being able to reliably avoid spurious vectors being accepted. The correlation method requires that both the peak height and signal to noise ratio processes pass to accept the calculated velocity vector. The exported data contains the Cartesian coordinate of the vector, x and y velocity components, and status to indicate if the vector is original, substituted, or rejected. The rejected status is used to indicate what region in the image had been masked.

4.1 Drag Coefficient

The drag force and respective coefficient are determined by calculating the total drag and form drag. The total drag force has been traditionally calculated by the steady state force balance between the buoyancy and drag force as seen in eq. (36)-(37). This force balance is used to directly calculate the total drag coefficient, eq.(38), which only requires the estimation of the equivalent spherical bubble diameter and the relative bubble velocity. This approach is consistent with past studies methodology [4].

$$F_B = F_D \tag{36}$$

$$\frac{\pi}{6}\left(\rho_f - \rho_g\right) g D_e^3 = \frac{1}{2} C_D \rho_f \left(\frac{\pi}{4} D_e^2\right) \mathrm{v}_r^2 \tag{37}$$

$$C_D = \frac{4}{3}\frac{\left(\rho_f - \rho_g\right) g D_e}{\rho_f \mathrm{v}_r^{\ 2}} \tag{38}$$

Because PIV has the ability to measure the velocity distribution around the bubble, it allows the force distribution surrounding the bubble to be calculated. This can provide direct calculation of the form drag and allows the contribution of skin drag for each bubble to be determined as well by subtracting the form drag force from the total drag. The form drag coefficient is calculated using eq.(39), where the force $F_{D,\mathrm{form}}$ is obtained by the surface integral of the pressure field surrounding the bubble.

$$C_{D,\mathrm{form}} = \frac{F_{D,\mathrm{form}}}{\frac{1}{2}\rho_f \left(\frac{\pi}{4} D_e^{\ 2}\right) \mathrm{v}_r^{\ 2}} \tag{39}$$

The surface integration for force $F_{D,\mathrm{form}}$, is shown in eq. (40), which requires the pressure field P around the bubble surface.

$$\vec{F} = -\iint \left(P \cdot \hat{n}\right) dS \tag{40}$$

The pressure field can be determined from a rearrangement of Navier-Stokes equation for the pressure gradient term, eq.(41), and then integrated between two points, eq.(42).

$$\nabla P = -\rho \left(\frac{D\vec{\mathrm{v}}}{Dt} - \nu \nabla^2 \vec{\mathrm{v}}\right) \tag{41}$$

$$P_2 - P_1 = \int_{x_1}^{x_2} \nabla P \mathrm{d}x \tag{42}$$

The velocity components, location and mask location were imported into the queen2 algorithm, developed by Dabiri et al. [41], which calculates a pressure field and was developed to handle “substantial body deformation characteristics” [42] and was verified against swimming deformable bodies such as jellyfish. This algorithm and application was considered ideal to handle the unstable bubble surface. The algorithm integrates the Navier-Stokes equation along a line integral to calculate the pressure at a point in the field of view. The pressure at a single location in the field of view is evaluated by performing eight line integrals from the left, right, top, bottom boundaries and from the upper left, upper right, lower left, and lower right regions of the field of view. The pressure is determined from a median polling to reduce the sensitivity to outliers. The median polling takes the top two median values and averages them to obtain the final pressure value at the location point of interest. This process is repeated at every velocity vector location in each frame. Because the algorithm calculates the velocity's material derivative, it truncates the last frame to implement the finite differencing scheme that evaluates the temporal derivative in the material derivative. An important element of the algorithm is its assumption of a zero pressure boundary condition at the edge of the field of view which results in final calculated pressures relative to this zero pressure boundary. However, this limitation on the pressure field calculation does not impact this study because the force on the bubble only relies on relative pressure differences

A Matlab script was used to perform a numerical surface integral of the pressure along the bubble's masked boundary. First a line integral is numerically approximated by multiplying the pressure value by the horizontal and vertical cell widths to obtain the vertical and horizontal force per length components respectively in each cell along the bubble mask. Subsequently, an azimuthal symmetry assumption was made to complete the surface integral and calculate the force exerted on the bubble. This required obtaining the masked bubble's centroid and determining the surface cell's distance from the centroid to each location along the two-dimensional bubble surface. The force per length value at each bubble surface position was rotated about the centroid's axis to complete the surface integral. Figure 8 shows an example revolution of each side of the masked bubble image. Because pressure information is provided on both sides of the bubble mask, each side is rotated 180 degrees as shown with the black and red arrows with their respective revolution paths. This preserves as much of the original geometry provided by the planar image; however it does not represent the true bubble surface area and is a limitation of using planar PIV.

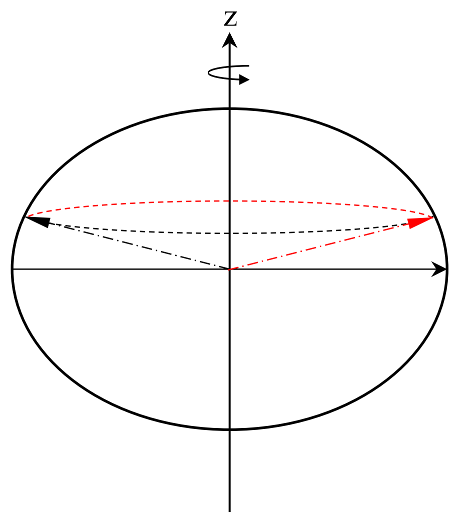

Figure 8: Pressure surface integral geometry diagram

This assumption was considered necessary because planar PIV prevents information from being known outside of the light sheet plane. The bubble velocity was found by tracking the bubble mask's centroid and using the distance travelled between frames to obtain the bubble's horizontal and vertical velocity components. Because the drag force acts opposite to the direction of motion, the bubble velocity components were used to find the unit vector opposite of the bubble's direction. Figure 9 shows an example vector component breakdown for determining the unit vector and the dot product between the calculated force on the bubble and the unit vector to determine the form drag force contribution (highlighted in red) to the net force.

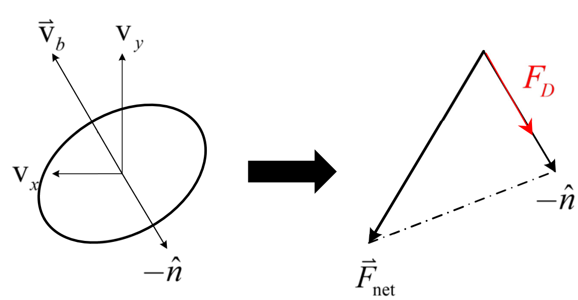

Figure 9: Example drag force component determination

After determining the form drag force components and net force, the drag coefficient could be found with eq.(39). It is important to specify that the cross-sectional area was based on the bubble's spherical equivalent diameter to provide a consistent reference area. This assumption introduces a source of error in the drag coefficient calculation since the cross-sectional area of the ellipsoidal/distorted bubbles do not match. Because the equivalent surface area is based on a sphere of the same volume, it will produce a larger projected cross-sectional area. This will cause the calculated drag coefficient to be under predicted. However, it is typical to report drag coefficient against the spherical equivalent Reynolds number to allow a consistent comparison of different experimental databases. This process was repeated for each frame in a trial and time averaged to produce an average drag coefficient for each trial with a specific spherical equivalent bubble diameter.

4.2 Virtual Mass Coefficient

The virtual mass coefficient is a non-dimensional form of the added mass a bubble carries with it after an acceleration or deceleration. The virtual mass coefficient has traditionally been treated as the analytical $C_{VM} = 0.5$ value derived from a spherical potential flow's kinetic energy. The added mass represents the influence of an object to the fluid's original kinetic energy. Lamb's derivation [43] of the spherical potential flow case used eq (43):

$$KE_f = -\frac{1}{2}\rho_f \iint \phi \frac{\partial \phi}{\partial r} dS \tag{43}$$

where ρ_f is the fluid density, ϕ is the potential flow function for a sphere, and the integration is performed over the sphere's surface area. The surface integration was converted from a volume integral over the entire fluid domain using Greens Theorem. This step allowed an easier analytical integration to be performed by changing the reference frame to the sphere as opposed to the fluid domain. Because these two integrals are equivalent, the kinetic energy of the fluid can be found by numerically integrating the kinetic energy in each discretized cell of the flow domain as shown in eq. (44)-(46)

$$KE_f = \frac{1}{2} m_a U^2 \tag{44}$$

$$\frac{1}{2} m_a U^2 = \sum_{i=1}^{\#\text{of cells}} \frac{1}{2} m_i \left(u_i^2 - U^2\right) \tag{45}$$

$$m_a = \sum_{i=1}^{\#\text{of cells}} \rho_f \Delta x_i \Delta y_i \left(\pi r_i\right) \frac{\left(u_i^2 - U^2\right)}{U^2} \tag{46}$$

where Δx_i and Δy_i are the field of view's horizontal and vertical cell widths respectively, r_i is the cell center's distance from the centroid location, u_i is the measured velocity of a cell, and U is the freestream velocity. It is important to specify that while the kinetic energy of the relative velocity is not equivalent to subtracting the freestream kinetic energy from the measured flow kinetic energy, the integration of both kinetic fields are equivalent. Both the relative and freestream velocities are obtained from a flow solution such as potential flow or PIV data. The volume is determined from the $\Delta x_i \Delta y_i \left(\pi r_i\right)$ term and is calculated similar to the drag force. It is revolved only 180º degrees about the centroid along the axis parallel to the freestream direction to preserve information on both sides of the bubble surface and retain as much of the bubble geometry as possible. The added mass in this form can be thought of as the summation of the flow domain's velocity-weighted mass based on the relative kinetic energy in the flow. Similar to the drag force calculation, the added mass calculation relies on an azimuthal symmetry about the bubble's centroid. After calculating the added mass, the virtual mass coefficient is determined by dividing the fluid mass displaced by the bubble as shown in eq. (47):

$$C_{VM} = \frac{m_a}{m_{disp}};\ m_{disp} = \frac{\pi}{6} \rho_f D_{eq}{}^3 \tag{47}$$

where ρ_f is the liquid density, and D_{eq} is the equivalent spherical bubble diameter. Equation (46) in conjunction with eq (47). was verified against Lamb's analytical $C_{VM} = 0.5$ value for potential flow around a sphere. The flow domain and spatial resolution was varied over a large range of both domain sizes and resolution to determine if the method converges on the analytical value regardless of how large the domain is. Figure 10 shows the calculated virtual mass coefficients converges to the predicted 0.5 value for various domain sizes and flow domain resolutions.

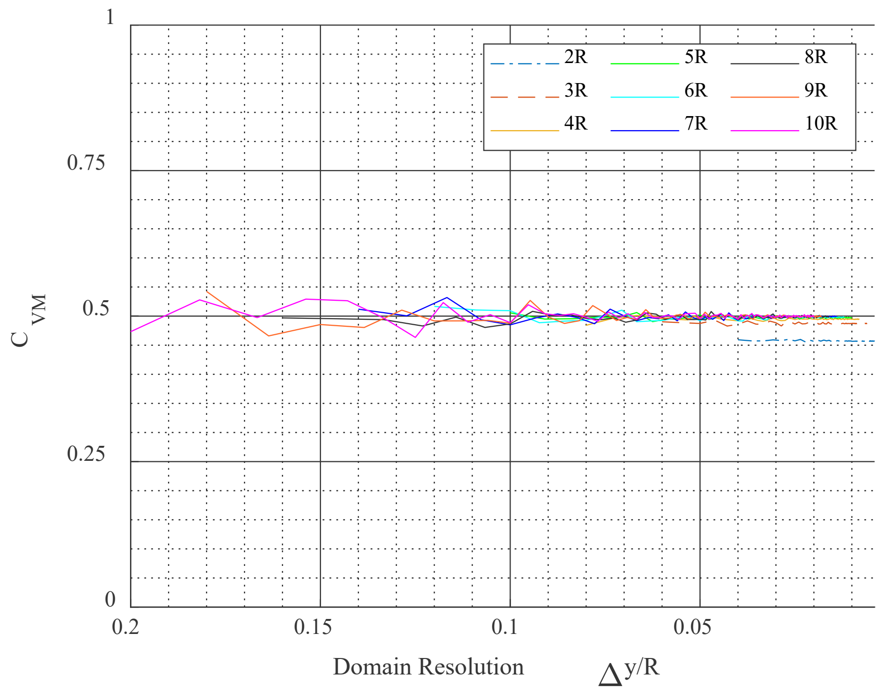

Figure 10: Predicted virtual mass coefficient for spherical potential flow

Each line plotted was for a particular square domain size of an integer multiplied by the sphere's radius (R). A square domain was used to make equal cell sizes in the x and y directions. The potential flow analysis identified a grid size spacing normalized by the object radius ratio of $\Delta y/R \leq 0.05$ is needed to have agreement with the analytical solution. It also showed that a domain size below four times the radius from the sphere's center was not large enough to calculate the analytical virtual mass coefficient as well as the remaining larger domain sizes did.

A similar analysis was performed on a half cylinder to confirm the two-dimensional case for an infinite cylinder. A distinct difference between the potential flow solution for virtual mass on a sphere and a cylinder is the reduction of the volume integral over the flow domain to a two-dimensional cross sectional area of the same flow domain. Figure 11 shows a kinetic energy per unit length spatial map for potential flow over a stationary cylinder with a uniform inlet velocity. The acceleration across the topside of the half cylinder is readily apparent and the stagnation point on the half cylinder's front and backside. The kinetic energy map provides a clear visualization of the kinetic energy influence from the stationary cylinder's presence in the flow field. The integrated kinetic energy difference between the potential flow and freestream flow without the cylinder when normalized by a reference kinetic energy quantifies the cylinder's virtual mass.

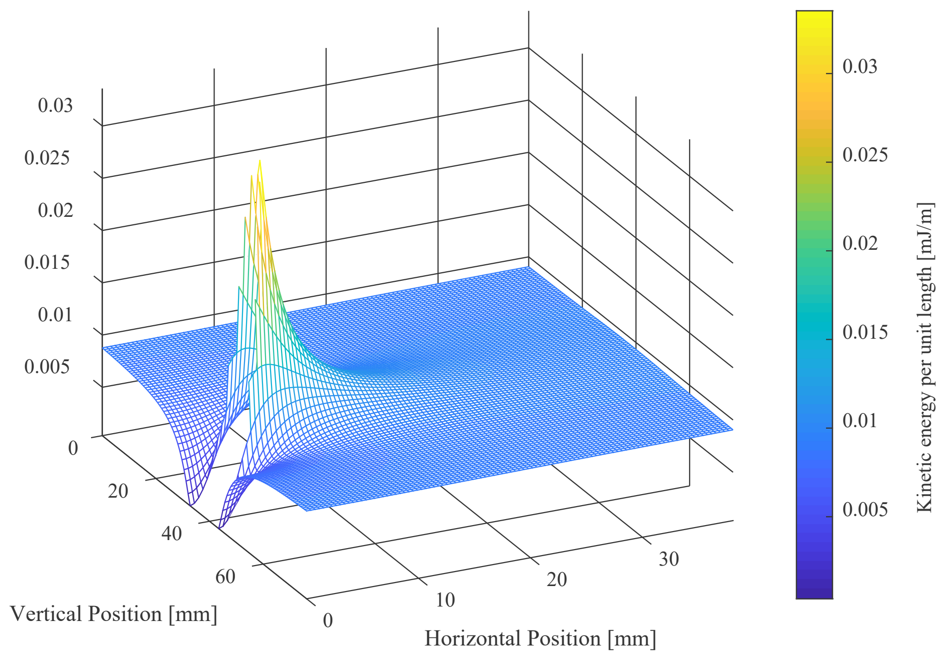

Figure 11: Infinite cylinder kinetic energy per unit length spatial map

Equation (48) shows this kinetic energy difference definition for the virtual mass:

$$C_{VM} = \frac{KE_f - KE_o}{KE_{\text{ref}}} \tag{48}$$

where KE_f is the flow domain's integrated kinetic energy, KE_o is the flow domain's kinetic energy without the object, and KE_{ref} is the reference kinetic energy such as the kinetic energy of the object moving with the freestream's velocity. In the case of a stationary flow field and a moving object, the flow domain kinetic energy term is zero. For the case of both a moving object and fluid, a relative velocity is used to make either the object or fluid stationary. Appendix B: Potential Flow Kinetic Energy Proof provides a proof showing that there is not a dependency on the reference frame used to evaluate the velocity in the flow's kinetic energy.

Because potential flow can leverage an analytical flow field, the kinetic energy difference in the freestream location is exactly zero. However, actual velocity data collected from PIV will have some amount of noise which prevents the kinetic energy difference in the freestream from ever reaching zero. To prevent this noise from artificially increasing the added mass in the flow domain, two modifications were made. The flow domain size integrated over can be varied by using integrating over a small layer surrounding the masked bubble. The added mass is then calculated using eq.(46) over the volume of the small layer. The size of the layer is then increased by the length of a single cell and the volume integration is repeated. This process continues until the added mass does not change by 10% between to two layers. The shape of the layer was determined to not influence the calculated added mass. The second modification was the use of a threshold for the squared velocity difference. If the difference between the measured fluid velocity squared in a cell was at least larger than 10% of the freestream speed squared the velocity, $\left(u_i^2 - U^2\right) \geq 0.1U^2$, the cell's kinetic energy would be considered in the added mass calculation, otherwise it would be assumed to have no kinetic energy contribution.

4.3 Sources of Error

Particle image velocimetry can provide a high-resolution quantitative velocity field with minimal intrusiveness. However, there are numerous factors that influence the accuracy in the calculation of the velocity vectors. Some contributions include the physical calibration length, camera optics, laser beam width, particle lag, and seeding density, however this list is not exhaustive. A source of error in planar PIV measurement comes from the out-of-plane motion that the flow has when capturing light intensity from the particles in the laser plane and the particles leave perpendicular to the laser plane. Because planar PIV cannot capture the third velocity component information, any region of flow that is highly three-dimensional, such as the wake behind the bubble, there is an expected decrease in reporting accepted velocity vectors from the DynamicStudio software.

A large source of uncertainty comes from the correlation method used to determine the velocity vectors. One approach involves quantifying the true pixel displacement uncertainty using information from the cross-correlation plane, where the error is related to the ratio of the largest detectable correlation peak to the second highest peak [44]. Other work has involved generating a four-dimensional uncertainty response, also referred to as an "uncertainty surface", which is dependent on the particle displacement, particle image diameter, particle image density, and shear [45]. The correlation algorithm's response is recorded for each of these four parameters and used to generate the uncertainty surface. The uncertainty for the reported velocity vector is obtained by inputting the four known parameters into the uncertainty surface to have the velocity's uncertainty calculated. Currently, there is no accepted best practice for quantifying the uncertainty resulting from a correlation method and is an active research area. A method proposed by Jackson [46] provides a simple uncertainty analysis framework that considers the physical spatial calibration length, pixel uncertainty, and timing uncertainty based on the laser/camera synchronization. This uncertainty analysis by Jackson is ideal when using commercial PIV software that does not provide the user with information related to the correlation method needed for the signal to noise ratio or uncertainty surface methods. For this reason, the method used by Jackson was implemented to determine the measured velocity field's uncertainty.

4.4 Uncertainty Analysis

Uncertainty was propagated using the Kline McClintock method show in eq. (33). For the measured velocity field, this study considered the physical calibration length resolution, image plane calibration length, and timer box resolution for the sources of error in velocity. A velocity vector is calculated based on the general equation, eq. (49), shown by Jackson [46]:

$$\mathrm{v} = \frac{\Delta x_{pix}}{\Delta t}\psi \; ; \; \psi = \frac{l}{L} \tag{49}$$

where Δx_{pix} is the pixel displacement, Δt is the time between image pairs, ψ is the pixel-spatial scale factor determined by the spatial calibration, l is the physical calibration object length [mm], and L is the calibration object's length in number of pixels. The pixel displacement is determined by the DynamicStudio software, and the time between image pairs is controlled by user input. Applying the three velocity uncertainty sources mentioned previously and eq. (49) into the Kline-McClintock method results in eq. (50) where it can be noted that actual pixel displacement does not need to be used directly to determine the velocity uncertainty and relies on the reported velocity from the correlation method.

$$\sigma_{\mathrm{v}} = \left[\left(-\frac{\mathrm{v}}{L}\sigma_L\right)^2 + \left(\frac{\mathrm{v}}{l}\sigma_l\right)^2 + \left(-\frac{\mathrm{v}}{\Delta t}\sigma_{\Delta t}\right)^2\right]^{0.5} \tag{50}$$

The cross-sectional area uncertainty was propagated from the injected volume uncertainty which affects the spherical equivalent diameter used in the area. Tate's law, eq. (34), was used for bubbles smaller than 0.1 mL injected volume to determine the minimum injectable bubble diameter and used a separate uncertainty propagation to consider the injection system's tube diameter. The full uncertainty propagation derivations are provided in Appendix A. The drag coefficient uncertainty was performed by propagating the drag force, velocity, and reference area. The uncertainty contribution was not performed for the pressure when determining the form drag force because of the nature of determining the uncertainty of the pressure field calculations. Applying the Kline McClintock method to the form drag force requires propagating the velocity uncertainty through the queen2 algorithm, which integrates the pressure gradient along eight different tracks to the cell of interest in the field of view. The queen2 algorithm is not able to report which integration tracks were used in the median polling, and to remain conservative the longest track length would be assumed to be used for average of the median polling which would be integrating diagonally across the discretized flow domain. However, conservatively propagating uncertainty through the numerical integration of eq. (42) results in pressure uncertainties on the same order of magnitude as the calculated relative pressures and shows that the numerical integration compounds uncertainty results in large uncertainty contribution from the pressure algorithm. Because the accuracy of the algorithm has already been demonstrated in other studies [41], [42], the pressure uncertainty was neglected from the analysis. This reduces the drag coefficient uncertainty to eq. (51):

$$\sigma_{C_D} = \left[\left(\frac{\partial C_D}{\partial F_D}\sigma_{F_D}\right)^2 + \left(\frac{\partial C_D}{\partial \mathrm{v}_r}\sigma_{\mathrm{v}_r}\right)^2 + \left(\frac{\partial C_D}{\partial A}\sigma_A\right)^2\right]^{0.5} \tag{51}$$

$$\frac{\partial C_D}{\partial F_D} = \frac{2}{\rho_f A \mathrm{v}_r{}^2} \tag{52}$$

$$\frac{\partial C_D}{\partial \mathrm{v}_r} = \frac{-4F_D}{\rho_f A \mathrm{v}_r{}^3} \tag{53}$$

$$\frac{\partial C_D}{\partial A} = \frac{-2F_D}{\rho_f A^2 \mathrm{v}_r{}^2} \tag{54}$$

where F_D is the calculated drag force, ρ_f is the liquid density, A is the equivalent spherical bubble diameter, and v_r is the relative bubble velocity. The virtual mass coefficient uncertainty is found from eq. (55)-(57)

$$\sigma_{C_{VM}} = \left[\left(\frac{\partial C_{VM}}{\partial m_a} \sigma_{m_a} \right)^2 + \left(\frac{\partial C_{VM}}{\partial m_{disp}} \sigma_{m_{disp}} \right)^2 \right]^{0.5} \tag{55}$$

$$\frac{\partial C_{VM}}{\partial m_a} = \frac{1}{m_{disp}} \tag{56}$$

$$\frac{\partial C_{VM}}{\partial m_{disp}} = -\frac{m_a}{m_{disp}{}^2} \tag{57}$$

Because the virtual mass coefficient is based only on the measured velocity field, the uncertainty propagation does not encounter issues such as the pressure uncertainty.

5 RESULTS & DISCUSSION

A total of 11 bubble sizes were injected with an equivalent spherical bubble diameter ranging from $2.94\text{ mm} < D_{eq} < 20\text{ mm}$ with total drag, form drag, and virtual mass coefficients calculated with an uncertainty propagation analysis performed. Bubble sizes below 0.1 mL volume had 6 repeated trials to allow consideration of the random uncertainty. Bubble volumes greater than or equal to 0.1 mL only used one trial since these bubbles are larger than ellipsoidal range and occupy the beginning of the spherical cap regime and were largely used to confirm an expected drag coefficient value of 2.33. Table 6 shows the injected bubble volumes, diameter, and equation used to determine equivalent diameter in this study:

Table 6: Bubble Test Matrix

Volume [mL]	Diameter [mm]	Trials
0.013±0.004	2.94±0.26	6
0.027±0.007	3.70±0.33	6
0.04±0.011	4.24±0.38	6
0.053±0.014	4.67±0.42	6
0.067±0.018	5.02±0.45	6
0.1±0.003	5.76±0.05	1
0.8±0.05	11.52±0.24	1
1.25±0.05	13.37±0.18	1
2.0±0.05	15.63±0.13	1
2.5±0.05	16.84±0.11	1
4.0±0.05	19.69±0.08	1

For bubble volumes below $\forall < 0.1\text{mL}$, Tate's Law, eq (34), was used to estimate the minimum bubble diameter that could be injected using Setup #1 as listed in Table 5. The minimum bubble diameter $D_{eq} = 2.94\text{mm}$ resulted in a minimum 0.013 mL injectable volume. The volumes 0.027-0.067 mL were achieved by injecting one of the minimum bubble sizes at a time to reach the desired volume. Volumes larger than $\forall \geq 0.1\mathrm{mL}$ relied on the known injected air volume from the syringe and did not rely on the minimum injectable bubble size. Additionally, each of the injected bubbles coalesced into the total single bubble volume prior to its release into the flow field.

Because spheroidal and ellipsoidal bubbles rise in a helical or zig-zag motion, the bubble would not remain centered in the laser plane for the entire collection time. Trials where the bubble remained in the laser plane for at least more than 10 consecutive frames and at least two occurrences would be analyzed. Because of the quasi-steady state assumption used for the buoyancy and drag force, each frame provides an instantaneous measurement of the drag force which is averaged across the other measured values and made the segmented analysis sequences of a trial acceptable.

Figure 12-Figure 16 shows bubbles, ranging from spheroidal to ellipsoidal, rising through the field of view. Bubble volumes of 0.013 mL and 0.027 mL (Figure 12, Figure 13) exhibit spheroidal geometry and have a helical rise path. As a result, trials for these bubble sizes needed to be analyzed in sections where the bubble remained within the laser plane. Because of the counter-current flow, the tightness of the spiral was reduced which allowed more direct vertical zig-zag motion thereby increasing the number of frames with the bubble moving upwards through the laser plane. Bubbles from 0.04 mL to 0.067 mL exhibited ellipsoidal geometry with zig-zag rise paths which reduced the amount of out-of-plane motion. The 0.067 mL bubbles also began to experience some distorted bubble behavior with the bubble aspect ratio between the height and width fluctuating throughout the rise. This is specifically seen in Figure 16 at time steps t=1.770s and 1.8s where the bubble expands from an ellipsoidal shape to a more spheroidal shape before reverting to its ellipsoidal shape. Bubble sizes ranging from 0.1 mL to 4.0 mL transitioned to distorted and eventual spherical-cap bubbles with rectilinear rise paths as expected. All injected bubbles were accompanied with vortex shedding.

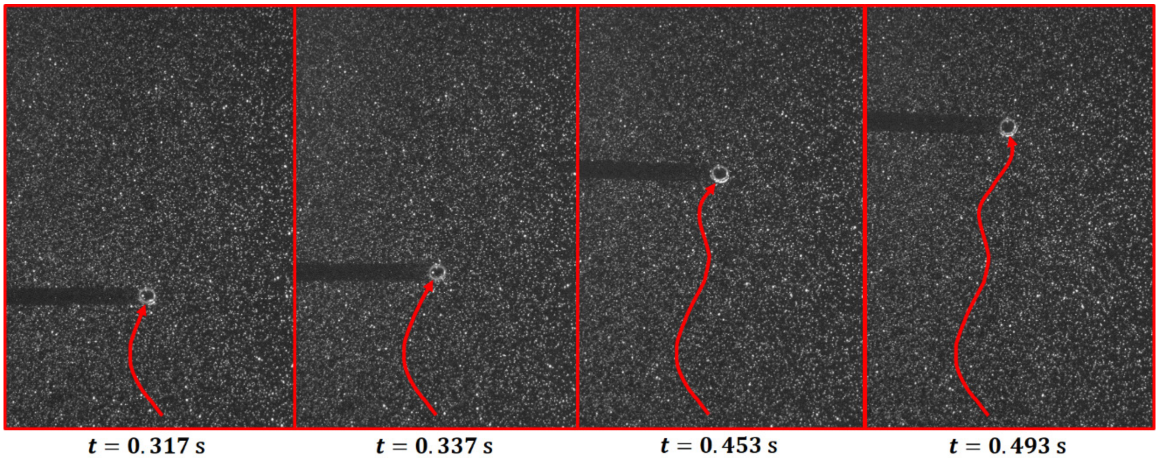

Figure 12: 0.013 mL bubble rising

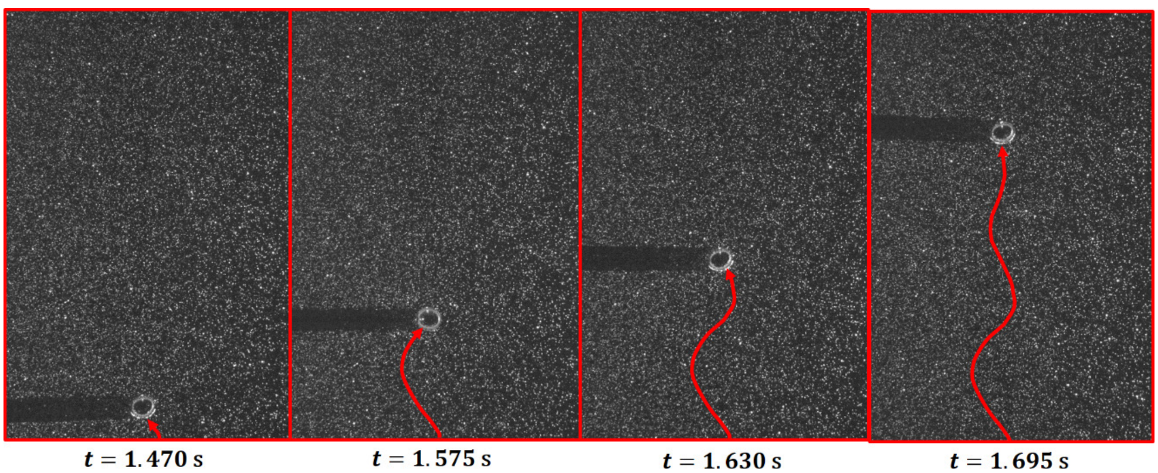

Figure 13: 0.027 mL bubble rising

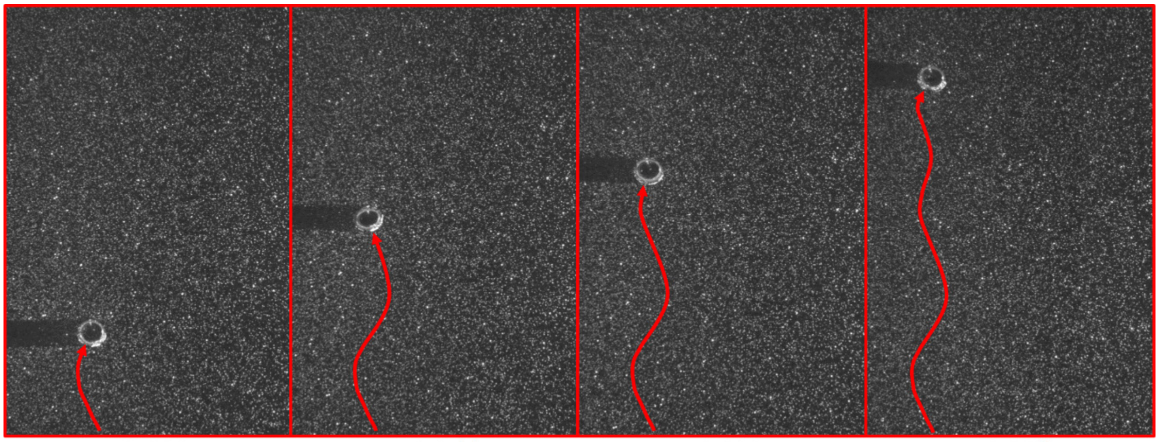

$t = 0.930$ s $t = 1.055$ s $t = 1.100$ s $t = 1.265$ s

Figure 14: 0.04 mL bubble rising

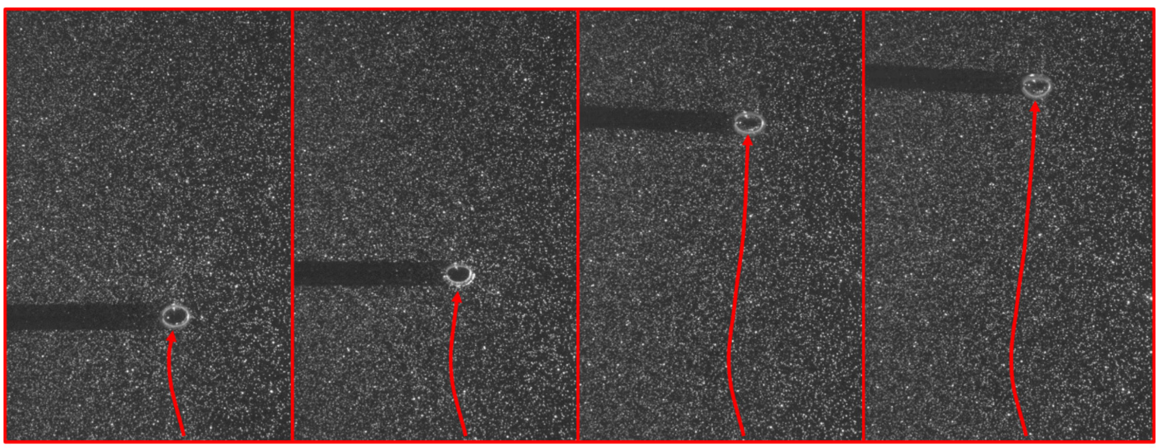

$t = 1.590$ s $t = 1.630$ s $t = 1.790$ s $t = 1.820$ s

Figure 15: 0.053 mL bubble rising

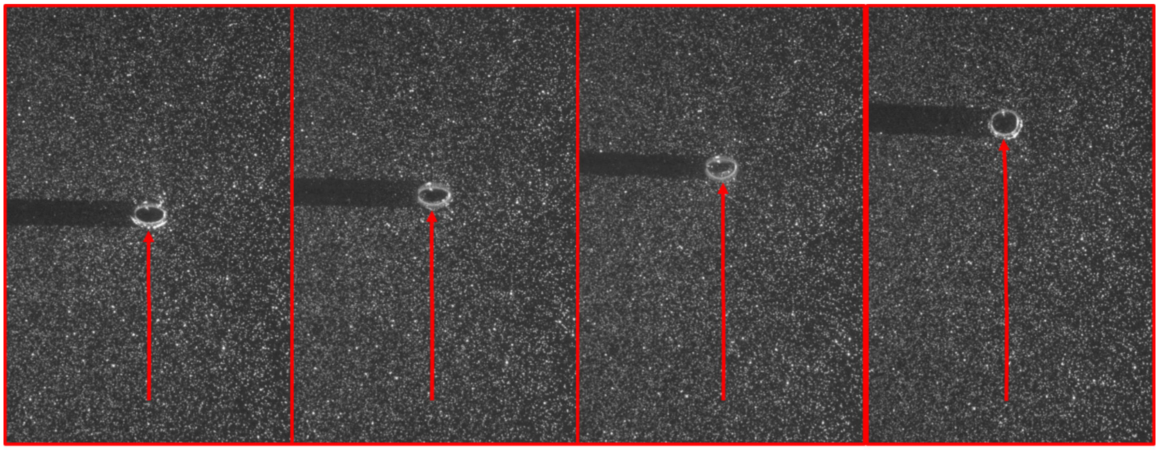

Figure 16: 0.067 mL bubble rising

The vortex shedding is visible when looking at the velocity field, velocity and pressure contour maps. Figure 17 shows the PIV velocity field obtained for the smallest bubble size where the blank white region represents the masked bubble, note that the axis are zoomed in but retain original aspect ratio from the field of view. The vertical and horizontal velocity components are shown in Figure 18 and Figure 19 respectively. The bubble speed is indicated by the high positive values directly behind the bubble, additionally a stagnation point can be seen in front of the bubble which aligns as expected since the counter-current flow would slow to zero slightly above the bubble's surface. A shed vortex is visible about two bubble diameters behind along with the bubble's wake from the rise. The horizontal components behind the bubble extend away from the wake centerline indicating the recirculation zone which is further visible from Figure 20 with the countering acting vorticity in the wake. Additionally, it is noted that while there is counter-clock wise direction vorticity on the bubble's left hand side and clock wise vorticity on the right hand side, there exists vorticity directly at the bubble left and right edge respective opposite sign as well as through the near bubble wake. This structure becomes less defined around four bubble diameters away from the bubble and indicates the far wake region.

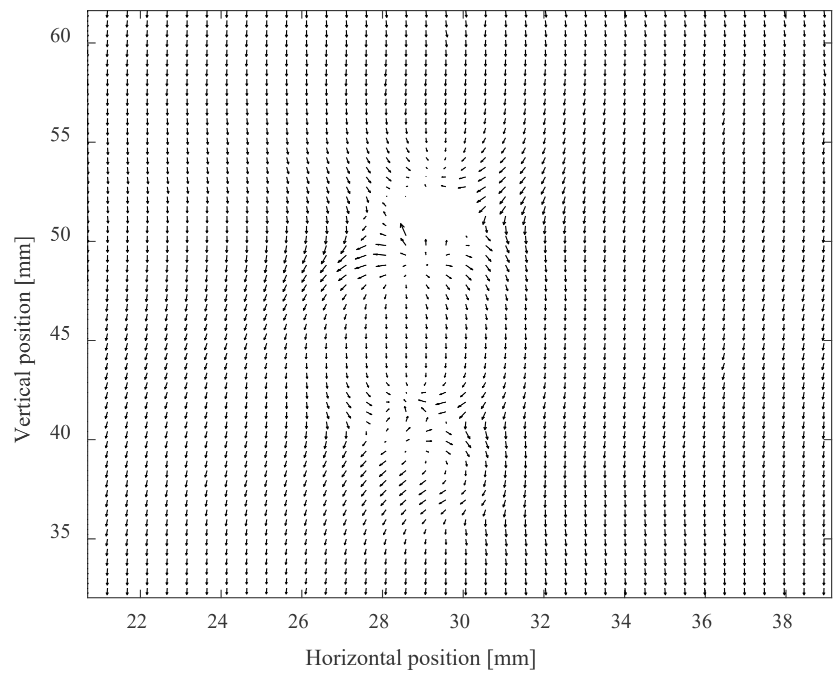

Figure 17: 0.013 mL bubble velocity field | t=0.453 s

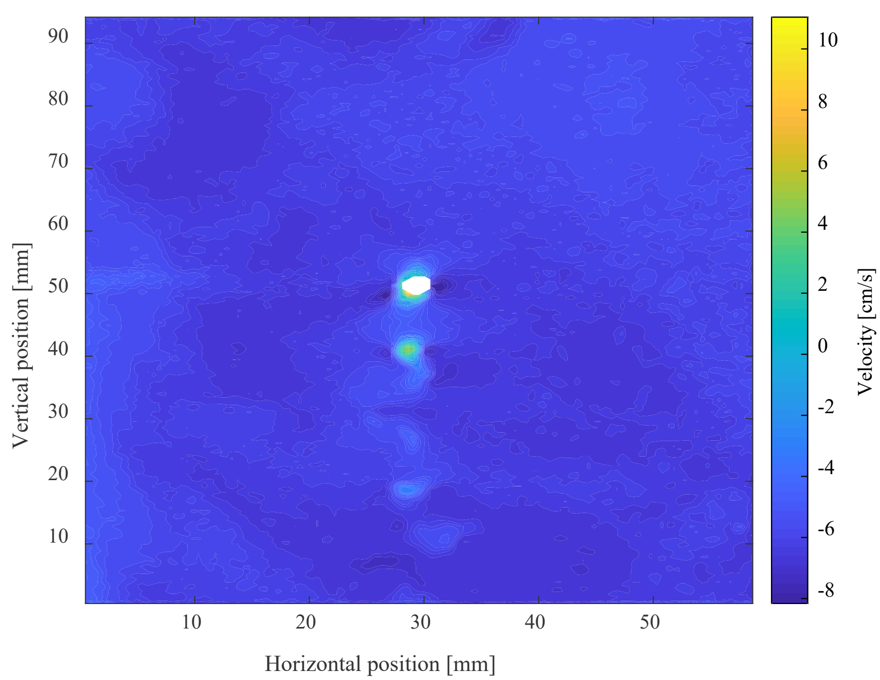

Figure 18: 0.013 mL bubble vertical velocity field | t =0.453 s

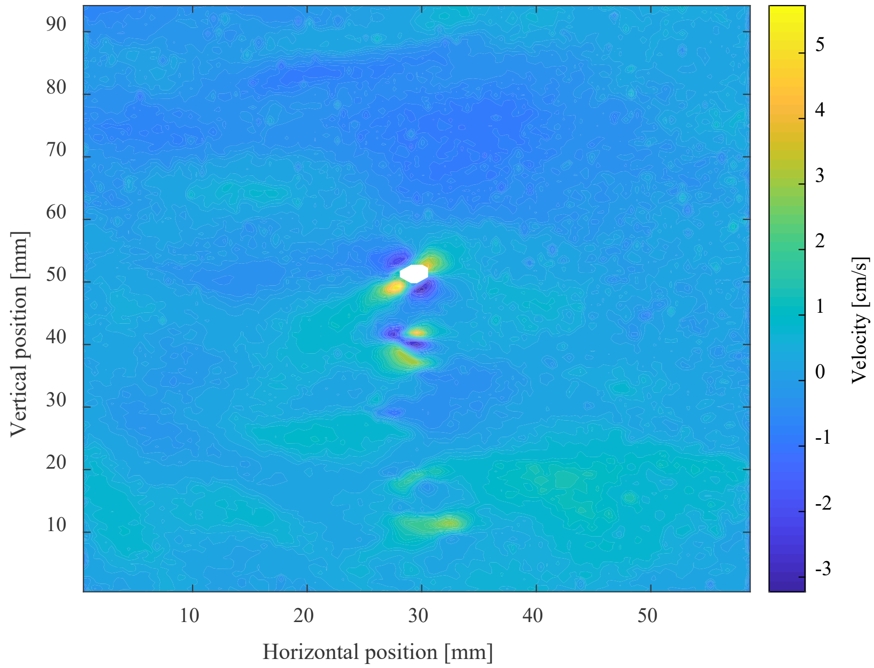

Figure 19: 0.013 mL bubble horizontal velocity field | t=0.453 s

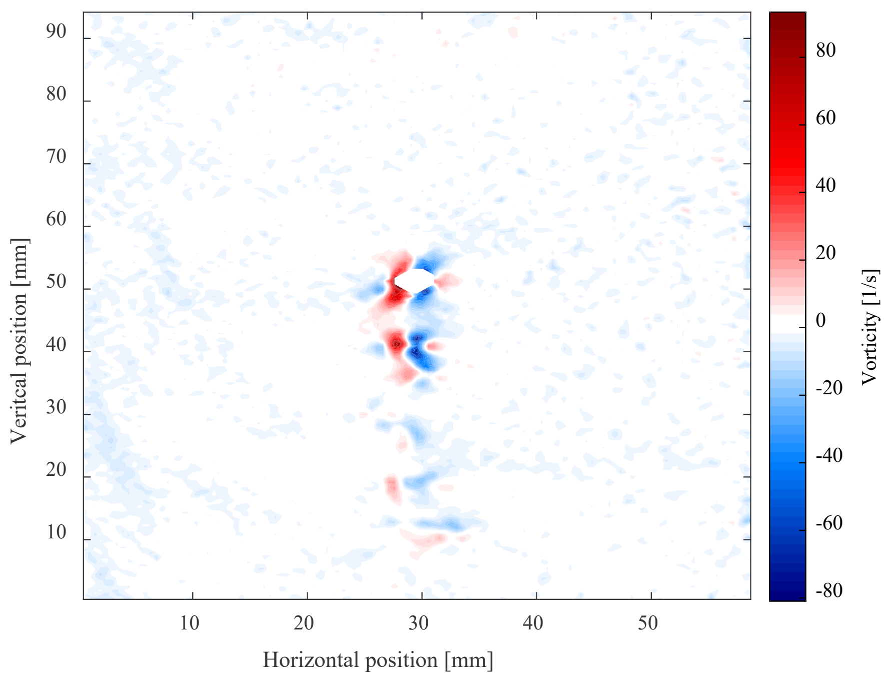

Figure 20: 0.013 mL bubble vorticity map | t=0.453 s

When looking at the largest ellipsoidal bubble size (0.067 mL), the bubble exhibits more zig-zagging rise path and has stronger wake dynamics than compared to the 0.013 mL bubble. Figure 21 shows the PIV velocity field obtained for a 0.067 mL bubble with zoomed axis and preserved aspect ratio. The larger bubble size shows a much stronger recirculation zone directly behind the bubble when compared to the 0.013 mL bubble in Figure 17. As with the other bubble cases, vortex shedding is observed occurring with about one bubble diameter spacing as seen in Figure 22. The vortex has a much larger size and velocity. The horizontal velocity component directions in Figure 23 retain the same pattern as before with the diagonal symmetry repeating in the far wake region. Looking at Figure 24, the vorticity does not keep its structure past the immediate recirculation zone behind the bubble. While the vorticity in the 0.013 mL bubble case has a largely continuous vorticity in the wake, the 0.067 mL case has distinct clusters of vorticity in the wake accompanying each prior vortex. This is consistent with the primary helical vortex wake and secondary wake formation seen in bubble wake dynamics [47] where the primary wake is characterized by vortex zone which has asymmetrical vortex shedding forming the secondary wake with shed vortices decaying from viscous stresses.

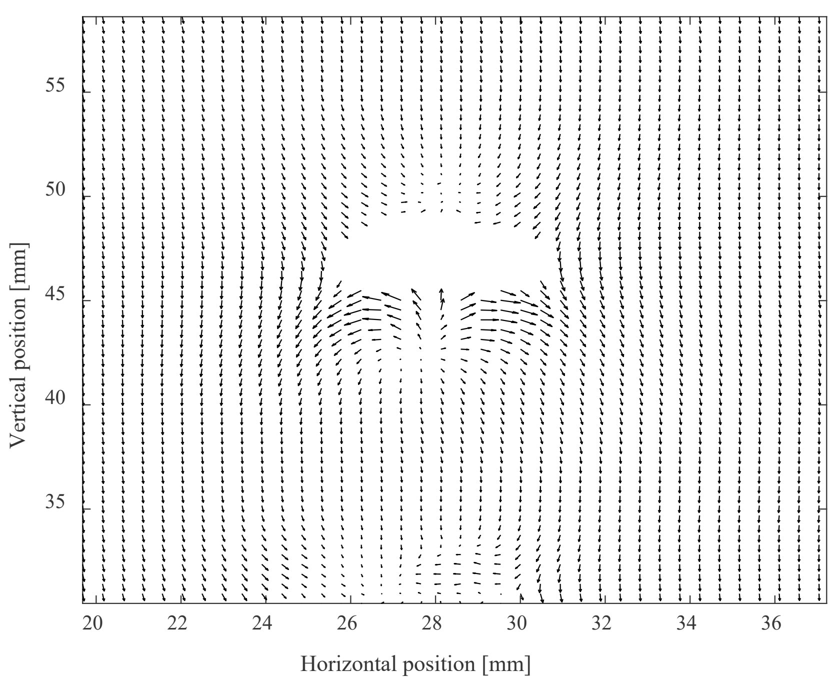

Figure 21: 0.067 mL bubble velocity field | t=1.740 s

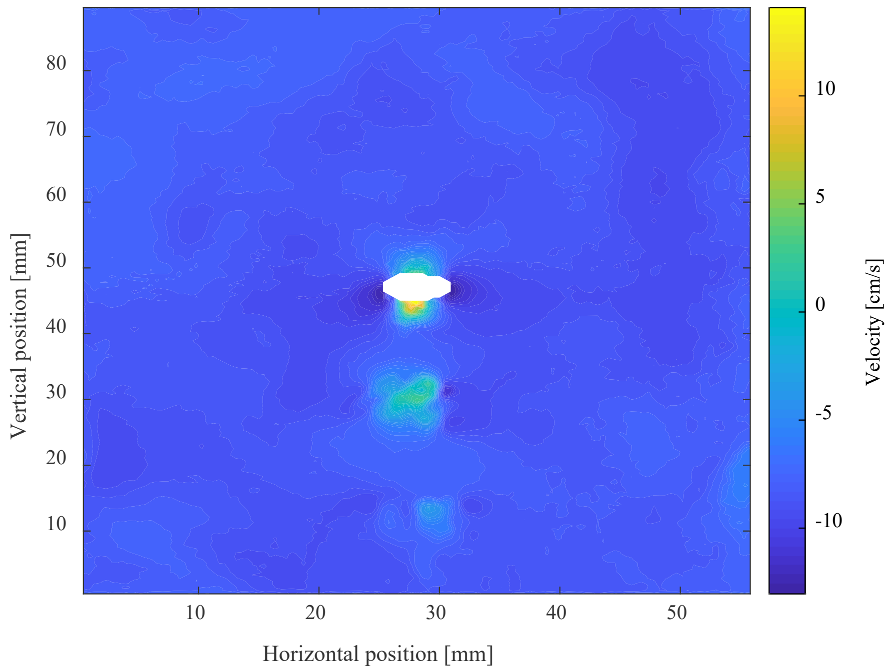

Figure 22: 0.067 mL bubble vertical velocity field | t=1.740 s

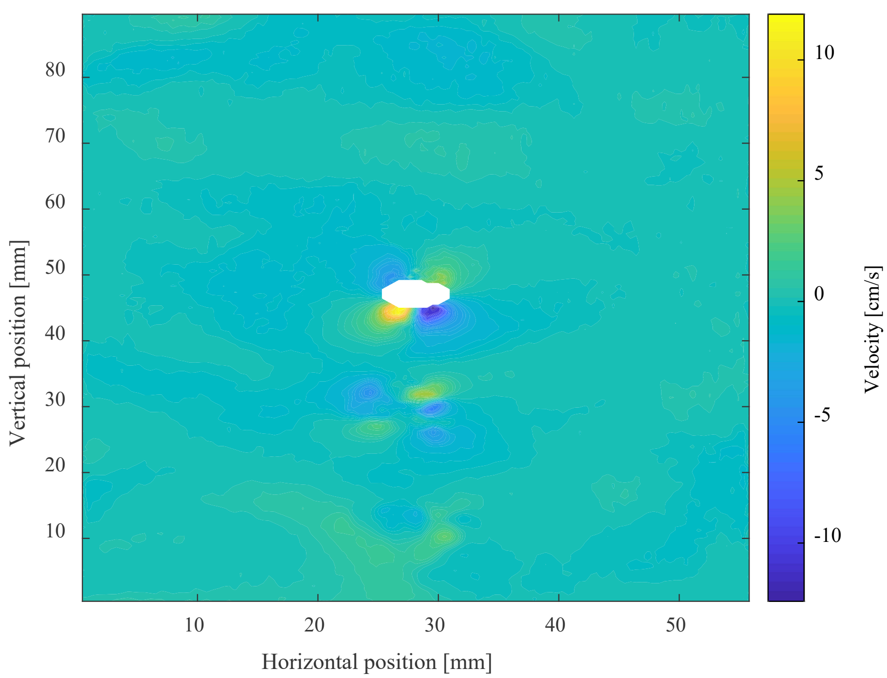

Figure 23: 0.067 mL bubble horizontal velocity field | t=1.740 s

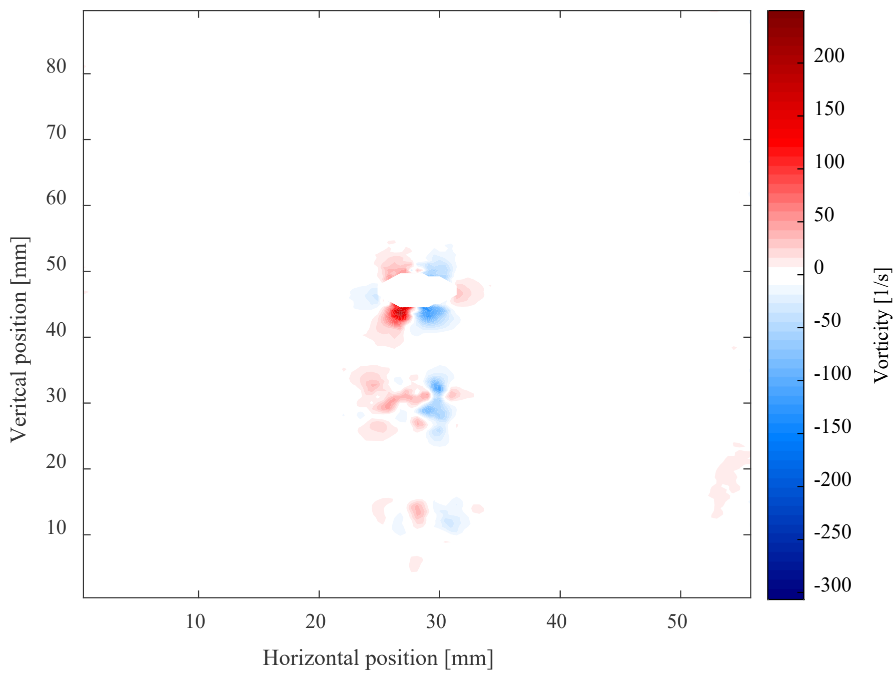

Figure 24: 0.067 mL bubble vorticity map | t=1.740 s

The terminal velocity, reported in Figure 25, shows a good agreement between the predictions, but with consistently lower values which would suggest that the drag coefficient would have be larger than predicted. Uncertainty on the bubble terminal velocity increases with bubble size which results from the timing uncertainty associated with tracking the bubble centroid. Because all bubble sizes were captured using a 200 Hz frequency between image-pairs, it is expected that the greater distance travelled with the same timing resolution would begin to limit the accuracy of the velocity measurement. However, the maximum terminal velocity uncertainty with 95% confidence is 2.34% of the measured value and is considered acceptable.

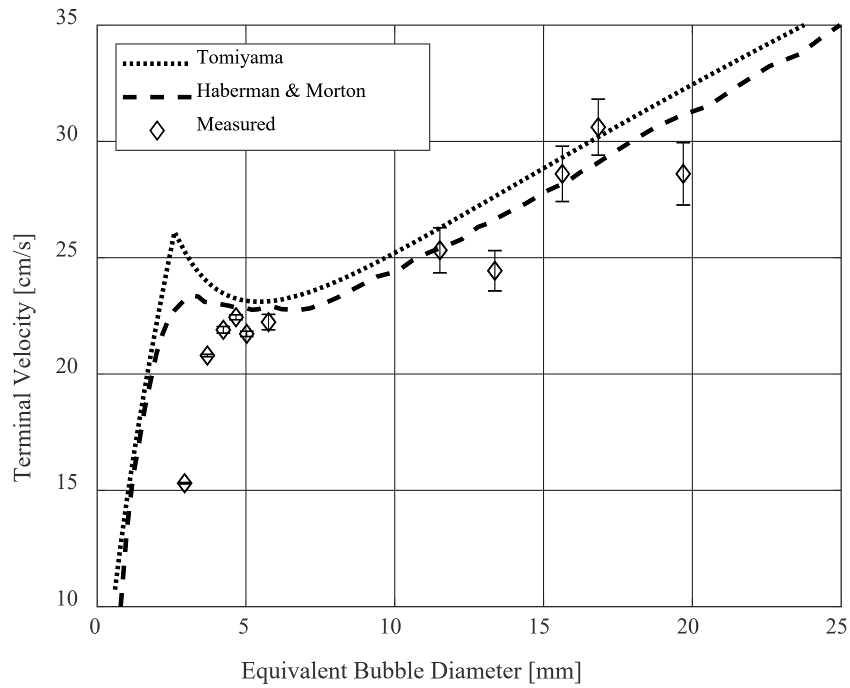

Figure 25: Bubble terminal velocity versus spherical equivalent bubble diameter

5.1 Drag Coefficient

The total and form drag coefficient for each bubble trial were time averaged with measurement and random uncertainty propagated, with the 6 trials averaged again with uncertainty propagated to determine the representative drag coefficient for that bubble size. Figure 26 overlays the averaged total drag coefficient on a log scale plot against the Reynolds number using the equivalent spherical diameter and the averaged measured terminal velocity. The dashed line is based on experimental data collected by Haberman and Morton [4] in tap water at 21ºC. The dotted line shows the predicted values from eq.(18), developed by Tomiyama et. al. [10] for heavily surface contaminated fluid which was considered appropriate due to the tracer particle presence in the flow field.

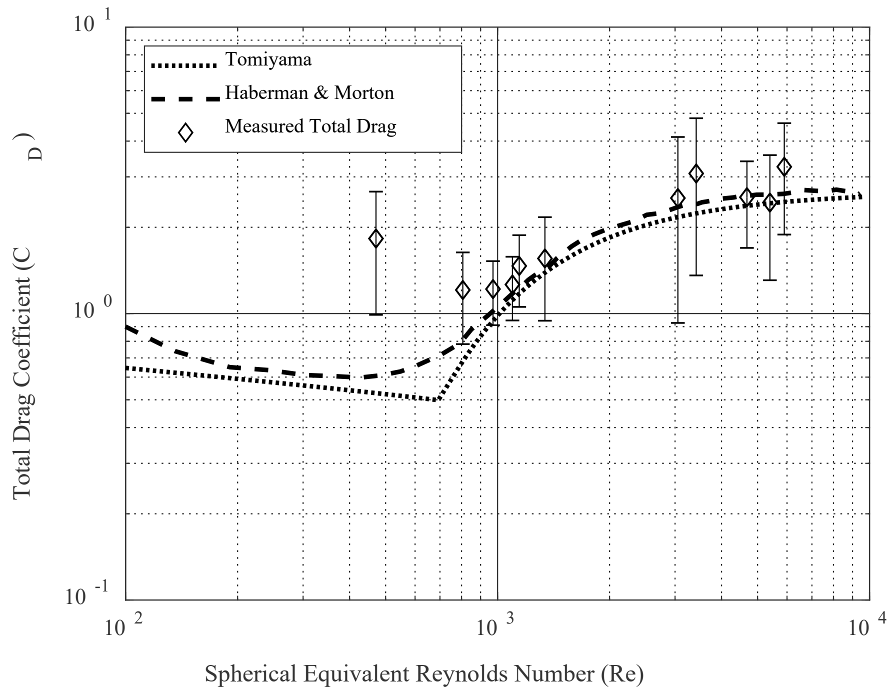

Figure 26: Measured total drag coefficient versus Reynolds Number

The total drag coefficient observed trend is consistent with the trends shown from the other data and correlation. The total drag coefficient value plateaus in the spherical cap regime as expected and agrees with the previous work. Additionally, the transition from spheroidal to ellipsoidal/distorted occurs near Reynolds number of $\mathrm{Re} = 10^3$ which is accompanied by a decrease in drag coefficient which agrees well with past work. It can be noted that the collected data has larger values than the prior work below this Reynolds number range. A possible explanation is the high concentration of tracer particles in the fluid which increases surface contamination. The higher concentration of contamination has been correlated to higher surface tension values [6] which results in the bubble surface behaving more akin to a rigid particle with a non-uniform surface which increases drag force experienced by the particle.

Figure 27 shows a direct comparison between the calculated drag coefficients and Tomiyama's predicted values from Figure 26 with 10% deviation lines from a 1:1 agreement included.

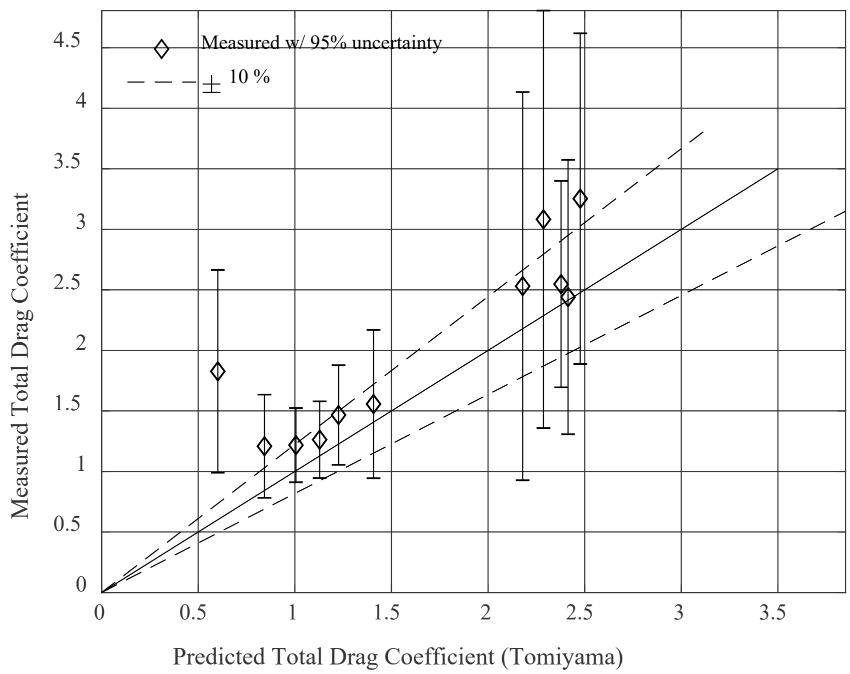

Figure 27: Measured total drag coefficient versus prediction

It is seen that except for four cases, there was agreement within 10% of each other considering the 95% confidence intervals of the calculated values. Looking at the nominal values, the correlation from Tomiyama consistently under predicted the drag coefficient.

Table 7: Total Drag Coefficient Values with 95% confidence

Bubble Volume	**Re**	$C_{D,t}$	**Measurement Uncertainty**	**Random Uncertainty**	**Total Uncertainty**
0.013 mL	471±82	1.827	0.419	0.725	0.838
0.027 mL	806±140	1.209	0.220	0.365	0.426
0.04 mL	972±169	1.217	0.226	0.208	0.307
0.053 mL	1096±190	1.263	0.178	0.261	0.316
0.067 mL	1143±199	1.466	0.238	0.336	0.411
0.1 mL	1341±29	1.557	0.286	0.542	0.613
0.8 mL	3053±169	2.531	0.093	1.601	1.603
1.25 mL	3420±148	3.083	0.061	1.723	1.724
2.0 mL	4681±205	2.547	0.054	0.851	0.853
2.5 mL	5397±219	2.440	0.050	1.132	1.133
4.0 mL	5899±274	3.253	0.043	1.365	1.366

The form drag coefficient was similarly time averaged with uncertainty propagated and is shown on a log scale against Reynolds number in Figure 28. The data is overlaid with the predicted total drag coefficient from Figure 26 to display the form drag contribution.

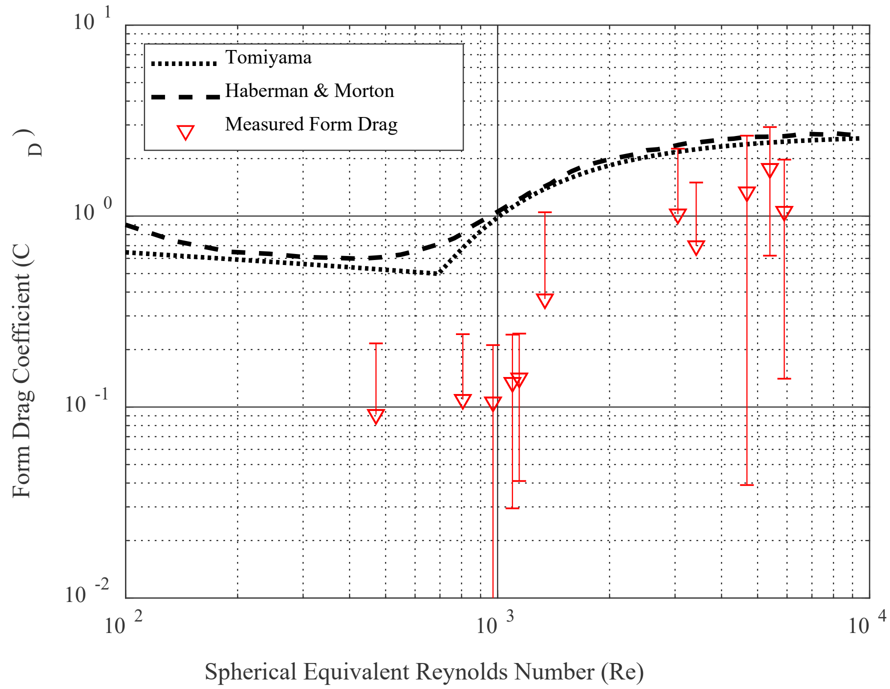

Figure 28: Form drag coefficient versus Reynolds number

The figure shows a nominal trend of increasing form drag with increasing Reynolds number. This agrees with the qualitative discussion of form drag having greater contribution with increasing bubble size. The form drag is expected to become dominate at very high Reynolds number because the boundary layer separation point moves from the backside of the bubble towards the front which increases the pressure drop from the flow separation thereby increasing the form drag force.

The ellipsoidal bubbles have a non-negligible skin drag contribution which is visible by the smaller pressure difference across the spheroidal and ellipsoidal bubbles and less turbulent wakes as seen in Figure 20. Figure 29 shows the calculated skin drag from subtracting the form drag coefficient from the total drag. In the case of the spheroidal and ellipsoidal bubbles ($\mathrm{Re} < 2\times10^3$) the skin drag dominates as expected. However, while the form drag increases towards the total drag coefficient value with increasing bubble size it is not the dominate drag component and the skin drag has a roughly equal contribution. It would be expected that as the cap bubble size further increases the form drag will continue to increase and thereby become more dominant than the skin drag force.

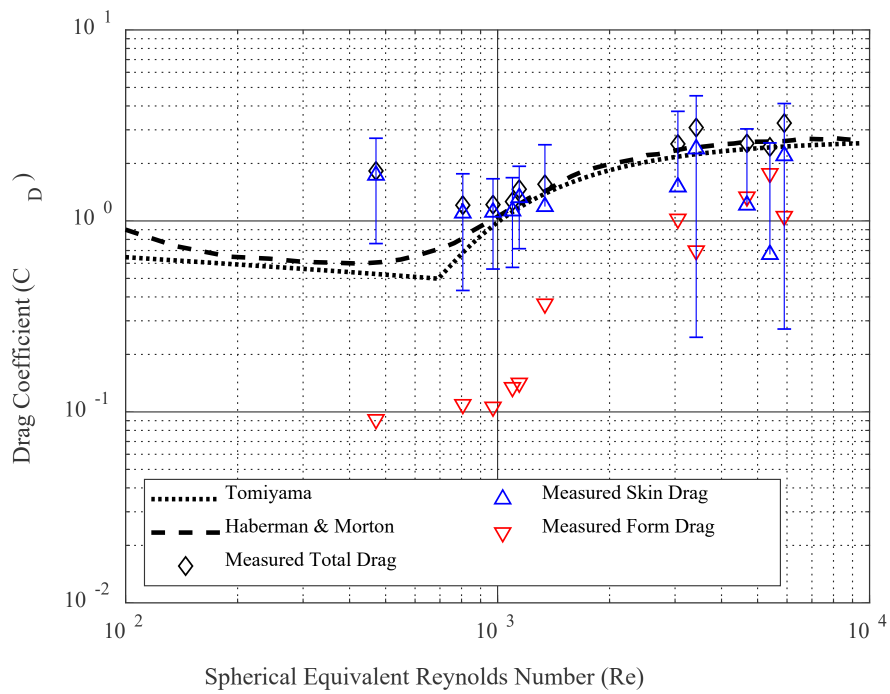

Figure 29: Measured skin drag versus Reynolds number

While the nominal trend agrees well for form drag, the uncertainty propagated across all cases is very large. One of the biggest contributors is the limited spatial resolution available for the smallest three bubble sizes. Because of the available camera lenses and limited extension rings, the resolution was limited to a horizontal and vertical grid size of 0.469 mm x 0.469 mm. Inspection of the uncertainty revealed the random uncertainty as the largest contributor as shown in Table 8. The large spread in the instantaneous form drag coefficient in each trial was found to come from the calculated form drag which in turn depends on the pressure integration along the bubble surface. The pressure integration is sensitive to the spatial resolution since it provides the number of cells used in the line integral prior to the surface revolution to complete the volume integral. Additionally, the masking can compound on this sensitivity since it provides the number of cells along the bubble interface. The increasing bubble size corresponded with continually decreasing measurement uncertainty relative to the calculated value which highlights the importance of improved spatial resolution. However, because only one trial was used for the bubble sizes of $\forall \geq 0.1[\text{mL}]$ the random uncertainty from the spread of calculated drag coefficient values at each recorded time frame explains the very large standard deviation from the time averaged value.

Table 8: Form Drag Coefficient Values with 95% confidence

Bubble Volume	Re	$C_{D,f}$	Measurement Uncertainty	Random Uncertainty	Total Uncertainty
0.013 mL	471±82	0.091	±0.058	±0.110	±0.124
0.027 mL	806±140	0.110	±0.064	±0.115	±0.131
0.04 mL	972±169	0.106	±0.059	±0.087	±0.105
0.053 mL	1096±190	0.134	±0.056	±0.089	±0.105
0.067 mL	1143±199	0.142	±0.071	±0.071	±0.101
0.1 mL	1341±29	0.368	±0.080	±0.675	±0.679
0.8 mL	3053±169	1.024	±0.038	±1.229	±1.230
1.25 mL	3420±148	0.698	±0.016	±0.800	±0.800
2.0 mL	4681±205	1.338	±0.025	±1.298	±1.338
2.5 mL	5397±219	1.773	±0.030	±1.152	±1.152
4.0 mL	5899±274	1.058	±0.011	±0.917	±0.917

5.2 Virtual Mass Coefficient

The method for calculating virtual mass coefficient was initially performed on with a stationary cylinder rod representing an infinite cylinder case in the flow channel described in Section 3.1. Varying inlet velocities of 120, 150, 210, and 270 mm/s were used to collect PIV data over a range of Reynolds numbers as listed in Table 9. The velocity field was processed to obtain the pressure field to be integrated across the cylinder surface to calculate the form drag. Because the cylinder produced a distinct shadow region on the cylinder's backside, only the front half of the field of view was analyzed.

Table 9: Cylinder rod flow conditions

Re	Measurement Uncertainty	Random Uncertainty	Total Uncertainty ($\sigma_{95\%}$)
1059	±0.86	±57	±58
1530	±1.18	±99	±99
1992	±1.15	±132	±132
2438	±1.80	±125	±125
2603	±1.98	±174	±174

A benefit to using a static cylinder was the two-dimensional flow assumption used to treat the planar wake. Figure 30 shows a spatial map of the turbulent integral time scale calculated for the cylinder data with a 210 mm/s inlet velocity. This was performed for the other four data sets were the maximum integral time scale was selected to compare to the total collection time. All five data sets were collected over a 2.135 s time frame which ensured the measurement period sufficiently captured the integral time scales for each flow speed. The integral time scales for 120, 150, 210, 250, and 270 mm/s flows were 13.8, 14.7, 10.9, 15.4, and 10.8 ms, respectively. The integral time scale distribution shows the largest time scales within the free shear layer of the turbulent wake. This positioning is reasonable since it describes the characteristic time scale that bulk eddy movements occur at. The macroscopic portion of the wake resides near the wake boundary with the freestream and is associated with the production of turbulent kinetic energy supplied to the microscale features of the turbulence. The presence of these microscale eddies is evident in the minimum time scale portion in the wake interior and is characterized by increased mixing.

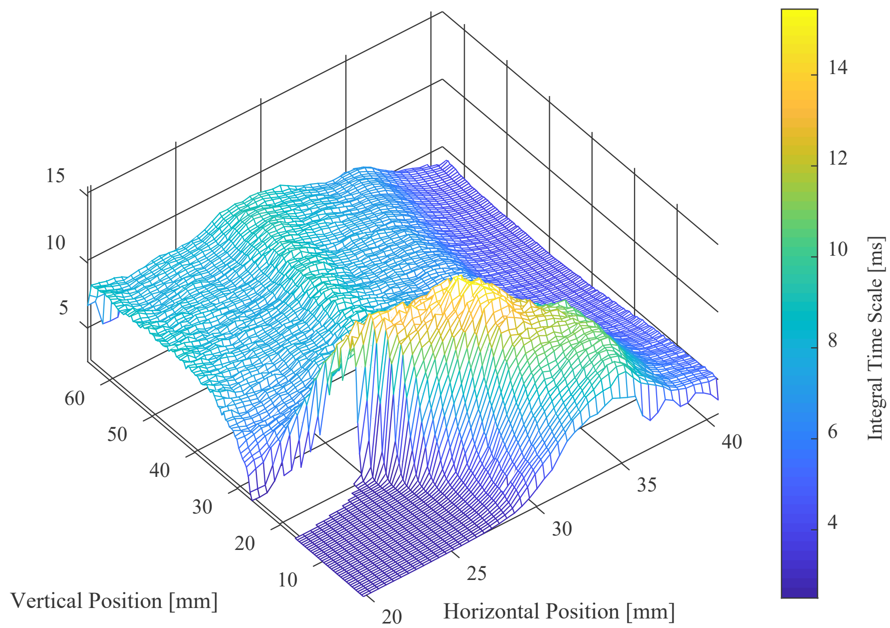

Figure 30: Cylinder 250 mm/s integral time scale spatial map

Figure 31-Figure 35 display the turbulent kinetic energy for each flow condition with a consistent colorbar scale for more direct comparison. As expected, the increase in Reynolds number results in increase in the turbulent kinetic energy and the growth of the free shear layer on the cylinder backside which agrees with past studies of flow past a cylinder [47]. The turbulent kinetic energy is largely confined to the wake boundary and corresponds to the large bulk eddies losing kinetic energy to supply the microscale eddies performing most of the mixing within the wake structure. A source of the turbulent kinetic energy is visible on the cylinder surface and indicates the vorticity generation along the surface which is supplied to the primary wake region visible by the lower portion of turbulent kinetic energy directly behind the cylinder. The increasing Reynolds number and further definition of the wake boundary visualizes the kinetic energy influence of the object on the freestream flow which provides a qualitative understanding of how virtual mass is affected by viscous effects and the presence of a wake. As the Reynolds number increases, the wake boundary becomes narrower and supports a potential flow assumption for high Reynolds number

flows. This behavior is currently the basis for implementing potential flow solutions for virtual mass in flow analysis.

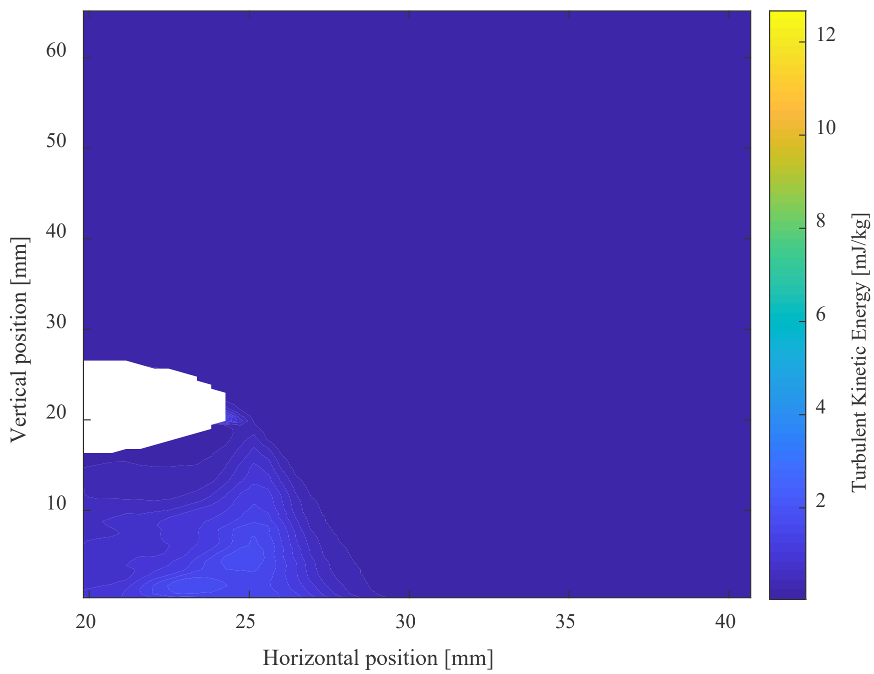

Figure 31: Cylinder 120 [mm/s] turbulent kinetic energy map

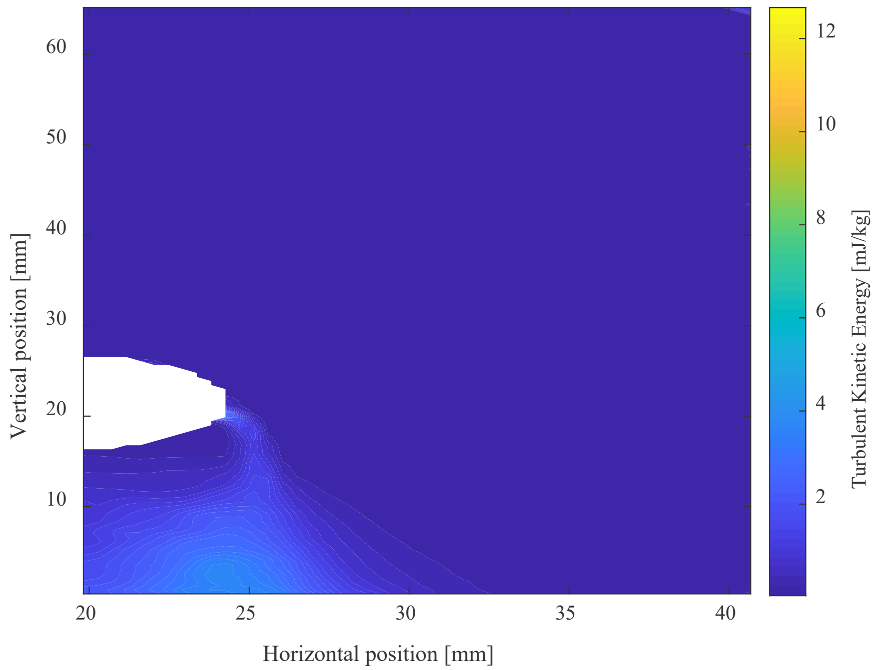

Figure 32: Cylinder 150 [mm/s] turbulent kinetic energy map

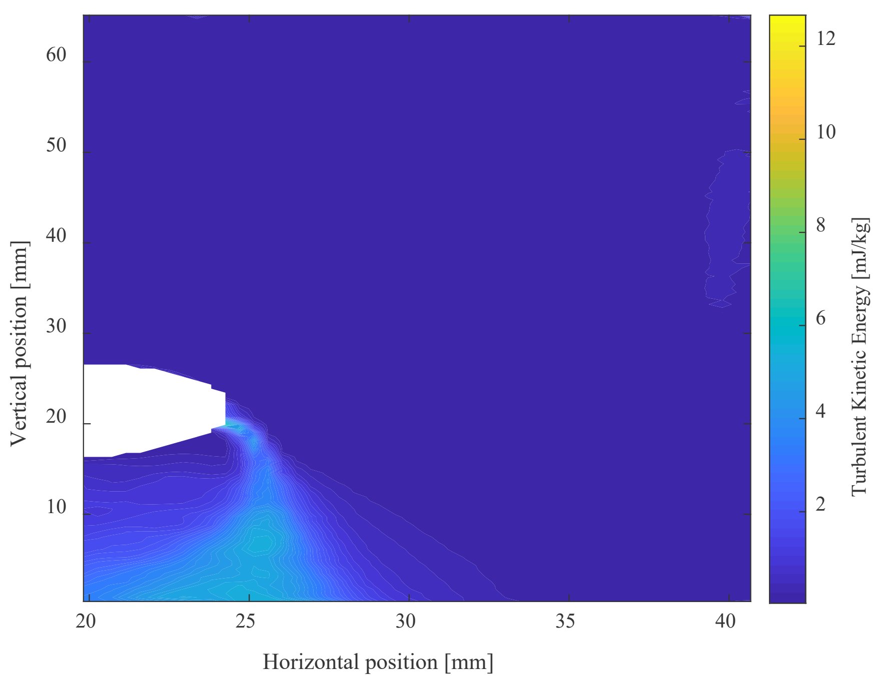

Figure 33: Cylinder 210 [mm/s] turbulent kinetic energy map

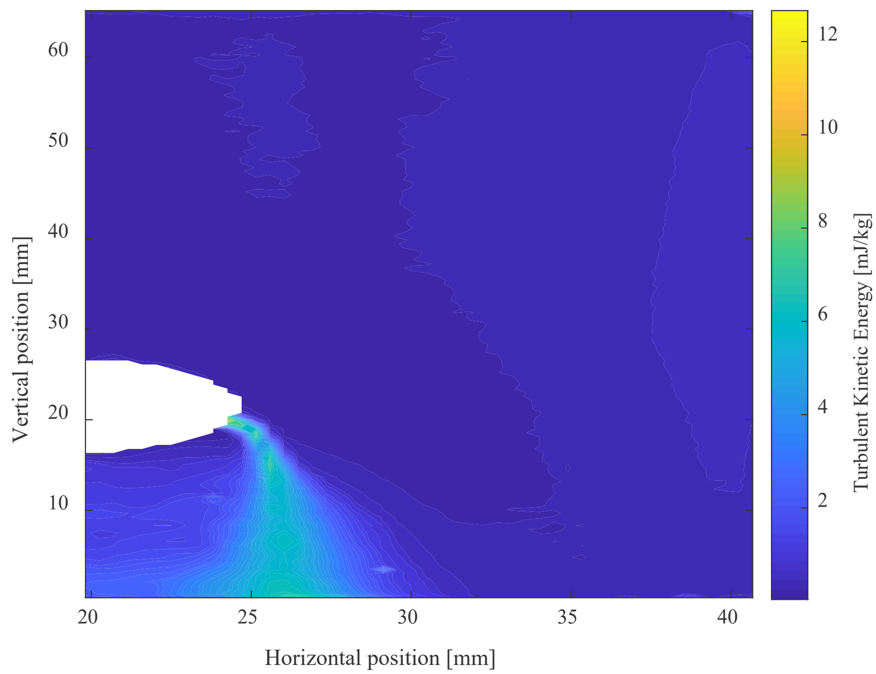

Figure 34: Cylinder 250 [mm/s] turbulent kinetic energy map

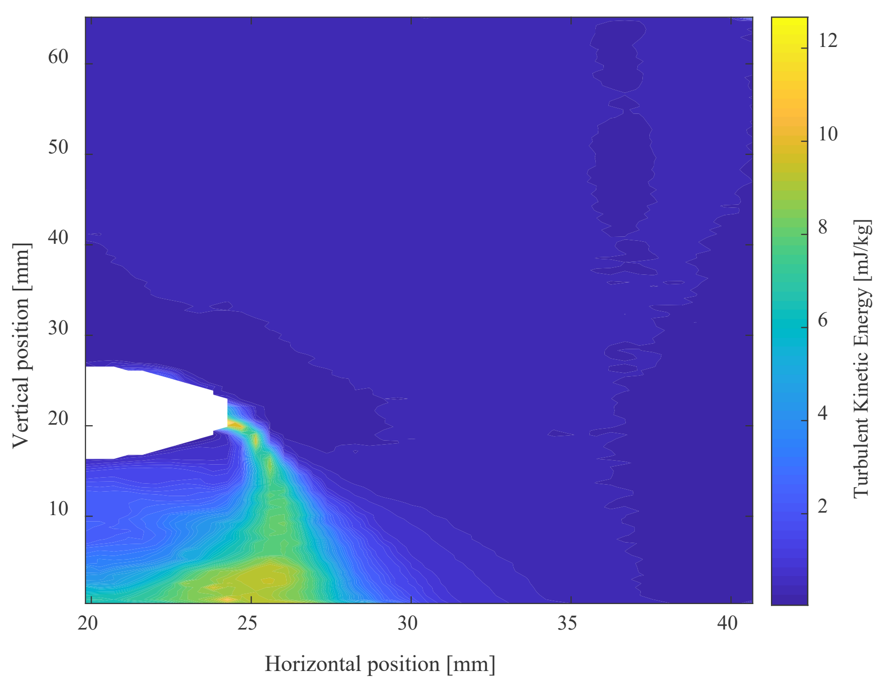

Figure 35: Cylinder 270 [mm/s] turbulent kinetic energy map

Because of the planar wake flow occurring from the cylinder the virtual mass can be treated similar to an infinite cylinder analysis and allows a direct comparison to its potential flow solution. The potential flow solution is obtained by integrating flow's kinetic energy the cross sectional area of the fluid from the cylinder surface into an infinite fluid domain as shown in eq. (58)-(62):

$$C_{VM} = \frac{m_a^{'}}{m_d^{'}} = \frac{KE_f^{'}}{KE_{ref}^{'}} \tag{58}$$

$$KE_{ref}^{'} = \frac{1}{2} m_d^{'} U^2 = \frac{1}{2}\rho A U^2 = \frac{1}{2}\rho\pi R^2 U^2 \tag{59}$$

$$KE_f^{'} = \int_0^{2\pi}\int_R^{\infty}\left(\frac{1}{2}\rho \mathrm{v}_r^{\,2}\right) r\,dr\,d\theta \tag{60}$$

$$\mathrm{v}_r^{\,2} = U_o^{\,2}\left(\frac{R^4}{r^4}\right)\left[\cos^2(\theta) + \sin^2(\theta)\right] \tag{61}$$

$$C_{VM} = \frac{KE_f^{'}}{KE_{ref}^{'}} = \frac{\frac{1}{2}\rho\pi R^2 U_o^{\,2}}{\frac{1}{2}\rho\pi R^2 U_o^{\,2}} = 1 \tag{62}$$

where ρ is the fluid density, R is the cylinder radius, and U_o is the speed the cylinder moves at in a stationary fluid. The analytical solution is equivalent to a stationary cylinder with a moving flow domain, a proof is provided in Appendix B. When considering the experimental data, the integration over an infinite flow domain is numerically approximated as discussed in Section 4.1 but instead on a per unit length basis and does not require a volume integral of the flow domain which results in eq. (63)-(65):

$$KE_f^{'} = \sum_{i=1}^{\#\text{of cells}} \frac{1}{2}\rho \Delta x_i \Delta y_i \mathrm{v}_{r,i}^{\,2} \tag{63}$$

$$KE_{ref} = \frac{1}{2}\rho\pi R^2 U_o^{\,2} \tag{64}$$

$$C_{VM} = \frac{\sum_{i=1}^{\#\text{of cells}} \frac{1}{2}\rho \Delta x_i \Delta y_i \mathrm{v}_{r,i}^{\,2}}{\frac{1}{2}\rho\pi R^2 U_o^{\,2}} \tag{65}$$

Where Δx_i is the horizontal cell width, Δy_i is the vertical cell width, $v_{r,i}$ is the relative measured fluid velocity, R is the cylinder radius, and U_o^2 is the inlet velocity. The inlet velocity was subtracted from the flow field to make the relative velocity appear that the cylinder is moving in a stationary flow domain to make qualitative comparisons to Lamb's derivation easier since it was derived for a moving object in a static infinite fluid. Figure 36 shows the calculated virtual mass coefficient for each Reynolds number measured with 95% confidence uncertainty intervals included and provides comparison to the potential flow solution.

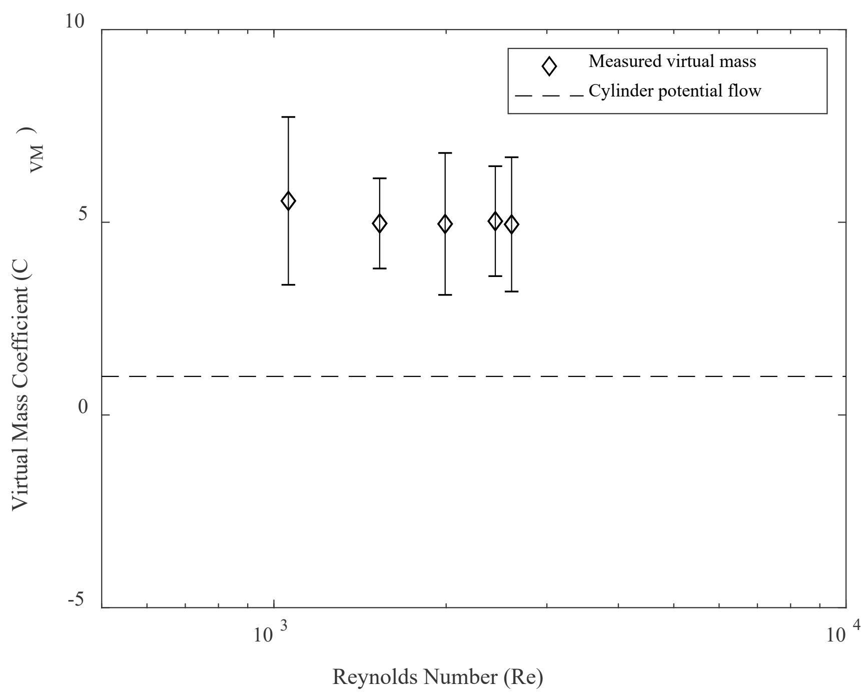

Figure 36: Cylinder measured virtual mass coefficient versus Reynolds number

Looking at the nominal trend the calculated virtual mass is relatively constant across the five flow speeds. There is a slight decrease in the virtual mass coefficient with increasing Reynolds number although the decrease is not substantial. Because potential flow assumptions are allowed at very high Reynolds number it would be expected that as the flow speed increased the calculated virtual mass would trend towards the potential flow value of $C_{VM} = 1$. The most notable trend observed is the virtual mass coefficient being much larger than the potential flow solution. Determining the virtual mass coefficient for objects in viscous flows has been an active research area with no accepted method for quantifying the virtual mass in the presence of a wake. Experiments to consider viscosity have been performed on sinusoidal oscillating cylinders with a force decomposition used to back out the virtual mass coefficient. However, experimental data from several studies have been contradictory [48] which adds to the open ended nature of determining virtual mass with viscous effects. When considering an energy balance perspective of a moving cylinder in a stationary fluid, the virtual mass describes the kinetic energy that is being added to the fluid by the object moving fluid particles out of its path. This is apparent when considering the streamlines of a moving cylinder or sphere in potential flow. From a control volume analysis from an energy balance perspective, the difference between a potential flow and viscous flow both in steady state is the presence of the drag force. The moving cylinder is performing work on the fluid through the viscous shear stresses and pressure gradient which appears as the total drag force. The source of kinetic energy in the wake comes from this drag force acting over a set distance the object has traveled. Because the viscosity prevents the flow behind the cylinder from mirroring the front side as would occur in potential flow, the flow domain needed to capture the entire influence of the object would likely need to include the entire wake. This would be impractical from an experimental perspective to capture the entire wake while still maintaining adequate spatial resolution. For instance, turbulent planar wakes can take up to 1000 diameters downstream to become self-persevering [49].

A control volume energy balance between the potential flow and viscous flow solutions shows that the difference is the energy added to the fluid by the drag work. A possible method to obtain the potential flow solution from a real viscous flow is to determine the drag work performed in the portion of the wake visible in the field of view and subtract the drag work from the fluid's total integrated kinetic energy to obtain the potential flow kinetic energy. The drag work was obtained by multiplying the calculated form drag on the cylinder determined by the pressure distribution and multiplied by the wake length visualized in the field of view. Subtracting the drag work from the integrated kinetic energy is expressed as a modification to eq. (65) resulting in eq.(66):

$$C_{VM,potential} = \frac{\sum_{i=1}^{\#\text{of cells}} \frac{1}{2}\rho \Delta x_i \Delta y_i \mathrm{v}_{r,i}^{\ 2} - F_{D,f}^{\ '} \Delta L_{wake}}{\frac{1}{2}\rho \pi R^2 U_o^{\ 2}} \tag{66}$$

where $F_{D,f}^{\ '}$ is the form drag force per unit length, and ΔL_{wake} is the wake length included in the flow domain integration.

The subtraction of the drag work from the visible flow field evaluating the potential flow virtual mass from the measured value. This was viewed appropriate by considering the integrated kinetic energy proceeding further into the wake. Figure 37 shows a plot of the integrated kinetic energy per unit length of the flow domain for the 250 mm/s flow case across increasing integration layers into the wake. The integration layer begins from the direct back side of the cylinder and increases by one cell distance vertically downward into the wake.

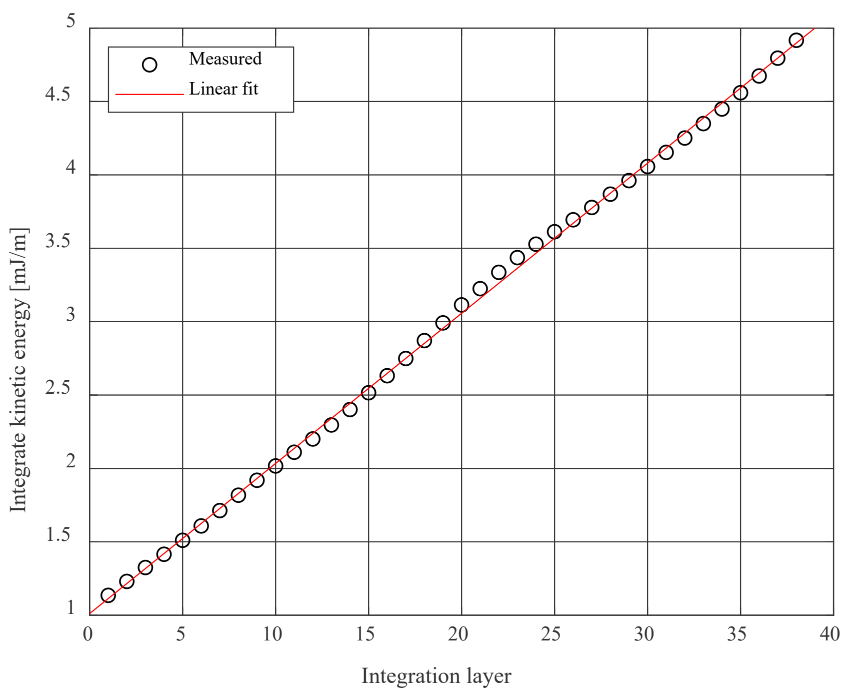

Figure 37: Integrated kinetic energy with increasing distance into wake

The nominal trend of the kinetic energy with increasing integration layers corresponds to a linear fit a with simple regression value of $R^2 = 0.997$. The significance of this linear trend is that incremental kinetic energy addition from the wake is not affected by the viscous dissipation within the wake. If the dissipation was non-negligible, increasing distance into wake would result in integrated kinetic energy plateauing. This would result from incremental kinetic energy decreasing to zero which corresponds to the viscous dissipation eventually causing the wake to return to the freestream conditions. This was used to justify the consideration of the drag work in the energy balance in eq. (66).

Figure 38 shows the results obtained from evaluating eq. (66) where two different form drag forces were input to determine the difference between using the calculated form drag from the measured pressure distribution and drag coefficients available from literature for the Reynold numbers measured.

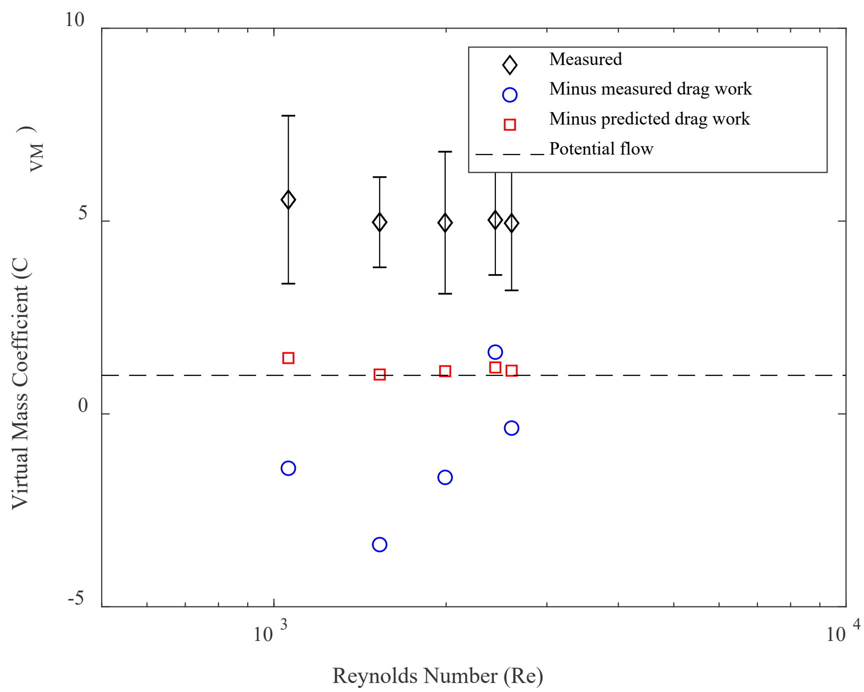

Figure 38: Cylinder measured virtual mass coefficient with drag work subtracted

Looking at the virtual mass coefficient values using the measured form drag reveals that all but one test had non-physical values. The calculated drag coefficient values are compared against literature in Figure 39 which shows the four non-physical values corresponded to over predicted drag coefficient values. The one value that showed a return to the potential flow value was occurring at 250 mm/s and had the best agreement with the value from literature. Using the predicted drag coefficient values to determine the form drag force resulted in a good agreement between the virtual mass coefficient and the potential flow solution.

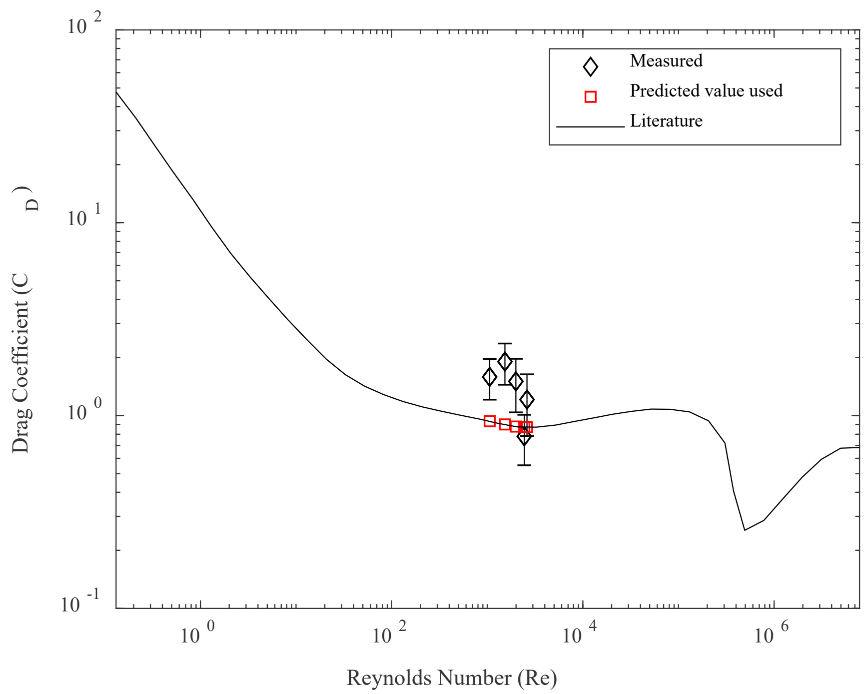

Figure 39: Cylinder measured drag coefficient versus Reynolds number

The agreement when using the predicted drag coefficient demonstrates the sensitivity this method has to the form drag as expected and highlights that the pressure field obtained from the PIV data resulted in an overestimated form drag. The overestimation of the form drag likely comes from the spatial resolution as discussed in Section 5.1. Table 10 lists the calculated virtual mass coefficient values with uncertainty intervals and the result of subtracting the drag work. It is important that to mention that reported virtual mass coefficient does not necessarily reflect what the true virtual mass coefficient is for the cylinder at these specific Reynolds numbers. The agreement of the virtual mass with the predicted drag work subtracted suggests that the measured virtual mass in the field of view is accurate, but the true virtual mass coefficient would likely require full visualization of the entire wake.

Table 10: Cylinder virtual mass coefficient w/ 95% confidence

Re	**C_{VM}**	**Measurement Uncertainty**	**Random Uncertainty**	**Total Uncertainty**	**C_{VM} (minus drag work)**	**C_{VM}(minus drag work w/ literature C_D)**
1059	5.55	±4.651E-4	±1.089	±1.089	-1.41	1.3926
1530	4.97	±7.068E-4	±0.585	±0.585	-3.39	0.9885
1992	4.96	±7.334E-4	±0.921	±0.921	-1.65	1.1902
2438	5.03	±5.110E-4	±0.713	±0.713	1.60	1.2050
2603	4.95	±5.736E-4	±0.871	±0.871	-0.37	1.1212

The open ended nature of determining the virtual mass for the two-dimensional planar flow case of the cylinder revealed that determining the virtual mass for the recorded bubble data would be hampered by the three-dimensional effects of the bubble rise, such as the spiraling bubble motion, helical vortex shedding, and deformable surface. Additionally, the virtual mass potential flow solution of a sphere requires a volume integral to be performed which planar PIV data would not be able to support without resulting in large uncertainty and an overestimation of the virtual mass. As the bubble rises any vortex that had been shed would be rotated around the centroid axis which causes the kinetic energy of the vortex to be treated as axisymmetric. This axisymmetric assumption would not be physical because of the alternating vortex shedding that occurs and would result in an artificial vortex ring of kinetic energy existing in a single time frame. However, it is possible that with a sufficiently long collection time that the time averaged three-dimensional flow field would be axisymmetric. Obtaining this long collection time with a bubble consistently in the laser sheet would be non-trivial. An alternative would be to use stereoscopic PIV to obtain three-dimensional information about the flow field and would greatly allow the uncertainty of the bubble within the laser sheet to be incorporated.

6 CONCLUSIONS

Modern fluid measurement techniques have the capability to improve understanding of various flow phenomena. This study examined the drag coefficient of rising ellipsoidal bubbles and the virtual mass coefficient on a stationary cylinder rod. The drag coefficient of ellipsoidal bubbles for five varying diameters have been experimentally measured with PIV which allowed the form and skin drag coefficients to be directly measured in addition to the total drag coefficient. Flow over a stationary cylinder rod for five Reynolds numbers utilized a method that allowed the virtual mass coefficient to be measured in steady state conditions. The cylinder virtual mass analysis revealed several sensitivities when measuring virtual mass in a flow field with significant wake effects. A method for retrieving the potential flow virtual mass from a measurement was showcased and identified improvements to experimentally measure virtual mass in real fluid flows. A rigorous uncertainty analysis was performed for drag and virtual mass coefficients using Kline-McClintock with uncertainty propagated, when known, from independent measured variables.

6.1 Significance of Work

The measured total drag coefficient used the traditional measurement technique of tracking the bubble velocity based on consecutive image frames. The use of modern digital imaging allowed the bubble centroid to be tracked objectively. The simultaneous use of PIV resulted in the form drag force, and by extension skin drag force, to be directly measured on rising ellipsoidal bubbles. This provided experimental observation for the trend of increasing form drag with increasing bubble diameter which is often described from a qualitative perspective.

A spatial integration of the kinetic energy measured in the flow around an object was applied to PIV data on a cylinder. This method allowed the virtual mass coefficient to be measured for steady state conditions which previously had been limited to only transient flow conditions in order to measure the virtual miss. The kinetic energy integration method follows the original derivation of virtual mass and provides direct comparison of the viscous flows to potential flow solutions. The removal of predicted drag work retrieved the potential flow solution which showcases the method's potential to isolate the viscous effects on the virtual mass coefficient.

6.2 Assumptions and Limitations

A key assumption used in the measurement of drag coefficient was that the bubble entered the PIV laser plane directly in the center of the bubble. If the bubble is not centered while in the laser plane, the bubble image masked will have a smaller cross section along with a different velocity and pressure distribution around the bubble interface. The uncertainty contribution from this was not considered as a part of the uncertainty analysis performed in this work. Another significant assumption applied was a steady state approximation for the bubble and cylinder force balances. This assumption was deemed appropriate because of its common usage in other drag coefficient experiments with similar experimental setups and provided a direct comparison to other experimental data.

Two-dimensional flow was assumed for the bubble's motion during its residence in the laser plane. This assumption was made because of planar PIV's inability to resolve three-dimensional effects from the bubble and fluid motion, such as a helical rise path, vortex shedding, and out-of-plane motion. The largest impact of out-of-plane motion was the increase to velocity uncertainty, and was a dominant factor in making the bubble off center in the laser plane. This two-dimensional flow assumption was similarly applied to the cylinder rod flow and resulted in the wake being evaluated as planar flow. Another important assumption was the velocity uncertainty determination. As mentioned previously in Section 4.4, there is no currently accepted best practice for quantifying the uncertainty in PIV velocity fields. There are several different methods for determining the uncertainty from the cross-correlation performed in the interrogation areas. This uncertainty was not considered in the analysis because the cross-correlation algorithm used in DynamicStudio is proprietary and not available. The inclusion of this uncertainty source would increase the velocity uncertainty.

6.3 Observations

Measured drag coefficient on ellipsoidal agreed with previous work and included total, form, and skin drag forces. Total drag coefficient was measured using the traditional technique of equating the total drag force to the buoyancy force and resulted in values consistently largely than prior experimental data and resulting correlations. However, when considering the uncertainty the predicted values do fall within the 95% confidence interval. The measured terminal velocities were lower when compared to prior work and was the source of the larger drag coefficient values which pointed to the influence of surface tension from tracer particles. Form drag was directly measured on the rising bubbles and showed a nominal trend of increasing form drag with bubble size which has agreement with qualitative understanding of form drag behavior on bubbles. An important observation from the uncertainty analysis was the significant uncertainty on the form drag force. This uncertainty provided improvements for future experiments measuring the pressure distribution around a bubble and highlights the importance of spatial resolution for resolving the bubble interface.

The virtual mass coefficient for an object in a real fluid flow was shown to require more experimentation to fully capture. Based on the definition of virtual mass representing that fluid mass with kinetic energy influenced by an object it appears that the entire wake needs to be visualized to make an objective determination on the extent of the virtual mass. The linear increase in kinetic energy in the wake showed that viscous dissipation was negligible which allowed the potential flow solution for each Reynolds number case to be retrieved by subtracting the predicted drag work from the flow domain's integrated kinetic energy. This work on the virtual mass coefficient for a cylinder showed that planar PIV would be incapable of measuring virtual mass on rising single bubbles without significant uncertainty from three-dimensional effects.

6.4 Future Work

Further studies in drag coefficient using PIV would benefit from improved spatial resolution to reduce uncertainty on the measured form drag coefficient. The measured form drag force is highly dependent on the pressure distribution along the bubble interface and increasing the number of velocity vectors around the bubble provides greater fidelity when quantifying the pressure distribution and thereby the form drag force. The use of stereoscopic PIV would eliminate the need for two-dimensional and azimuthal assumptions This would greatly reduce the effects of out-of-plane motion on velocity uncertainty and is recommended for future experimental setups.

The virtual mass coefficient analysis has identified several improvements that can be made to future experiments. The impact of the wake dynamics needs to be well characterized and would benefit from flow over the stationary cylinder over a large range of Reynolds numbers. Using another fluid to generate varying wake structures such as steady wakes with a separation region, Von Karman vortex sheets, laminar wakes. Operating at very high Reynolds number would provide experimental confirmation of virtual mass approximating the potential flow solution which would be expected considering that wake size would decrease. In addition to a greater operating range of Reynolds number, a large enough field of view to capture the entire wake would remove subjectivity on the wake's ultimate influence on the virtual mass and allow the presented method for steady state flows to be fully explored.

The measured virtual mass values with measured drag work subtracted produced unphysical values that did not correspond to the potential flow values. Using a predicted drag coefficient for the correspond Reynolds numbers resulted in drag work values that did cause the measured virtual mass values to return to the potential flow solution. This highlights the need to improve the form drag characterization on the cylinder rod. An important consideration from the virtual mass experiments is the current inability to objectively measure the virtual mass coefficient on a rising bubble in steady state that can characterize the influence of wake dynamics and three-dimensional effects. Further studies in characterizing this influence would be considerably improve the current understanding of virtual mass.

REFERENCES

[1] Division of Risk Assessment and Special Projects, "TRACE V5.0 Theory Manual: Field Equations, Solution Methods, and Physical Models," Washington, DC.

[2] M. Ishii and T. Hibiki, *Thermo-Fluid Dynamics of Two-Phase Flow*, 2nd ed. New York: Springer, 2011.

[3] M. Raffel, C. E. Willert, S. T. Wereley, and J. Kompenhans, *Particle Image Velocimetry: A Practical Guide*, 2nd ed. Springer, 2007.

[4] W. L. Haberman and R. K. Morton, "An Experimental Investigation of the Drag and Shape of Air Bubbles Rising in Various Liquids," 1953.

[5] T. Z. Harmathy, "Velocity of large drops and bubbles in media of infinite or restricted extent," *AIChE J.*, vol. 6, no. 2, pp. 281–288, 1960.

[6] R. Clift, J. R. Grace, and M. E. Weber, *Bubbles, Drops and Particles*. Academic Press Inc., 1978.

[7] D. W. Moore, "The boundary layer on a spherical gas bubble," *Journal of Fluid Mechanics*, vol. 16, no. 2. pp. 161–176, 1963.

[8] G. B. Wallis, "The terminal speed of single drops or bubbles in an infinite medium," *International Journal of Multiphase Flow*, vol. 1, no. 4. pp. 491–511, 1974.

[9] M. Ishii and N. Zuber, "Drag coefficient and relative velocity in bubble droplet or particulate flows.pdf," *AIChE Journal*, vol. 25, no. 5. pp. 843–855, 1979.

[10] A. Tomiyama, I. Kataoka, I. Zun, and T. Sakaguchi, "Drag Coefficients of Single Bubbles under Normal and Micro Gravity Conditions," *JSME Int. J. Ser. B Fluids Therm. Eng.*, vol. 41, no. 2, pp. 472–479, 1998.

[11] D. Zhang, N. G. Deen, and J. A. M. Kuipers, "Numerical simulation of the dynamic flow behavior in a bubble column: A study of closures for turbulence and interface forces," *Chem. Eng. Sci.*, vol. 61, no. 23, pp. 7593–7608, 2006.

[12] A. Tomiyama, "Drag, lift, and virtual mass forces acting on a single bubble," in *Third International Conference on Two-Phase Flow Modeling and Experimentation*, 2004.

[13] N. G. Deen, *An Experimental and Computational Study of Fluid Dynamics in Gas-Liquid Chemical Reactors*, no. August. 2001.

[14] G. Kelbaliyev and K. Ceylan, “Development of new empirical equations for estimation of drag coefficient, shape deformation, and rising velocity of gas bubbles or liquid drops,” *Chem. Eng. Commun.*, 2007.

[15] H. Lamb, *Hydrodynamics*, 6th ed. Dover Publications, 1932.

[16] A. Basset, *A Treatise on Hydrodynamics Vol 2.* Deighton, Bell, Cambridge: Cambridge University Press, 1888.

[17] L. Van Wijngaarden and D. J. Jeffrey, “Hydrodynamic interaction between gas bubbles in liquid,” *J. Fluid Mech.*, vol. 77, no. 1, pp. 27–44, 1976.

[18] J. A. Geurst, “Virtual mass in two-phase bubbly flow,” *Phys. A Stat. Mech. its Appl.*, vol. 129, no. 2, pp. 233–261, 1985.

[19] B. U. Felderhof, “Virtual mass and drag in two-phase flow,” *Journal of Fluid Mechanics*, vol. 225, no. 1. p. 177, 1991.

[20] R. Mei and J. F. Klausner, “Unsteady force on a spherical bubble at finite Reynolds number with small fluctuations in the free-stream velocity,” *Phys. Fluids*, vol. A4, no. 1, pp. 63–70, 1992.

[21] K. Sankaranarayanan, X. Shan, I. G. Kevrekidis, and S. Sundaresan, “Analysis of drag and virtual mass forces in bubbly suspensions using an implicit formulation of the lattice Boltzmann method,” *J. Fluid Mech.*, vol. 452, pp. 61–96, 2002.

[22] C. D. Ohl, A. Tijink, and A. Prosperetti, “The added mass of an expanding bubble,” *J. Fluid Mech.*, vol. 482, no. 482, pp. 271–290, 2003.

[23] A. A. Kendoush, “The virtual mass of an oblate-ellipsoidal bubble,” *Phys. Lett. Sect. A Gen. At. Solid State Phys.*, vol. 366, no. 3, pp. 253–255, 2007.

[24] W. D. Fullmer and M. A. L. De Bertodano, “An Assessment of the Virtual Mass Force in RELAP5/MOD3.3 for the Bubbly Flow Regime,” *Nucl. Technol.*, vol. 191, no. 2, pp. 185–192, 2015.

[25] N. R. C. Job and W. Code, “RELAP5 / MOD3 Code Manual,” vol. 5, 1995.

[26] R. J. N. Bernier, “Unsteady two-phase flow instrumentation and measurement,” California Institute of Technology, 1982.

[27] “IFA 300 Constant Temperature Anemometer System Operation Manual.” TSI Incorporated, Shoreview, MN, 2010.

[28] I. Kataoka, M. Ishii, and A. Serizawa, "Local formulation and measurements of interfacial area concentration in two-phase flow," *Int. J. Multiph. Flow*, vol. 12, no. 4, pp. 505–529, Jul. 1986.

[29] Q. Wu and M. Ishii, "Sensitivity study on double-sensor conductivity probe for the measurement of interfacial area concentration in bubbly flow," *Int. J. Multiph. Flow*, vol. 25, no. 1, pp. 155–173, 1999.

[30] S. Kim, X. Y. Fu, X. Wang, and M. Ishii, "Development of the miniaturized four-sensor conductivity probe and the signal processing scheme," *Int. J. Heat Mass Transf.*, vol. 43, no. 22, pp. 4101–4118, 2000.

[31] Z. Dang *et al.*, "Experimental study of interfacial characteristics of vertical upward air-water two-phase flow in 25.4 mm ID round pipe," *Int. J. Heat Mass Transf.*, vol. 108, pp. 1825–1838, 2017.

[32] A. Boutier, *Laser Velocimetry in Fluid Mechanics*. Hoboken, NJ: John Wiley & Sons, Inc., 2013.

[33] J. Westerweel, "Fundamentals of Digital Particle Image Velocimetry," *Meas. Sci. Tech.*, vol. 8, no. 12, pp. 1379–1392, 1997.

[34] R. J. Adrian and J. Westerweel, *Particle Image Velocimetry*. 2011.

[35] C. Brücker, "Structure and dynamics of the wake of bubbles and its relevance for bubble interaction," *Phys. Fluids*, vol. 11, no. 7, pp. 1781–1796, 1999.

[36] S. Hosokawa, S. Moriyama, A. Tomiyama, and N. Takada, "PIV Measurement of Pressure Distributions about Single Bubbles," *J. Nucl. Sci. Technol.*, vol. 40, no. 10, pp. 754–762, 2003.

[37] J. Ortiz-Villafuerte, W. D. Schmidl, and Y. A. Hassan, "Three-dimensional PIV measurements of bubble drag and lift coefficients in restricted media," *Rev. Mex. Fis.*, vol. 59, no. 5, pp. 444–452, 2013.

[38] X. Yan, Y. Jia, L. Wang, and Y. Cao, "Drag coefficient fluctuation prediction of a single bubble rising in water," *Chem. Eng. J.*, vol. 316, pp. 553–562, 2017.

[39] R. D. Keane and R. J. Adrian, "Optimization of particle image velocimeters: II. Multiple pulsed systems," *Meas. Sci. Technol.*, vol. 2, no. 10, pp. 963–974, 1991.

[40] R. Hain and C. J. Kähler, "Fundamentals of multiframe particle image velocimetry

(PIV)," *Exp. Fluids*, vol. 42, no. 4, pp. 575–587, 2007.

[41] J. O. Dabiri, S. Bose, B. J. Gemmell, S. P. Colin, and J. H. Costello, "An algorithm to estimate unsteady and quasi-steady pressure fields from velocity field measurements," *J. Exp. Biol.*, vol. 217, no. 3, pp. 331–336, 2014.

[42] K. N. Lucas, J. O. Dabiri, and G. V. Lauder, "A pressure-based force and torque prediction technique for the study of fish-like swimming," *PLoS One*, vol. 12, no. 12, pp. 1–30, 2017.

[43] H. Lamb, "Motion of a Sphere," in *Hydrodynamics*, 6th ed., Dover, Ed. 1932, pp. 123–125.

[44] J. J. Charonko and P. P. Vlachos, "Estimation of uncertainty bounds for individual particle image velocimetry measurements from cross-correlation peak ratio," *Meas. Sci. Technol.*, vol. 24, no. 6, 2013.

[45] B. H. Timmins, B. W. Wilson, B. L. Smith, and P. P. Vlachos, "A method for automatic estimation of instantaneous local uncertainty in particle image velocimetry measurements," *Exp. Fluids*, vol. 53, no. 4, pp. 1133–1147, 2012.

[46] B. Jackson, "An Experimental Study of Laminarization Induced by Acceleration and Curvature," Oregon State University, 2012.

[47] L. Fan and K. Tsuchiya, *Bubble Wake Dynamics In Liquids And Liquid-Solid Suspensions*. Stoneham, MA: Butterworth-Heinemann, 1990.

[48] C. E. Brennen, "A Review of Added Mass and Fluid Intertial Forces," 1982.

[49] F. M. . White, *Viscous Fluid Flow*, 3rd ed. McGraw Hill Education, 2006.

NOMENCLATURE

Letters

A	Cross Sectional Area
C_D	Drag Coefficient
d , D	Diameter
F	Force
g	Gravitational Constant
KE	Kinetic Energy
l	Characteristic Length
u	Velocity
U	Mean Velocity
R	Cross-Correlation Coefficient
r	Radius
$\boldsymbol{s}$	Particle Displacement Vector
$\forall$	Volume
$\boldsymbol{X}$	Light Intensity Position Vector

Greek Letters

α	Void Fraction
σ	Surface Tension
ρ	Density
μ	Dynamic Viscosity
τ	Relaxation Time Constant
γ	Dielectric Constant

Subscripts

b	Bubble
c	Continuous Phase
d	Dispersed Phase
e	Spherical Equivalent
f	Liquid Phase

$field$	Flow Domain
g	Gas Phase
o	Reference Flow Condition
p	Particle
r , R	Relative
ref	Reference Kinetic Energy Condition
T	Terminal Velocity
∞	Spherical Sphere in Infinite Medium

APPENDIX A: UNCERTAINTY ANALYSIS

An uncertainty analysis was performed for calculated values presented in the work using the Kline-McClintock method. The independent measured parameters included: velocity, bubble volume, cylinder diameter, pulse timing, image-pair timing, calibration length scale, and pixel calibration length. The subsections below detail how the Kline-McClintock was performed for drag coefficient and virtual mass coefficient. The uncertainty contribution from dependent variable, for example the drag coefficient depends on uncertainty from the total or form drag force, relative bubble terminal velocity, and bubble cross sectional area. The uncertainty for dependent variables within each of these variables is similarly propagated until the independent variables are the only uncertainty source for a variable. Because the BIL facility is operated at a nominal $T = 21^{o}C$ temperature and in an unpressurized environment, thermophysical property values (density, viscosity, surface tension) for water and air were identified using the National Institute of Standards and Technology (NIST) Chemistry WebBook and uncertainty contribution from these values were not considered.

Drag Coefficient Uncertainty Propagation:

The total drag coefficient is calculated from eq. (67):

$$C_D = \frac{2F_D}{\rho_f A \mathrm{v}_r^{\,2}} \tag{67}$$

where F_D is the total drag force, ρ_f is the fluid density, A is the bubble's spherical equivalent cross sectional area, and v_r is the bubble's relative terminal velocity. Applying Kline-McClintock uncertainty propagation to eq. (67) results in eq. (68) which identifies uncertainty sensitivity terms and the uncertainty contribution of each depend variable on the right hand side of eq. (67). The uncertainty sensitivity terms are defined by eq. (69)-(71)

$$\sigma_{C_D} = \left[\left(\frac{\partial C_D}{\partial F_D}\sigma_{F_D}\right)^2 + \left(\frac{\partial C_D}{\partial \mathrm{v}_r}\sigma_{\mathrm{v}_r}\right)^2 + \left(\frac{\partial C_D}{\partial A}\sigma_A\right)^2\right]^{0.5} \tag{68}$$

$$\frac{\partial C_D}{\partial F_D} = \frac{2}{\rho_f A \mathrm{v}_r^{\ 2}} \tag{69}$$

$$\frac{\partial C_D}{\partial \mathrm{v}_r} = \frac{-4F_D}{\rho_f A \mathrm{v}_r^{\ 3}} \tag{70}$$

$$\frac{\partial C_D}{\partial A} = \frac{-2F_D}{\rho_f A^2 \mathrm{v}_r^{\ 2}} \tag{71}$$

The uncertainty propagation for either total or form drag coefficient use the same definitions listed above expect using the appropriate drag force in the equations

Total Drag/Buoyancy Force Uncertainty Propagation:

The total drag force uncertainty can be substituted by the buoyancy force and its uncertainty because of the steady state assumption applied to the bubble force balance.

$$F_D = F_B = \frac{\pi}{6} g \Delta\rho D_{eq}^{\ 3} \tag{72}$$

$$\sigma_{F_D} = \frac{\partial F_D}{\partial D_{eq}} \sigma_{D_{eq}} \tag{73}$$

$$\frac{\partial F_D}{\partial D_{eq}} = \frac{\pi}{3} g \Delta\rho D_{eq}^{\ 2} \tag{74}$$

Looking at eq. (72)-(74) it can be seen that source of uncertainty for the total drag force comes from bubble's spherical equivalent diameter.

Form Drag Uncertainty Propagation:

The form drag force is calculated by taking the dot product of the net pressure force and the normal vector opposite of the bubble's velocity as shown in eq. (75), with normal vector components defined in eq. (76)-(77).

$$F_{D,\mathrm{form}} = \vec{F}_{net} \cdot \hat{n}_{b,velocity} = F_{net,x} n_{b,x} + F_{net,y} n_{b,y} \tag{75}$$

$$n_{b,x} = -\frac{\mathrm{v}_{b,x}}{\mathrm{v}_b} \tag{76}$$

$$n_{b,y} = -\frac{\mathrm{v}_{b,y}}{\mathrm{v}_b} \tag{77}$$

The uncertainty propagation for the form drag force magnitude is shown below and considers the horizontal and vertical components of the net pressure force and velocity normal vector accompanying sensitivity terms.

$$\sigma_{F_{D,\text{form}}} = \left[\left(\frac{\partial F_{D,\text{form}}}{\partial F_{net,x}} \sigma_{F_{net,x}} \right)^2 + \left(\frac{\partial F_{D,\text{form}}}{\partial F_{net,y}} \sigma_{F_{net,y}} \right)^2 + \left(\frac{\partial F_{D,\text{form}}}{\partial n_x} \sigma_{n_x} \right)^2 + \left(\frac{\partial F_{D,\text{form}}}{\partial n_y} \sigma_{n_y} \right)^2 \right]^{0.5} \tag{78}$$

$$\frac{\partial F_{D,\text{form}}}{\partial F_{net,x}} = n_x \tag{79}$$

$$\frac{\partial F_{D,\text{form}}}{\partial F_{net,y}} = n_y \tag{80}$$

$$\frac{\partial F_{D,\text{form}}}{\partial n_x} = F_{net,x} \tag{81}$$

$$\frac{\partial F_{D,\text{form}}}{\partial n_y} = F_{net,y} \tag{82}$$

The uncertainty for each normal vector component is next identified as being dependent on the bubble terminal velocity magnitude and components. The uncertainty sources for the relative velocity is evaluated later in Appendix A: Uncertainty Analysis.

$$\sigma_{n_x} = \left[\left(\frac{\partial n_x}{\partial \mathrm{v}_{b,x}} \sigma_{\mathrm{v}_{b,x}} \right)^2 + \left(\frac{\partial n_x}{\partial \mathrm{v}_b} \sigma_{\mathrm{v}_b} \right)^2 \right]^{0.5} \tag{83}$$

$$\sigma_{n_y} = \left[\left(\frac{\partial n_y}{\partial \mathrm{v}_{b,y}} \sigma_{\mathrm{v}_{b,y}} \right)^2 + \left(\frac{\partial n_y}{\partial \mathrm{v}_b} \sigma_{\mathrm{v}_b} \right)^2 \right]^{0.5} \tag{84}$$

$$\frac{\partial n_x}{\partial \mathrm{v}_{b,x}} = -\frac{1}{\mathrm{v}_b} \tag{85}$$

$$\frac{\partial n_x}{\partial \mathrm{v}_b} = \frac{\mathrm{v}_{b,x}}{\mathrm{v}_b^{\;2}} \tag{86}$$

$$\frac{\partial n_y}{\partial \mathrm{v}_{b,y}} = -\frac{1}{\mathrm{v}_b} \tag{87}$$

$$\frac{\partial n_y}{\partial \mathrm{v}_b} = \frac{\mathrm{v}_{b,y}}{\mathrm{v}_b^{\;2}} \tag{88}$$

The net pressure force's horizontal and vertical components are analytically defined with eq. (89)-(90). These analytical definitions were numerically evaluated with the pressure field with eq. (91)-(92).

$$F_{net,x} = -\iint P \cdot \hat{n}_{x,surf}\, dS \tag{89}$$

$$F_{net,y} = -\iint P \cdot \hat{n}_{y,surf}\, dS \tag{90}$$

$$F_{net,y} = -P_i \Delta x_i \pi r_{cent,i} \tag{91}$$

$$F_{net,x} = -P_i \Delta y_i \pi r_{cent,i} \tag{92}$$

The uncertainty propagation for both components is performed below and is identical with the exception of the cell distance used.

$$\sigma_{F_{net,y}} = \left[\sum_{i=1}^{\#\text{of surface cells}} \left(\frac{\partial F_{net,y}}{\partial F_{net,y,i}} \sigma_{F_{net,y,i}} \right)^2 \right]^{0.5} = \left[\sum_{i=1}^{\#\text{of surface cells}} \sigma_{F_{net,y,i}}{}^2 \right]^{0.5} \tag{93}$$

$$\sigma_{F_{net,x}} = \left[\sum_{i=1}^{\#\text{of surface cells}} \left(\frac{\partial F_{net,x}}{\partial F_{net,x,i}} \sigma_{F_{net,x,i}} \right)^2 \right]^{0.5} = \left[\sum_{i=1}^{\#\text{of surface cells}} \sigma_{F_{net,x,i}}{}^2 \right]^{0.5} \tag{94}$$

$$\sigma_{F_{net,y,i}} = \left[\left(\frac{\partial F_{net,y,i}}{\partial \Delta x_i} \sigma_{\Delta x_i} \right)^2 + \left(\frac{\partial F_{net,y,i}}{\partial r_{cent,i}} \sigma_{r_{cent,i}} \right)^2 \right]^{0.5} \tag{95}$$

$$\sigma_{F_{net,x,i}} = \left[\left(\frac{\partial F_{net,x,i}}{\partial \Delta y_i} \sigma_{\Delta x_i} \right)^2 + \left(\frac{\partial F_{net,x,i}}{\partial r_{cent,i}} \sigma_{r_{cent,i}} \right)^2 \right]^{0.5} \tag{96}$$

$$\frac{\partial F_{net,y,i}}{\partial \Delta x_i} = -P_i \pi r_{cent,i} \tag{97}$$

$$\frac{\partial F_{net,y,i}}{\partial r_{cent,i}} = -P \Delta x_i \pi \tag{98}$$

$$\frac{\partial F_{net,x,i}}{\partial \Delta y_i} = -P_i \pi r_{cent,i} \tag{99}$$

$$\frac{\partial F_{net,x,i}}{\partial r_{cent,i}} = -P \Delta y_i \pi \tag{100}$$

To fully propagate uncertainty through the net pressure components the uncertainty from a cell width needed to be evaluated. The Kline-McClintock method is applied again to eq.

(101) resulting in eq. (102) where the uncertainty depends on the length scale calibration used for each trial.

$$\Delta x_i = \frac{l}{L}\Delta x_{i,pix} \tag{101}$$

$$\sigma_{\Delta x_i} = \left[\left(\frac{\partial \Delta x_i}{\partial l}\sigma_l\right)^2 + \left(\frac{\partial \Delta x_i}{\partial L}\sigma_L\right)^2\right]^{0.5} \tag{102}$$

$$\frac{\partial \Delta x_i}{\partial l} = \frac{1}{L}\Delta x_{i,pix} = \frac{\Delta x_i}{l} \tag{103}$$

$$\frac{\partial \Delta x_i}{\partial L} = -\frac{l}{L^2}\Delta x_{i,pix} = \frac{\Delta x_i}{L} \tag{104}$$

Additionally, the distance from the cell to centroid horizontally was used for the 180 degree revolution needed to complete the surface integral is defined by eq. (105). The uncertainty was similar propagated and also depended on the length scale calibration.

$$r_{cent,i} = x_{cent} - x_i = \Delta x_{cent,i} = \frac{l}{L}\Delta x_{cent,i,pix} \tag{105}$$

$$\sigma_{r_{cent,i}} = \left[\left(\frac{\partial r_{cent,i}}{\partial l}\sigma_l\right)^2 + \left(\frac{\partial r_{cent,i}}{\partial L}\sigma_L\right)^2\right]^{0.5} \tag{106}$$

$$\frac{\partial r_{cent,i}}{\partial l} = \frac{1}{L}\Delta x_{cent,i,pix} = \frac{\Delta x_{cent,i}}{l} \tag{107}$$

$$\frac{\partial r_{cent,i}}{\partial L} = -\frac{l}{L^2}\Delta x_{cent,i,pix} = \frac{\Delta x_{cent,i}}{L} \tag{108}$$

Skin Drag Uncertainty Propagation:

The measured skin drag coefficient had uncertainty propagation from both the total and form drag coefficients. The skin drag coefficient definition, eq. (109), resulted in a simple uncertainty propagation of the two different drag coefficients as shown in eq. (113)

$$C_{D,s} = C_{D,t} - C_{D,f} \tag{109}$$

$$\sigma_{C_{D,s}} = \left[\left(\frac{\partial C_{D,s}}{\partial C_{D,t}}\sigma_{C_{D,t}}\right)^2 + \left(\frac{\partial C_{D,s}}{\partial C_{D,f}}\sigma_{C_{D,f}}\right)^2\right]^{0.5} \tag{110}$$

$$\frac{\partial C_{D,s}}{\partial C_{D,t}} = 1 \tag{111}$$

$$\frac{\partial C_{D,s}}{\partial C_{D,f}} = -1 \tag{112}$$

$$\sigma_{C_{D,s}} = \left[\sigma_{C_{D,t}}{}^2 + \sigma_{C_{D,f}}{}^2 \right]^{0.5} \tag{113}$$

Area Uncertainty Propagation:

The cross sectional area uncertainty is only dependent on the bubble diameter uncertainty which depends on the bubble volume used.

$$A = \frac{\pi}{4} D_{eq}{}^2 \tag{114}$$

$$\sigma_A = \frac{\partial A}{\partial D_{eq}} \sigma_{D_{eq}} \tag{115}$$

$$\frac{\partial A}{\partial D_{eq}} = \frac{\pi}{2} D_{eq} \tag{116}$$

Diameter Uncertainty Propagation for V ≥ 0.1 [mL]:

For bubble volumes greater or equal to 0.1 mL, the bubble diameter was evaluated using the volume for a sphere and has uncertainty dependency on the syringe resolution from Setup 2 in Section 3.4.

$$D_{eq} = \left(\frac{6V}{\pi} \right)^{\frac{1}{3}} \tag{117}$$

$$\sigma_{D_{eq}} = \frac{\partial D_{eq}}{\partial V} \sigma_V \tag{118}$$

$$\frac{\partial D_{eq}}{\partial V} = \frac{1}{3} \left(\frac{6}{\pi V^2} \right)^{\frac{1}{3}} \tag{119}$$

Tate’s Law Uncertainty Propagation for V < 0.1 [mL]:

For bubble volumes smaller than

$$D_{eq} = \left(\frac{6 d_n \sigma}{g \Delta \rho} \right)^{\frac{1}{3}} \tag{120}$$

$$\sigma_{D_{eq}} = \frac{\partial D_{eq}}{\partial d_n}\sigma_{d_n} \tag{121}$$

$$\frac{\partial D_{eq}}{\partial d_n} = \frac{1}{3}\left(\frac{6\sigma}{d_n{}^2 g\Delta\rho}\right)^{\frac{1}{3}} \tag{122}$$

Velocity Uncertainty Propagation:

The bubble's relative velocity is defined in eq. (123) and has its uncertainty propagation applied in eq. (124) with sensitivity terms defined in eq. (125)-(127).

$$\mathrm{v}_r = \left[\left(\mathrm{v}_{b,y} - \mathrm{v}_{o,y}\right)^2 + \mathrm{v}_{b,x}{}^2\right]^{0.5} \tag{123}$$

$$\sigma_{\mathrm{v}_r} = \left[\left(\frac{\partial \mathrm{v}_r}{\partial \mathrm{v}_{b,y}}\sigma_{\mathrm{v}_{b,y}}\right)^2 + \left(\frac{\partial \mathrm{v}_r}{\partial \mathrm{v}_{o,y}}\sigma_{\mathrm{v}_{o,y}}\right)^2 + \left(\frac{\partial \mathrm{v}_r}{\partial \mathrm{v}_{b,x}}\sigma_{\mathrm{v}_{b,x}}\right)^2\right]^{0.5} \tag{124}$$

$$\frac{\partial \mathrm{v}}{\partial \mathrm{v}_{b,y}} = \frac{\mathrm{v}_{b,y} - \mathrm{v}_{o,y}}{\left[\left(\mathrm{v}_{b,y} - \mathrm{v}_{o,y}\right)^2 + \mathrm{v}_{b,x}{}^2\right]^{0.5}} \tag{125}$$

$$\frac{\partial \mathrm{v}}{\partial \mathrm{v}_{o,y}} = -\frac{\mathrm{v}_{b,y} - \mathrm{v}_{o,y}}{\left[\left(\mathrm{v}_{b,y} - \mathrm{v}_{o,y}\right)^2 + \mathrm{v}_{b,x}{}^2\right]^{0.5}} \tag{126}$$

$$\frac{\partial \mathrm{v}}{\partial \mathrm{v}_{b,x}} = \frac{\mathrm{v}_{b,x}}{\left[\left(\mathrm{v}_{b,y} - \mathrm{v}_{o,y}\right)^2 + \mathrm{v}_{b,x}{}^2\right]^{0.5}} \tag{127}$$

The uncertainty sources, $\sigma_{\mathrm{v}_{b,y}}$, $\sigma_{\mathrm{v}_{o,y}}$, $\sigma_{\mathrm{v}_{b,x}}$, are calculated using eq. (128), which uses the respective velocity variable in the definition. The velocity uncertainty propagation method is described below and is adapted from Jackson [46].

$$\sigma_{\mathrm{v}} = \left[\left(\frac{\partial \mathrm{v}}{\partial l}\sigma_l\right)^2 + \left(\frac{\partial \mathrm{v}}{\partial L}\sigma_L\right)^2 + \left(\frac{\partial \mathrm{v}}{\partial \Delta t}\sigma_{\Delta t}\right)^2\right]^{0.5} \tag{128}$$

The uncertainty sources are from the length scale calibration and timing information used to capture an image pair. The velocity definition is leveraged to not rely on the pixel displacement determined by DynamicStudio's cross-correlation method which is unreported by the software. The sensitivity definitions in eq. (130)-(132) show that for the same length scale and timing uncertainties, the velocity uncertainty will increase as measured velocity increases. This trend is noticeable by the increasing velocity uncertainty seen in the bubble terminal velocity in Figure 25.

$$\mathrm{v} = \frac{l}{L}\frac{\Delta x_{\mathrm{pixel}}}{\Delta t} \tag{129}$$

$$\frac{\partial \mathrm{v}}{\partial l} = \frac{1}{L}\frac{\Delta x_{\mathrm{pixel}}}{\Delta t} = \frac{\mathrm{v}}{l} \tag{130}$$

$$\frac{\partial \mathrm{v}}{\partial L} = \frac{-l}{L^2}\frac{\Delta x_{\mathrm{pixel}}}{\Delta t} = -\frac{\mathrm{v}}{L} \tag{131}$$

$$\frac{\partial \mathrm{v}}{\partial \Delta t} = -\frac{l}{L}\frac{\Delta x_{\mathrm{pixel}}}{\Delta t^2} = -\frac{\mathrm{v}}{\Delta t} \tag{132}$$

Pressure Uncertainty Propagation:

The pressure uncertainty contribution to the form drag force was not considered in the uncertainty analysis as discussed in Section 4.4. A conservative application of the Kline McClintock method is performed on a general form of the queen2 algorithm described in Dabiri [41]. Pressure at a coordinate position is determined by integrating the pressure gradient from a boundary location to the coordinate position of interest as shown in eq. (133). The pressure at the boundary condition is assumed to be zero in the queen2 algorithm. An assumed pressure boundary condition does not affect the form drag force calculation which depends only relative pressure differences.

$$P = P_o + \int_{x_1}^{x_2} \nabla P \, dx \tag{133}$$

$$\sigma_P = \frac{\partial P}{\partial \nabla P}\sigma_{\nabla P} \tag{134}$$

$$\nabla P = -\rho\left(\frac{D\vec{\mathrm{v}}}{Dt} - \nu\nabla^2\vec{\mathrm{v}}\right) \tag{135}$$

$$\nabla P = -\rho\left(\frac{\partial\vec{\mathrm{v}}}{\partial t} + \mathrm{v}_x\frac{\partial\vec{\mathrm{v}}}{\partial x} + \mathrm{v}_y\frac{\partial\vec{\mathrm{v}}}{\partial y}\right) + \nu\left(\frac{\partial^2\vec{\mathrm{v}}}{\partial x^2} + \frac{\partial^2\vec{\mathrm{v}}}{\partial y^2}\right) \tag{136}$$

$$\frac{\partial P}{\partial x} \approx -\rho\left(\frac{\Delta\mathrm{v}_x}{\Delta t} + \mathrm{v}_x\frac{\Delta\mathrm{v}_x}{\Delta x} + \mathrm{v}_y\frac{\Delta\mathrm{v}_x}{\Delta y}\right) + \nu\left(\frac{\Delta{\mathrm{v}_x}^2}{\Delta x^2} + \frac{\Delta{\mathrm{v}_x}^2}{\Delta y^2}\right) \tag{137}$$

$$\frac{\partial P}{\partial y} \approx -\rho\left(\frac{\Delta \mathrm{v}_y}{\Delta t} + \mathrm{v}_x \frac{\Delta \mathrm{v}_y}{\Delta x} + \mathrm{v}_y \frac{\Delta \mathrm{v}_y}{\Delta y}\right) + \nu\left(\frac{\Delta \mathrm{v}_y{}^2}{\Delta x^2} + \frac{\Delta \mathrm{v}_y{}^2}{\Delta y^2}\right) \tag{138}$$

The pressure gradient expressions in eq. (137)-(138) are numerically approximated as shown in eq. (139). The remaining derivation is performed on the horizontal pressure gradient but is analogous for the vertical pressure gradient with the velocity variable replaced by its respective vertical velocity component.

$$\frac{\partial P}{\partial x} \approx -\rho\left(\frac{u_{x_{i,j,k+1}} - u_{x_{i,j,k}}}{\Delta t}\right) + \mu\left[\frac{u_{x_{i+1,j,k}} + u_{x_{i-1,j,k}} + u_{x_{i,j+1,k}} + u_{x_{i,j-1,k}}}{4} - u_{x_{i,j,k}}\right] \tag{139}$$

The terms in eq. (139), are substituted using definitions in eq. (140) which resulted in eq. (141). This maintained readability and assisted with keeping track of variables. The Kline-McClintock is applied resulting in eq. (142).

$$\frac{\partial P}{\partial x} = \alpha;\, u_{x_{i,j,k+1}} = \beta;\, u_{x_{i,j,k}} = \chi;\, u_{x_{i+1,j,k}} = \delta;\, u_{x_{i-1,j,k}} = \varepsilon;\, u_{x_{i,j+1,k}} = \gamma;\, u_{x_{i,j-1,k}} = \eta \tag{140}$$

$$\alpha \approx -\rho\left(\frac{\beta - \chi}{\Delta t}\right) + \mu\left[\frac{\delta + \varepsilon + \gamma + \eta}{4} - \chi\right] \tag{141}$$

$$\sigma_\alpha = \left[\left(\frac{\partial \alpha}{\partial \Delta t}\sigma_{\Delta t}\right)^2 + \left(\frac{\partial \alpha}{\partial \beta}\sigma_\beta\right)^2 + \left(\frac{\partial \alpha}{\partial \chi}\sigma_\chi\right)^2 + \left(\frac{\partial \alpha}{\partial \delta}\sigma_\delta\right)^2 + \left(\frac{\partial \alpha}{\partial \varepsilon}\sigma_\varepsilon\right)^2 + \left(\frac{\partial \alpha}{\partial \gamma}\sigma_\gamma\right)^2 + \left(\frac{\partial \alpha}{\partial \eta}\sigma_\eta\right)^2\right]^{0.5} \tag{142}$$

The sensitivity terms are expressed below in eq, (143)-(149):

$$\frac{\partial \alpha}{\partial \Delta t} = \rho\frac{(\beta - \chi)}{\Delta t^2} \tag{143}$$

$$\frac{\partial \alpha}{\partial \beta} = -\frac{\rho}{\Delta t} \tag{144}$$

$$\frac{\partial \alpha}{\partial \chi} = \frac{\rho}{\Delta t} - \mu \tag{145}$$

$$\frac{\partial \alpha}{\partial \delta} = \frac{\mu}{4} \tag{146}$$

$$\frac{\partial \alpha}{\partial \varepsilon} = \frac{\mu}{4} \tag{147}$$

$$\frac{\partial \alpha}{\partial \gamma} = \frac{\mu}{4} \tag{148}$$

$$\frac{\partial \alpha}{\partial \eta} = \frac{\mu}{4} \tag{149}$$

An order of magnitude analysis can be used to determine the most influential contributions to the uncertainty. Because queen2 performs eight distinct path integrations and averages the top two median numbers, it would require the source code to be modified to output the specific integration paths selected for every velocity vector location that is having the pressure computed. It is known that the largest velocity components are on the order of [cm/s] and uncertainties in velocity are on the order of [mm/s]:

$$\sigma_\beta = \sigma_\chi = \sigma_\delta = \sigma_\varepsilon = \sigma_\gamma = \sigma_\eta = \sigma_{\mathrm{v}} \approx 10^{-3}\left[\frac{\mathrm{m}}{\mathrm{s}}\right] \tag{150}$$

$$\beta \approx 10^{-2}\left[\frac{\mathrm{cm}}{\mathrm{s}}\right]; \chi \approx 10^{-2}\left[\frac{\mathrm{cm}}{\mathrm{s}}\right]; \Delta t \approx 10^{-3}[\mathrm{s}]; \sigma_{\Delta t} \approx 10^{-9}[\mathrm{s}] \tag{151}$$

The order of magnitude for uncertainty and variable values in eq. (150)-(151) are substituted into the sensitivity terms to determine the approximate order of magnitude of the total uncertainty for a pressure gradient.

$$\left(\frac{\partial \alpha}{\partial \Delta t}\sigma_{\Delta t}\right)^2 \approx \left(10^3\frac{\left(10^{-2}\right)}{\left(10^{-3}\right)^2}10^{-9}\right)^2 = 10^{-4} \tag{152}$$

$$\left(\frac{\partial \alpha}{\partial \beta}\sigma_\beta\right)^2 \approx \left(-\frac{10^3}{10^{-3}}10^{-3}\right)^2 = 10^6 \tag{153}$$

$$\left(\frac{\partial \alpha}{\partial \chi}\sigma_\chi\right)^2 \approx \left(\left(\frac{10^3}{10^{-3}} - 10^{-3}\right)10^{-3}\right)^2 = 10^6 \tag{154}$$

$$\left(\frac{\partial \alpha}{\partial \delta}\sigma_{\mathrm{v}}\right)^2 \approx \left(10^{-3}10^{-3}\right)^2 = 10^{-12} \tag{155}$$

$$\left(\frac{\partial \alpha}{\partial \varepsilon}\sigma_{\mathrm{v}}\right)^2 \approx \left(10^{-3}10^{-3}\right)^2 = 10^{-12} \tag{156}$$

$$\left(\frac{\partial \alpha}{\partial \gamma}\sigma_{\mathrm{v}}\right)^2 \approx \left(10^{-3}10^{-3}\right)^2 = 10^{-12} \tag{157}$$

$$\left(\frac{\partial \alpha}{\partial \eta}\sigma_{\mathrm{v}}\right)^2 \approx \left(10^{-3}10^{-3}\right)^2 = 10^{-12} \tag{158}$$

Looking at the order of magnitude analysis, the viscous, eq. (155)-(158), and the temporal, eq. (152), sensitivity terms do not contribute to the pressure gradient's uncertainty and can be neglected. This reduces the pressure gradient uncertainty equation to:

$$\sigma_{\alpha} = \left[\left(-\frac{\rho}{\Delta t}\sigma_{\mathrm{v}}\right)^2 + \left(\frac{\rho}{\Delta t}\sigma_{\mathrm{v}}\right)^2\right]^{0.5} \tag{159}$$

Substituting order of magnitudes above into the above equation results in a pressure gradient having roughly and uncertainty of:

$$\sigma_{\alpha} = \left[\left(-\frac{10^3}{10^{-3}}10^3\right)^2 + \left(\frac{10^3}{10^{-3}}10^3\right)^2\right]^{0.5} = 10^3 \tag{160}$$

$$\sigma_{\frac{\partial P}{\partial x}} \approx 10^3\left[\frac{\mathrm{Pa}}{\mathrm{m}}\right] \tag{161}$$

The numerical integration of the pressure gradient can be represented as:

$$\Delta P \approx \sum_{i=1}^{N} \nabla P_i \Delta x_i \tag{162}$$

The queen2 algorithm performs this line integral from eight different locations along the physical boundary of the spatial data. To remain conservative the largest uncertainty would come from integrating diagonally across the data to provide the longest track length. If the uncertainty of the pressure gradient in the x and y directions are assumed to be equal and the same in each cell, the uncertainty for the relative pressure is:

$$N \approx 10^2 \text{ cells}; \Delta \mathrm{x} \approx 10^{-3}[\mathrm{m}]; \nabla P \approx 10^4\left[\frac{\mathrm{Pa}}{\mathrm{m}}\right]; \sigma_{\nabla P} \approx 10^3\left[\frac{\mathrm{Pa}}{\mathrm{m}}\right]; \sigma_{\Delta x} \approx 10^{-5}[\mathrm{m}] \tag{163}$$

$$\sigma_P \approx \left[N\left(\left(\Delta x \sigma_{\nabla P}\right)^2 + \left(\nabla P \sigma_{\Delta x}\right)^2\right)\right]^{0.5} \tag{164}$$

$$\sigma_P \approx \left[10^2\left(\left(10^{-3}10^3\right)^2 + \left(10^4 10^{-5}\right)^2\right)\right]^{0.5} \tag{165}$$

$$\sigma_P \approx 10^1[\mathrm{Pa}] \tag{166}$$

The conservative approximation of the relative pressure uncertainty is on the same order of magnitude as the calculated pressure differences and shows that the numerical integration compounds uncertainty results in a unreasonably large uncertainty contribution from the pressure algorithm. Because the accuracy of the algorithm has already been demonstrated in other studies [41], [42], the pressure uncertainty was neglected from the analysis. This reduces the pressure force uncertainty to eq. (167) which has no uncertainty dependence on the pressure.

$$\sigma_{F_{net,y,i}} = \left[\left(\frac{\partial F_{net,y,i}}{\partial \Delta x_i} \sigma_{\Delta x_i} \right)^2 + \left(\frac{\partial F_{net,y,i}}{\partial r_{cent,i}} \sigma_{r_{cent,i}} \right)^2 \right]^{0.5} \tag{167}$$

$$\frac{\partial F_{net,y,i}}{\partial r_{cent,i}} = -P \Delta x_i \pi \tag{168}$$

$$\frac{\partial F_{net,y,i}}{\partial \Delta x_i} = -P_i \pi r_{cent,i} \tag{169}$$

Virtual Mass Coefficient Uncertainty Propagation:

The virtual mass coefficient is defined by eq. (170) with uncertainty dependent on the added mass, eq. (171), and displaced mass, eq. (173). The added mass is the summation of each differential added mass cell in the flow domain defined by eq. (172).

$$C_{VM,2D} = \frac{m_{a,2D}}{m_{disp}} \tag{170}$$

$$m_{a,2D} = \sum_{i=1}^{\#\text{of cells}} m_{a,2D,i} \tag{171}$$

$$m_{a,2D,i} = \rho_f \Delta x_i \Delta y_i \frac{{u_{r,i}}^2}{{U_o}^2} \tag{172}$$

$$m_{disp} = \rho_f \frac{\pi}{4} {D_{eq}}^2 \tag{173}$$

Virtual mass coefficient uncertainty is defined by the Kline McClintock method in eq. (174), with uncertainty sensitivity terms defined by eq. (175)-(176).

$$\sigma_{C_{VM,2D}} = \left[\left(\frac{\partial C_{VM,2D}}{\partial m_{a,2D}} \sigma_{m_{a,2D}} \right)^2 + \left(\frac{\partial C_{VM,2D}}{\partial m_{disp}} \sigma_{m_{disp}} \right)^2 \right]^{0.5} \tag{174}$$

$$\frac{\partial C_{VM,2D}}{\partial m_a} = \frac{1}{m_{disp}} \tag{175}$$

$$\frac{\partial C_{VM,2D}}{\partial m_{disp}} = -\frac{m_{a,2D}}{m_{disp}^{2}} \tag{176}$$

The added mass uncertainty is propagated from the summation of differential added mass cells, eq. (177), which has uncertainty in each cell calculated with eq. (178).

$$\sigma_{m_{a,2D}} = \left[\left(\frac{\partial m_{a,2D}}{\partial m_{a,2D,1}}\sigma_{m_{a,1}}\right)^2 + \ldots + \left(\frac{\partial m_{a,2D}}{\partial m_{a,2D,N}}\sigma_{m_{a,N}}\right)^2\right]^{0.5} \tag{177}$$

$$\sigma_{m_{a,2D,i}} = \left[\left(\frac{\partial m_{a,2D,i}}{\partial \Delta x,i}\sigma_{\Delta x}\right)^2 + \left(\frac{\partial m_{a,2D,i}}{\partial \Delta y,i}\sigma_{\Delta y}\right)^2 + \left(\frac{\partial m_{a,2D,i}}{\partial u_{r,i}}\sigma_{u_{r,i}}\right)^2 + \left(\frac{\partial m_{a,2D,i}}{\partial U_o}\sigma_{U_o}\right)^2\right]^{0.5} \tag{178}$$

The sensitivity terms defined in eq. (179)–(182) use a relative velocity measured in each cell in a reference frame with the flow field stationary and the cylinder moving.

$$\frac{\partial m_{a,2D,i}}{\partial \Delta x_i} = \rho \Delta y_i \frac{u_{r,i}^{2}}{U_o^{2}} \tag{179}$$

$$\frac{\partial m_{a,2D,i}}{\partial \Delta y_i} = \rho \Delta x_i \frac{u_{r,i}^{2}}{U_o^{2}} \tag{180}$$

$$\frac{\partial m_{a,2D,i}}{\partial u_{r,i}} = 2\rho \Delta x_i \Delta y_i \frac{u_{r,i}}{U_o^{2}} \tag{181}$$

$$\frac{\partial m_{a,2D,i}}{\partial U_o} = -2\rho \Delta x_i \Delta y_i \frac{u_{r,i}^{2}}{U_o^{3}} \tag{182}$$

The values $\Delta x_i, \Delta y_i$ are the cell widths in the horizontal and vertical directions, respectively. The definition of the cell width is shown in eq. (183), and is analogous for the vertical cell width.

$$\Delta x_i = \frac{l}{L}\Delta x_{i,pix} \tag{183}$$

$$\sigma_{\Delta x_i} = \left[\left(\frac{\partial \Delta x_i}{\partial l}\sigma_l\right)^2 + \left(\frac{\partial \Delta x_i}{\partial L}\sigma_L\right)^2\right]^{0.5} \tag{184}$$

$$\frac{\partial \Delta x_i}{\partial l} = \frac{1}{L}\Delta x_{i,pix} = \frac{\Delta x_i}{l} \tag{185}$$

$$\frac{\partial \Delta x_i}{\partial L} = -\frac{l}{L^2}\Delta x_{i,pix} = \frac{\Delta x_i}{L} \tag{186}$$

The displaced two-dimensional mass uncertainty and sensitivity is shown in eq. (187)-, and is only a function of the cylinder rod diameter.

$$\sigma_{m_{disp}} = \frac{\partial m_{disp}}{\partial D_{eq}} \sigma_{D_{eq}} \tag{187}$$

$$\sigma_{m_{disp}} = \left(\frac{\pi}{2} \rho_f D_{eq} \right) \sigma_{D_{eq}} \tag{188}$$

The uncertainty for each cell's added mass per unit length is performed across the flow field and the maximum value is chosen to apply for every cell's uncertainty to add conservatism. This reduces eq. (177) to eq. (190).

$$\sigma_{m_{a,2D}} = \left[N \left(\sigma_{m_{a,2D,\max}} \right)^2 \right]^{0.5} \tag{189}$$

$$\sigma_{m_{a,2D}} = \left(N \right)^{0.5} \sigma_{m_{a,2D,\max}} \tag{190}$$

Reynolds Number Uncertainty Propagation:

The Reynolds number is defined by eq. (191), and has uncertainty dependency on the relative velocity and diameter for either the bubbles or cylinder. The thermo-physical properties for density and dynamic viscosity were not considered because values were obtained from the National Institute of Standards and Technology (NIST) Chemistry WebBook.

$$\mathrm{Re} = \frac{\rho \mathrm{v}_r D_{eq}}{\mu} \tag{191}$$

$$\sigma_{\mathrm{Re}} = \left[\left(\frac{\partial \mathrm{Re}}{\partial \mathrm{v}_r} \sigma_{\mathrm{v}_r} \right)^2 + \left(\frac{\partial \mathrm{Re}}{\partial D_{eq}} \sigma_{D_{eq}} \right)^2 \right]^{0.5} \tag{192}$$

$$\frac{\partial \mathrm{Re}}{\partial \mathrm{v}_r} = \frac{\rho D_{eq}}{\mu} \tag{193}$$

$$\frac{\partial \mathrm{Re}}{\partial D_{eq}} = \frac{\rho \mathrm{v}_r}{\mu} \tag{194}$$

APPENDIX B: POTENTIAL FLOW KINETIC ENERGY PROOF

The reference frame used to evaluate the kinetic energy in the flow domain does not impact the virtual mass calculated. The PIV data recorded was for a stationary cylinder with downward fluid flow, while virtual mass is typically determined for moving objects in a stationary fluid. To provide this direct comparison there are two methods to change the moving fluid reference frame to the stationary fluid. One method is to calculate the kinetic energy of the moving fluid and subtract the uniform kinetic energy field as if the object was not in the flow. The second method is calculating the relative velocity from the measured velocity field for a reference frame with a moving object in a stationary fluid.

Relative Kinetic Energy

The virtual mass coefficient is defined, eq. (195), by the ratio of the integrated kinetic energy field, eq. (196), over a reference kinetic energy, eq. (197), such as the cylinder moving at the inlet velocity.

$$C_{VM} = \frac{KE_{field}}{KE_{ref}} \tag{195}$$

$$KE_{field} = \int_{o}^{2\pi}\int_{R}^{\infty} \frac{1}{2}\rho\left(V^2 - U^2\right) r dr d\theta \tag{196}$$

$$KE_{ref} = \frac{1}{2}\rho\pi R^2 U^2 \tag{197}$$

The moving fluid velocity, V, and reference uniform velocity, U, are defined in polar coordinates in eq. (198), with subsequent component definitions by eq. (199)-(200)

$$V = \sqrt{v_r^2 + v_\theta^2}\ ; U = \sqrt{U_r^2 + U_\theta^2} \tag{198}$$

$$v_r = U\cos\left(\theta\right)\left(1 - \frac{R^2}{r^2}\right); v_\theta = -U\sin\left(\theta\right)\left(1 + \frac{R^2}{r^2}\right) \tag{199}$$

$$U_r = Ucos\left(\theta\right); U_\theta = -Usin\left(\theta\right) \tag{200}$$

The preceding definitions are substituted into eq. (201), and expanded in eq. (202)-(205).

$$V^2 - U^2 = v_r^2 + v_\theta^2 - U_r^2 - U_\theta^2 \tag{201}$$

$$v_r^2 = \left[U\cos(\theta)\left(1-\frac{R^2}{r^2}\right)\right]^2 = U^2\cos^2(\theta)\left(1-\frac{2R^2}{r^2}+\frac{R^4}{r^4}\right) \tag{202}$$

$$v_\theta^2 = \left[-U\sin(\theta)\left(1+\frac{R^2}{r^2}\right)\right]^2 = U^2\sin^2(\theta)\left(1+\frac{2R^2}{r^2}+\frac{R^4}{r^4}\right) \tag{203}$$

$$U_r^2 = \left[Ucos(\theta)\right]^2 \tag{204}$$

$$U_\theta^2 = \left[Usin(\theta)\right]^2 \tag{205}$$

The expanded velocity components are combined to form a single expression in eq. (206), which is substituted into eq. (207) resulting in eq. (208).

$$V^2 - U^2 = U^2\cos^2(\theta)\left(1-\frac{2R^2}{r^2}+\frac{R^4}{r^4}\right)$$
$$+U^2\sin^2(\theta)\left(1+\frac{2R^2}{r^2}+\frac{R^4}{r^4}\right) - U^2\cos^2(\theta) - U^2\sin^2(\theta) \tag{206}$$

$$V^2 - U^2 = U^2\cos^2(\theta)\left(-\frac{2R^2}{r^2}+\frac{R^4}{r^4}\right) + U^2\sin^2(\theta)\left(\frac{2R^2}{r^2}+\frac{R^4}{r^4}\right) \tag{207}$$

$$KE_{field} = \int_o^{2\pi}\int_R^{\infty}\frac{1}{2}\rho\left[U^2\cos^2(\theta)\left(-\frac{2R^2}{r}+\frac{R^4}{r^3}\right)\right.$$
$$\left. +U^2\sin^2(\theta)\left(\frac{2R^2}{r}+\frac{R^4}{r^3}\right)\right] dr d\theta \tag{208}$$

The integration with respect to r, is performed resulting in eq. (209) and evaluated across its limits to obtain eq. (211).

$$KE_{field} = \int_o^{2\pi}\frac{1}{2}\rho\left[U^2\cos^2(\theta)\left(-2R^2\ln(r)-\frac{R^4}{2r^2}\right)\right.$$
$$\left. +U^2\sin^2(\theta)\left(2R^2\ln(r)-\frac{R^4}{2r^2}\right)\right]_R^{\infty} d\theta \tag{209}$$

$$\left[U^2\cos^2(\theta)\left(-2R^2\ln(r)-\frac{R^4}{2r^2}\right)+U^2\sin^2(\theta)\left(2R^2\ln(r)-\frac{R^4}{2r^2}\right)\right]_R^\infty$$

$$=U^2\cos^2(\theta)\left(2R^2\ln\left(\frac{R}{\infty}\right)+\frac{R^2}{2}\right)+U^2\sin^2(\theta)\left(2R^2\ln\left(\frac{\infty}{R}\right)+\frac{R^2}{2}\right) \tag{210}$$

$$KE_{field}=\int_o^{2\pi}\frac{1}{2}\rho\left[U^2\cos^2(\theta)\left(2R^2\ln\left(\frac{R}{\infty}\right)+\frac{R^2}{2}\right)\right.$$

$$\left.+U^2\sin^2(\theta)\left(2R^2\ln\left(\frac{\infty}{R}\right)+\frac{R^2}{2}\right)\right]d\theta \tag{211}$$

The integration across θ, is next performed and evaluated across its limits in eq. (212). The definition of logarithms addition division results in the two natural logarithm terms in eq. (213) to be equal to natural log of one which is zero. This simplifies to eq. (214) and subsequently eq. (215)

$$KE_{field}=\frac{1}{2}\rho\left[U^2\pi\left(2R^2\ln\left(\frac{R}{\infty}\right)+\frac{R^2}{2}\right)+U^2\pi\left(2R^2\ln\left(\frac{\infty}{R}\right)+\frac{R^2}{2}\right)\right] \tag{212}$$

$$KE_{field}=\frac{1}{2}\rho\left[U^2\pi\left(2R^2\ln\left(\frac{R}{\infty}\right)+2R^2\ln\left(\frac{\infty}{R}\right)+\frac{R^2}{2}+\frac{R^2}{2}\right)\right] \tag{213}$$

$$KE_{field}=\frac{1}{2}\rho\left[U^2\pi\left(\frac{R^2}{2}+\frac{R^2}{2}\right)\right] \tag{214}$$

$$\boldsymbol{KE_{field}=\frac{1}{2}\rho\pi R^2U^2} \tag{215}$$

Equations (197) and (215) are substituted into eq. (195) and results in a virtual mass coefficient for on a cylinder in potential flow to be:

$$C_{VM}=\frac{\frac{1}{2}\rho_f\pi R^2U^2}{\frac{1}{2}\rho_f\pi R^2U^2} \tag{216}$$

$$C_{VM}=1 \tag{217}$$

Relative Velocity

The second method for evaluating the virtual mass coefficient is shown here. The virtual mass coefficient definition is shown in eq. (218) and is equivalent to eq. (195). The integrated kinetic energy field is defined by eq. (219) and the reference kinetic energy is defined by eq. (220).

$$C_{VM} = \frac{KE_{field}}{KE_{ref}} \tag{218}$$

$$KE_{field} = \int_{o}^{2\pi}\int_{R}^{\infty}\left(\frac{1}{2}\rho V_{rel}^2\right) r dr d\theta \tag{219}$$

$$KE_{ref} = \frac{1}{2}\rho\pi R^2 U^2 \tag{220}$$

The relative velocity is defined by the uniform inlet velocity components subtracted from the moving fluid velocity and is shown in eq.(221)-(228).

$$V = \sqrt{v_r^2 + v_\theta^2}\ ; U = \sqrt{U_r^2 + U_\theta^2} \tag{221}$$

$$V_{rel} = \sqrt{\left(v_r - U_r\right)^2 + \left(v_\theta - U_\theta\right)^2} \tag{222}$$

$$V_{rel}^2 = \left(v_r - U_r\right)^2 + \left(v_\theta - U_\theta\right)^2 \tag{223}$$

$$v_r = U\cos\left(\theta\right)\left(1 - \frac{R^2}{r^2}\right); v_\theta = -U\sin\left(\theta\right)\left(1 + \frac{R^2}{r^2}\right) \tag{224}$$

$$U_r = Ucos\left(\theta\right); U_\theta = -Usin\left(\theta\right) \tag{225}$$

$$V_{rel}^2 = \left(U\cos\left(\theta\right)\left(1 - \frac{R^2}{r^2}\right) - Ucos\left(\theta\right)\right)^2 + \left(-U\sin\left(\theta\right)\left(1 + \frac{R^2}{r^2}\right) - -Usin\left(\theta\right)\right)^2 \tag{226}$$

$$V_{rel}^2 = \left(U\cos\left(\theta\right)\left(\frac{R^2}{r^2}\right)\right)^2 + \left(-U\sin\left(\theta\right)\left(\frac{R^2}{r^2}\right)\right)^2 \tag{227}$$

$$V_{rel}^2 = U^2\cos^2\left(\theta\right)\left(\frac{R^4}{r^4}\right) + U^2\sin^2\left(\theta\right)\left(\frac{R^4}{r^4}\right) \tag{228}$$

The relative velocity definition from eq. (228) is substituted into the kinetic energy equation which results in eq. (229).

$$KE_{field} = \int_{o}^{2\pi}\int_{R}^{\infty} \frac{1}{2}\rho\left[U^2\cos^2(\theta)\left(\frac{R^4}{r^3}\right)+U^2\sin^2(\theta)\left(\frac{R^4}{r^3}\right)\right]drd\theta \tag{229}$$

The radiation integration is performed in eq. (230) and evaluated across its limits resulting in eq. (232).

$$KE_{field} = \int_{o}^{2\pi} \frac{1}{2}\rho\left[U^2\cos^2(\theta)\left(-\frac{R^4}{2r^2}\right)+U^2\sin^2(\theta)\left(-\frac{R^4}{2r^2}\right)\right]_R^\infty d\theta \tag{230}$$

$$U^2\left[\cos^2(\theta)\left(-\frac{R^4}{2r^2}\right)+\sin^2(\theta)\left(-\frac{R^4}{2r^2}\right)\right]_R^\infty = U^2\left[\cos^2(\theta)\frac{R^2}{2}+\sin^2(\theta)\frac{R^2}{2}\right] \tag{231}$$

$$KE_{field} = \int_0^{2\pi}\frac{1}{2}\rho U^2\left[\cos^2(\theta)\frac{R^2}{2}+\sin^2(\theta)\frac{R^2}{2}\right]d\theta \tag{232}$$

Common constant values from in eq. (232) are factored from the sine and cosine terms to implement the trigonometric definition for $\left[\cos^2(\theta)+\sin^2(\theta)\right]=1$. This simplifies the expression to eq. (233) and subsequently eq. (236).

$$KE_{field} = \frac{1}{2}\rho\int_0^{2\pi}\frac{R^2}{2}U^2\left[\cos^2(\theta)+\sin^2(\theta)\right]d\theta \tag{233}$$

$$KE_{field} = \frac{1}{2}\rho\int_0^{2\pi}\frac{R^2}{2}U^2\, d\theta \tag{234}$$

$$KE_{field} = \frac{1}{2}\rho\left[\frac{R^2}{2}U^2\right]_0^{2\pi} \tag{235}$$

$$\boldsymbol{KE_{field} = \frac{1}{2}\rho\pi R^2U^2} \tag{236}$$

Substituting eq. (220)and eq. (236) into eq. (218) results in eq. (237). This simplifies to a virtual mass coefficient value of one which is equivalent to the result obtained from the relative kinetic energy method.

$$C_{VM} = \frac{\frac{1}{2}\rho_f \pi R^2 U^2}{\frac{1}{2}\rho_f \pi R^2 U^2} \tag{237}$$

$$C_{VM} = 1 \tag{238}$$